Politecnico di Milano
School of Industrial and Information Engineering
Master of Science in Mechanical Engineering

Application of detailed chemistry approaches with a semi-global mechanism for soot emissions in non-premixed flames

Supervisor: Prof. Gianluca D'ERRICO

Authors:
Damiano NARDI Matr. 836525
Aldo SESTITO Matr. 836488

Academic Year 2015–2016

Work it may, but SHINE it must.

Acknowledgments

Al termine di questo lavoro durato nove mesi, vogliamo prima di tutto ringraziarci l'un l'altro per il reciproco supporto e la pazienza dimostrata quando lo sconforto prendeva il sopravvento.

Grazie Aldo (scritto da Damiano).

Grazie Damiano (scritto da Aldo).

Doverosi e sentiti ringraziamenti vanno fatti al nostro relatore, il professore Gianluca D'Errico, perchè è stato una presenza costante ogni qual volta ne abbiamo avuto bisogno. La sua calma e la sua conoscenza sono state un'ancora di salvezza preziosa.

Ci teniamo anche a ringraziare il professore Tommaso Lucchini per la disponibilità e per il continuo e preciso supporto fornitoci.

Non vogliamo omettere nessuno dei nostri colleghi e amici che abbiamo avuto il piacere di conoscere al Poli, ma siamo sicuri che di qualcuno ci dimenticheremo. Quindi se vi sentite parte di questo gruppo di persone, questi ringraziamenti sono anche per voi. Dei ringraziamenti speciali però vanno fatti al Mitico (lui sa chi è), Filippo, Andre, Manuel, Giada, Ale, Robu: siete stati con noi dal primo all'ultimo giorno e vi siete rivelati colleghi e amici straordinari.

Ora è Damiano che parla.

Mi rendo conto che le persone che devo ringraziare di più sono i membri della mia famiglia (nonne, cugini, etc..) ed in particolare mamma, papà e Gp: dal giorno in cui ho per la prima volta messo piede nelle fredde e sterili aule della Bovisa non mi avete mai fatto mancare alcun tipo di supporto, materiale e affettivo. Siete stati il principale motore (scusate la deformazione professionale) della mia ambizione, e ve ne sarò riconoscente per sempre.

Una volta una persona saggia mi ha detto che non conosci davvero qualcuno finchè non ci vivi assieme: sarebbe quindi un crimine non ringraziare i miei stupendi coinquilini passati e presenti (Nico, Bonda, Zio, Cascò e Stiveeeen) e i compagni di pianerottolo (Cat e Pulkas) che sono stati per 5 anni la mia seconda famiglia. Le partite a PES, il risotto con le bistecche, le serie TV, la palestra fai-da-te e tante altre cose sono ricordi che conserverò con gioia per sempre nel mio cuore.

Impossibile poi non ringraziare i miei conterranei (nonchè soci) Marco, Filippo, Andrea, Gloria, Ele, Erica e Monica: crescere al vostro fianco è stato stupendo e non esagero se dico che non sarei la persona di oggi senza di voi.

Infine (ma non ultimi per importanza) ringrazio Nico, Ciano, Uggio, Dema, Edo, Emi, Bonda, Lutto e Gigio (altresì detti «i Best»): sono davvero grato al Belfiore per averci fatti incontrare e per avermi donato amicizie così preziose.

Ora parla Aldo.

Al contrario di Dante io il mio viaggio, nella mia personalissima selva oscura che è stato questo lungo periodo universitario, non l'ho iniziato con la guida preziosa e saggia di Virgilio, ma con quella fuorviante di Matteo e Vittorio. Tuttavia, come diceva Mark Twain, "l'Inferno lo preferisco per la compagnia". Grazie amici, siete stati compagni, avversari, confidenti, cuochi, pessimi giocatori di FIFA paragonati a me e moltissime altre cose. Voglio ringraziare anche amici che, presto o tardi, ho considerato coinquilini di case diverse, l'адвокатом Carlo, la puntuale Chiara, la fashion blogger Sabrina e la M&Ms di via San Rocco (Mario e Mastro). Un grazie speciale va alla mia coinquilina Lucrezia, senza la quale avrei patito la fame spesse volte. Tutte le persone conosciute, viste o frequentate in questi anni a Milano, soprattutto tutti i catanzaresi trapiantati qui che non mi hanno mai fatto sentire troppo lontano da casa, meritano anche loro un ringraziamento particolare.

Poi ci sono le persone lontane, quelle che non senti e quelle più assillanti (scusate la rima). Questa dualità è rappresentata perfettamente da Enrico ed Antonio, amici da sempre e per sempre.

Grazie al profugo Andrea. Testimonio che la tua integrazione nel nostro paese è stata perfetta in questi 20 anni che ci conosciamo, non mi dilungo perchè altrimenti si entra nel politico e non è la sede adatta.

Grazie a tutti i miei colleghi universitari dei primi due anni, abbiamo intrapreso strade diverse col tempo, ma siete stati importanti, avete reso quasi soft l'impatto con l'università.

Grazie a tutti i miei amici di Catanzaro, Soverato, Tropea, un elenco infinito di persone a cui voglio bene.

Grazie a tutti gli amici del liceo ancora non citati, in particolare, Giuseppe, Marco, Alessandro ed Alberto. Siete stati decisamente il contrario delle buone compagnie che un ragazzo dovrebbe frequentare negli anni formativi. Come in cuor mio voglio ringraziare per ciò che mi hanno lasciato tutti gli amici che ho avuto in tutta la mia vita, persone che ho perso, ma che ricordo con affetto.

Grazie a tutti i miei zii, anche per aver messo al mondo quelle innumerevoli canaglie che sono i miei adorati cugini. Siamo troppi, non posso elencarvi tutti.

Un grazie speciale alle mie nonne, che avrei voluto vivessero questo giorno speciale e a mio nonno Piero, mio fan #1.

Grazie a quello spirito libero di mia sorella Giovanna, le contraddizioni tra me e lei sono le cose che ci rendono perfettamente complementari.

Grazie a mamma e papà, che dal 18 luglio 1993 sono sempre stati e saranno per sempre fondamenta della mia crescita, spinta delle mie motivazioni e faro nelle mie incertezze. Vi voglio bene.

Se ho dimenticato qualcuno o una categoria di persone, chiedo venia, vi offrirò una cena.

Abstract

In this work, the CFD analysis of non-premixed flames is performed. In particular, the focus is to verify if the most adopted semi-empirical soot model proposed by Leung et al. is able to predict the soot formation and destruction processes if coupled with three different combustion models: Representative Interactive Flamelet (RIF) model, Tabulated Representative Interactive Flamelet (TRIF) model and Tabulated Well Mixed (TWM) model. Particular attention was given to the tabulated combustion models, since they are less time-consuming, and this feature is of particular interest for industrial practical applications. The analysis was done using the open-source CFD code OpenFOAM. All the models for combustion and soot were already implemented inside the library *Lib-ICE*, developed by the Politecnico di Milano ICEGroup.

Numerical results were compared to the experimental ones provided by Sandia Laboratories: after a brief validation of the combustion models, a trial-and-error analysis was performed changing the constants of Leung model in order to understand which is the importance of every single soot creation/destruction process and to see if it is possible to get quantitatively a good matching between numerical and experimental results despite the combustion models limits.

In the end it was shown that not only the trend but also the amount of soot can be predicted with tabulated models even if it is not clear the behaviour in some oxygen-temperature combinations. To make a more accurate analysis, more experimental data should be available in order to test the reactivity of the soot model with different oxygen-temperature conditions. Another issue is related to the choice of acetylene (C_2H_2) as unique soot precursor, while nowadays it is well accepted that a key role is played by benzene (C_6H_6) and other poly-aromatic species.

***Key-words**: CFD, soot, non-premixed, combustion, RIF, TRIF, TWM, OpenFOAM*

Sommario

In questa tesi è stata condotta l'analisi CFD riguardante fiamme non premiscelate. In particolare si è verificata la capacità del modello semi-empirico di Leung et al. di predirre la quantità di soot formato ed ossidato, accoppiandolo con diversi modelli di combustione: modello Representative Interactive Flamelet (RIF), modello Tabulated Representative Interactive Flamelet (TRIF) e modello Tabulated Well Mixed (TWM).

Si è deciso di dedicare particolare attenzione ai modelli di combustione tabulati dato che consentono una riduzione dei tempi di calcolo, molto utile in ambito industriale. L'analisi è stata realizzata usando il software CFD open-source OpenFOAM. Tutti i modelli di combustione e soot sono implementati all'interno della libreria *Lib-ICE*, interamente sviluppata dall'ICEGroup del Politecnico di Milano.

I risultati numerici ottenuti sono stati confrontati con quelli forniti dai Laboratori Sandia: dopo una breve validazione dei modelli di combustione, è stata condotta un'analisi trial-and-error modificando le costanti del modello di Leung per capire l'importanza dei singoli processi di creazione e distruzione del soot e vedere quanto è possibile avvicinare i risultati numerici e sperimentali ovviando ai limiti dei modelli di combustione.

I risultati hanno dimostrato che è possibile riprodurre in maniera piuttosto soddisfacente il comportamento del soot usando i modelli tabulati. Tuttavia in particolari condizioni di ossigeno e temperatura i modelli disponibili hanno evidenziato alcune lacune. Per fare un'analisi più dettagliata sarebbero necessari dati in altre condizioni di temperatura e ossigeno per testare la reattività dei vari modelli. Un altro possibile punto di partenza per eventuali lavori futuri può consistere nel capire se l'utilizzo di acetilene (C_2H_2) come unico precursore del soot sia corretto: recenti studi ad esempio suggeriscono che l'utilizzo del benzene (C_6H_6) potrebbe essere più appropriato.

***Key-words**: CFD, soot, non-premixed, combustion, RIF, TRIF, TWM, OpenFOAM*

Contents

List of Figures

List of Tables

Introduction

Diesel engine is one of the most efficient thermal engines currently available, largely used for energy production, automotive and naval applications and many more. However, despite its advantages, the nature of the combustion, that is a non-premixed one, leads necessarily to the production of soot, a solid pollutant species. This issue nowadays is getting always more relevant, since also modern gasoline engines adopt direct injection (GDI), therefore soot emission is becoming important also in this context. The phenomenon by itself is still not completely clear, however in the last decades many studies were carried on trying to understand the complex thermochemical processes involved. Since the legislation regarding pollutant emissions of car is getting very restrictive, in particular in EU countries, a complete comprehension of how it is formed inside the flame during combustion event is necessary. Here computational fluid-dynamic (CFD) plays a key role, since it allows to simulate all the phenomena regarding reacting flows, with a complete description of their fields and chemical species spatial distribution. This is crucial because measuring directly all of them requires expensive instrumentations and it is very difficult, if not impossible at all. However, CFD models must be validated and calibrated. In particular, combustion modeling must be carefully verified since it is one of the most complex and challenging process in fluid-dynamic.

The focus of this work is to try to understand if already existing combustion models can be coupled efficiently with the most used and accomplished semi-empirical soot prediction model, the Leung one [30]. The combustion and soot models that are used have been developed, updated and validated during the years by the Internal Combustion Engines research group (ICEGroup) of Politecnico di Milano, using the CFD open-source software OpenFOAM. It is a very powerful tool, customizable and able to simulate any kind of flow. The validation activity is performed comparing the numerical results with the ones provided by the Energy Combustion Network (ECN) of Sandia National Laboratories, which offers a huge number of detailed experimental data regarding different kinds of combustion events, with different fuels and initial oxygen-temperature conditions. Past works developed at Politecnico di Milano and other universities all over the world have clearly shown that it is possible to qualitatively catch quite well the behaviour of the soot mass in most of the experimental cases provided by Sandia. However, it is fundamental to understand how every single process that governs soot formation influences the numerical outputs. In order to obtain significant results, it is important to verify first if combustion models are able to simulate efficiently the flow fields inside the combustion chambers, since soot emissions are directly related to thermochemical spatial distribution of some specific species, position of lift-off and ignition delay. An important part of this work is related to the necessity of reducing the computational time of those combustion models that, for many different reasons that will be described inside this thesis, are practically unfeasable for industrial purpose. In particular, the focus is on the understanding if the most adopted combustion model, the Representative Interective Flamelet (RIF), that solves directly the chemistry in an accurate way but slowly, can be replaced by other models which use tabulated chemistry. Among them, Tabulated Representative Interactive Flamelet (TRIF) and Well-Mixed Model (TWM) are analyzed.

In the following chapters, strong and weak points of each of them will be emphatized and their impact on the soot calculation, which is a particular activity (it is not calculated together with other chemical species, since at each iteration it is done after the calculation of the flow fields obtained during combustion), so it heavily depends on the chosen combustion model.

The thesis is articulated in the following way:

- Chapter 1: the main features of non-premixed combustion and of soot phenomenology are described
- Chapter 2: the adopted numerical methods and models regarding combustion and soot formation are described
- Chapter 3: here it is explained how the numerical cases of interest for us are set up and launched in OpenFOAM
- Chapter 4: methods and experimental setups used in Sandia laboratories are described
- Chapter 5: combustion models are validated, paying attention to the main features and outputs that are useful for soot modeling
- Chapter 6: soot model is validated and calibrated, emphatizing the differences caused by adoption of a specific combustion model

Chapter 1

Diesel Combustion Process

In this chapter, the main features of the diesel combustion are illustrated. In particular, in the first part, the preparation of the combustible mixture is explained, focusing also on the peculiar distribution of the air fuel ratio inside the combustion chamber. In the second part, the governing processes of the soot formation and destruction are explained.

1.1 Diesel Combustion

The combustion inside a diesel engine, or in general in a non premixed combustion chamber, is a heterogenenous process. The fuel is injected in its liquid state inside the combustion chamber, containing air at high temperature and pressure. This is necessary, in a first moment, in order to allow the transition from the liquid to the gaseous phase of the fuel. Then, when the mixing process between vapour fuel and air reaches a certain condition, the mixture autoignites. In general, in an engine, the injection starts when the piston approaches the top dead center (TDC) of the chamber. If the timing is delayed or anticipated, some particular kinds of combustion processes happen, that are for instance homogeneous/partial charge combustion ignition (*HCCI*, *PCCI*), but they are out of interest for this work. The injection pressure is very high, up to 200 MPa. The mixing process inside the chamber plays a key role to obtain a high efficiency combustion. It is a very complex task, since it involves several physical and chemical processes. The fuel is injected in a chamber containing air that in general, in order to optimize the mixing, is organized according to some large scale gas motions. These are useful in order to promote fuel evaporation and mixing before the combustion, but they are also crucial during the expansion stroke of the piston, since they increase the mixing between air and burned gases allowing a better soot oxidation. For instance, swirl (Fig. 1.3) is one of the most adopted configuration. The combustion process can be divided in four phases. The first one is called *ignition delay* (AB phase of Fig. 1.1 and Fig. 1.2), it starts immedietely after the start of injection (SOI) and it ends when the combustion starts. By a practical point of view, its timing is measured up to the first point of positive heat release (see Fig. 1.1).

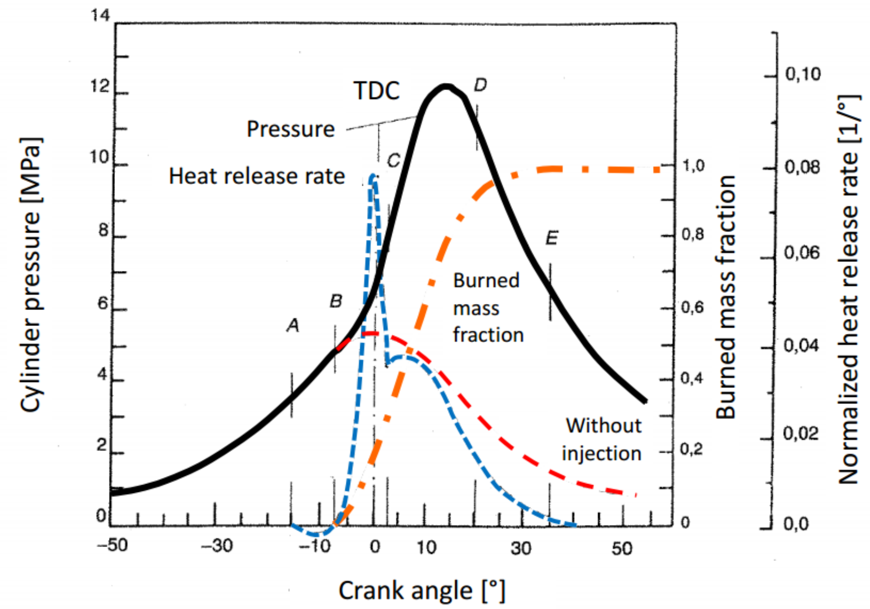

Figure 1.1: Pressure, fuel mass burned and rate of heat released (*RoHR*) versus crank angle, taken from [23]

In the first part, the curve is negative because the fuel absorbes heat and the graphs refers to the air thermodynamic conditions. This time is necessary because the mixture has to physically be generated and some preliminar cool combustion reactions (low T and p increasing) need to take place before the real combustion.

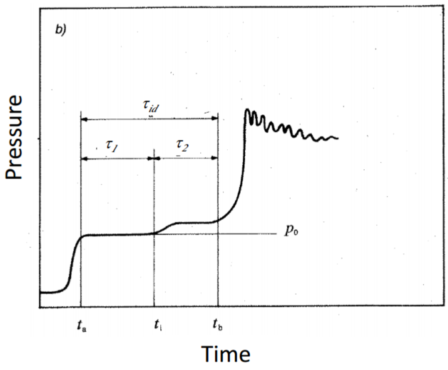

Figure 1.2: Ignition delay

The second phase of the combustion is called *rapid/premixed combustion* (*BC* phase of Fig. 1.1). During the ignition delay, the internal part of the jet has a very high momentum, so the sorrounding air is not able to carry it away. Instead the external part, which has a lower momentum, is entrained by the high momentum air and evaporates, creating a locally homogeneous mixture. Where the mixture reaches near stoichimetric condition, thanks to the high temperature and pressure, autoignition happens, producing a very steep energy release rate. The flame at this point is fully established. Then, the *RoHR* curve falls down reaching a quasi steady value. This phase is called *mixing controlled combustion* (*CD* phase of Fig. 1.1). The burning rate is mainly controlled by the efficiency of the mixing process between air and fuel. If air is capable of carry away the fuel (mainly in the external part of the jet, see Fig. 1.3), the high temperature of the chamber facilitates the evaporation and the self ignition of the parts where the mixture is stoichiometric.

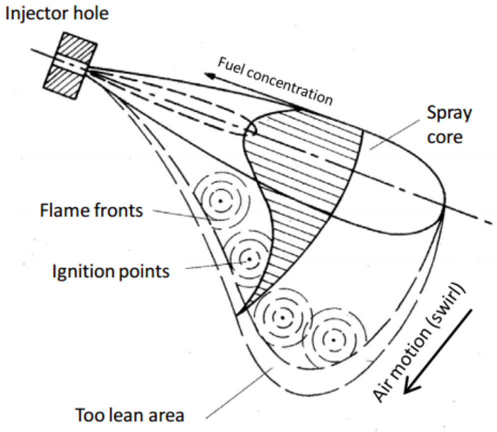

Figure 1.3: Effect of swirl on the flame [23]

The combustion rate is lower with respect to a premixed flame, because it takes time to evaporate and mix the gases. That is why the quasi steady-value of the *RoHR* is lower than the premixed peak. The last phase is called *late combustion (DE* phase of Fig. 1.1) and it corresponds to the combustion of the remaining air/fuel mixture and the partially oxidated species that are formed in the non-stoichiometric region of the flame. The large scale motions are very important in this phase because they avoid the exiting during the exhaust stroke of unburned fuel pockets or pollutants, that are mainly generated due to incomplete combustion.

1.2 Soot formation and destruction

Among the various pollutants that are generated inside a diesel engine, this thesis is focused on the analysis of soot. For this reason, other pollutant species such as NO_x and other incomplete combustion products are not treated. Soot is a solid by-product, appearing as black particles, generated mainly inside the non premixed flames, due to the heterogeneous nature of the combustion. Inside the exhaust gases, it is also called particulate matter PM. Looking at the flame structure, it is formed in the region where the air fuel ratio is lower than one, where there is lack of oxygen and abundance of carbon atoms (soot particles are characterized by a very low $^{H}/_{C}$ atoms ratio). It is clear that this critical region is the one where fuel concentration is very high, so close to the jet axis (Fig. 1.4).

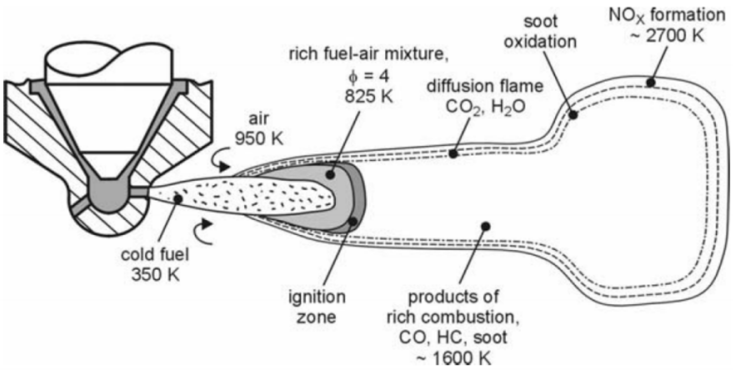

Figure 1.4: Soot and other pollutants space distribution [23]

Here the phases of its formation are fully described.

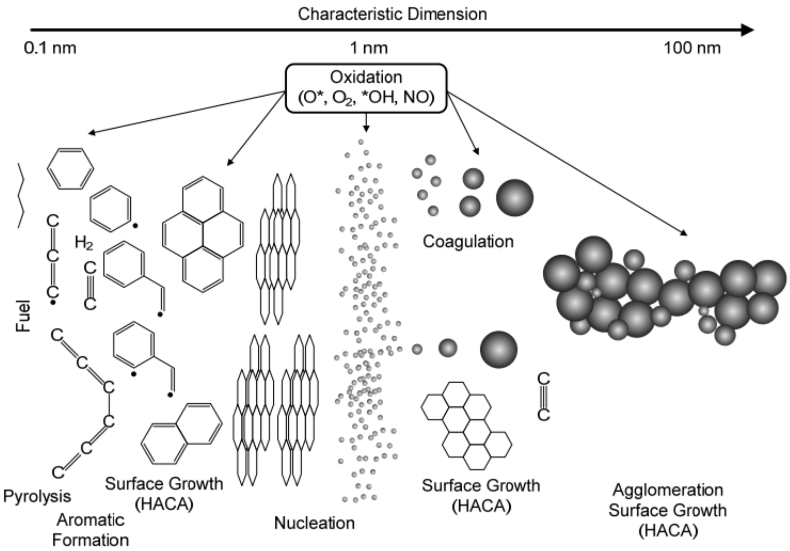

Figure 1.5: Soot formation mechanism, taken from [44]

1.2.1 Pyrolisis and formation of soot precursors

The process of pyrolysis starts when the fuel particles are heated up in an environment lean in oxygen. It consists in the chemical dissociation of some particular atoms, in this case hydrogen. So, the new hydrocarbons into which the fuel is transformed have a $^{H}/_{C}$ atoms ratio lower than 0.1, while for a common fuel it should be around 2. Some typical species that are formed are aliphatic hydrocarbons such as acetylene C_2H_2, C_2H_4, methane CH_4, C_3H_6, benzene C_6H_6 [11] and radicals. Benzene in particular, is very significant since the first process starting after the pyrolysis is the formation of the aromatic rings. This process is still not clear, but there are some theories about it according to [14], but they will not be discussed in this work. However it is rather common to consider that the main soot precursor is acetylene, mainly for its abundance, although it is well known, by experimental evidence, that fuels containing aromatic species as benzene produce more soot.

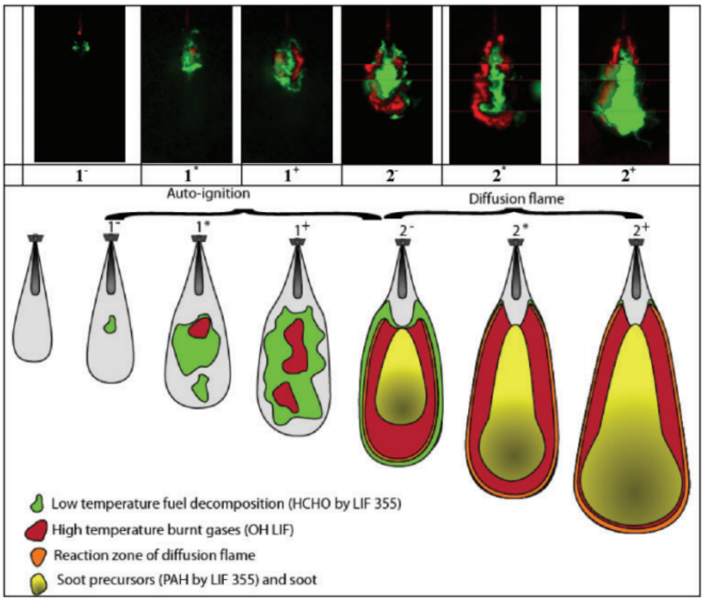

Figure 1.6: PAH distribution in a diesel flame, taken from [21]

All these species, once they are transformed into aromatic ones, start their process of evolution to poly-aromatic hydrocarbons (PAHs). This is called *H-abstraction-C2H2-addition* (*HACA* mechanism) and step by step it causes the formation of larger and larger PAHs, interacting with H radicals, dehydrogenate aromatic rings and acetylene.

1.2.2 Nucleation

This part is the least understood in soot formation [37], however it is common to consider that this growing process keeps going up to a moment in which this PAH particles reach a certain size (few nano-meters), forming the so called nuclei. This process is very fast and only few milliseconds are necessary to form large solid particles having $10^6 - 10^{12}$ carbon atoms [49]. There are two ways to see this process, as hinted by Wang [19]: the first suggests that they form starting from quasi 2D particles into curved fullerene clusters, the other says that nuclei are formed as a consequence of physical coalescence of smaller PAH, followed by a further coalescence into crosslinked 3D structures. In other words, at a certain size, some PAHs start to stick each other during collision, while others keep increasing in size. The combination of these phenomena leads to the solid particle formation [49].

1.2.3 Surface growth

This process is governed by a series of reactions happening at the interface of the nuclei with the gases. In practice, it consists in the addition of mass to already existing particles without changing their overall number. Here a key role is played by acetylene, since it contributes to the *HACA* mechanism already seen in Section 1.2.1. This was validated by Frenklach [37] with its theory of chemical similarity. It is very important to underline that soot surface growth rate is lower for larger particles, that means older ones, so the number of active sites present locally in the flame is assumed to be proportional to the square root of the total available surface area. This is called *surface agening* [30]. In Leung soot model [30], H radicals concentration, that in *HACA* theory should activate the surface of soot particles, is not accounted. Hernandez [28] suggests that in a more accurate model this should be considered.

1.2.4 Coagulation and agglomeration

Initially, particles are spherical, evolving to long chained structure by means of two following processes: coagulation and agglomeration. Notice that both of them do not change the total mass of soot, but only the number of particles. The first consists in the coalescence of small spherical particles into a bigger spherical one (diameter up to 50 nm), according to a rate described by Leung [30]: young particles have a significantly higher rate of coagulation than the older ones. This process is simultaneous with surface growth. The second one consists in the sticking of spherical particles into long chained structures. By the point of view of the dimensions, all these steps lead to the formation of structures whose lengths may reach 2 μm. It is also important to underline that during the exhaust stroke in a diesel engine, when the temperature falls below 500°C, particles get coated by gaseous components of low vapour pressure (sulphates for instance) [23]. For this reason, soot is generally considered to be composed by 2 parts: solid fraction (*SOL*) and soluble organic fraction (*SOF*). The latter can be separated by means of organic solvents (Fig. 1.7).

1.2.5 Oxidation

The are many ways to reduce the amount of soot released by a car, as, for instance, the diesel particulate filters (DPF). However, the best way to reduce it is to favour the soot oxidation while it is still inside the combustion chamber. Soot oxidation is a chemical surface reaction that always occurs while there are soot, a sufficiently high temperature (higher than 1300 K) and a certain oxygen concentration. Since

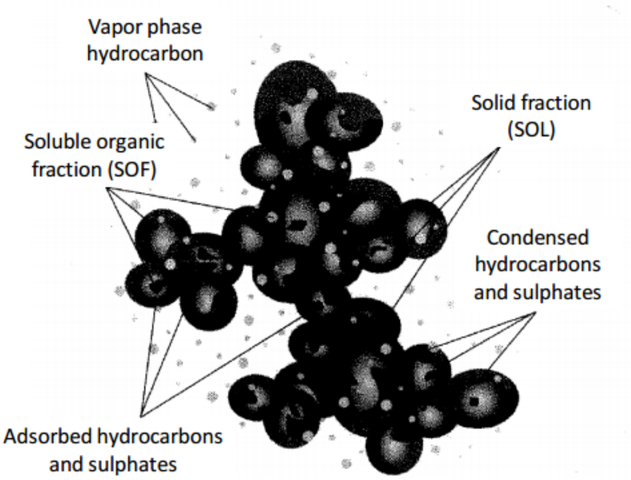

Figure 1.7: Diesel particulate structure [23]

soot is made mainly of carbon atoms, the products of its combustion are CO_2 and CO, that are desorbed from the soot particles, after a previous absorption of the oxidizer that reacts with the radical active sites. Since it always take place, also species like aromatics are oxidized. The main role here is played by O_2, while, for what concerns soot particles, even if it is not clear by a theoretical point of view, it seems that OH radicals are the most important oxidizing agent under stoichiometric or rich condition [13, 43, 46]. In lean conditions, both O_2 and OH are important. The effectiveness of the OH collision with the active sites is about $10 - 20\%$.

1.2.6 Soot particles classification

The very complex shape that soot agglomerates can assume can be simplified, for a sake of classification reason, considering its equivalent diameter D_p of a spherical particle sharing with the real particle the volume, surface or dynamic behaviour. Typically, there are 3 groups into which soot can be divided according to particles size:

- *single nuclei* ($D_p < 50$ nm): very large in number in a soot cloud, but, due to the very small dimension, their contribution to the total mass is negligible. The normalized concentration of number-weighted particles presents a peak around $10 - 30$ nm
- *particles* ($D_p = 50 - 1000$ nm): less in number, but they give the biggest contribution in terms of total mass, with a normalized peak around $100 - 500$ nm
- *agglomerates* ($D_p > 1000$ nm): in general, they are not direct product of combustion, but they are deposits on valves or surface of the combustion chamber that are taken away by the exhaust gases

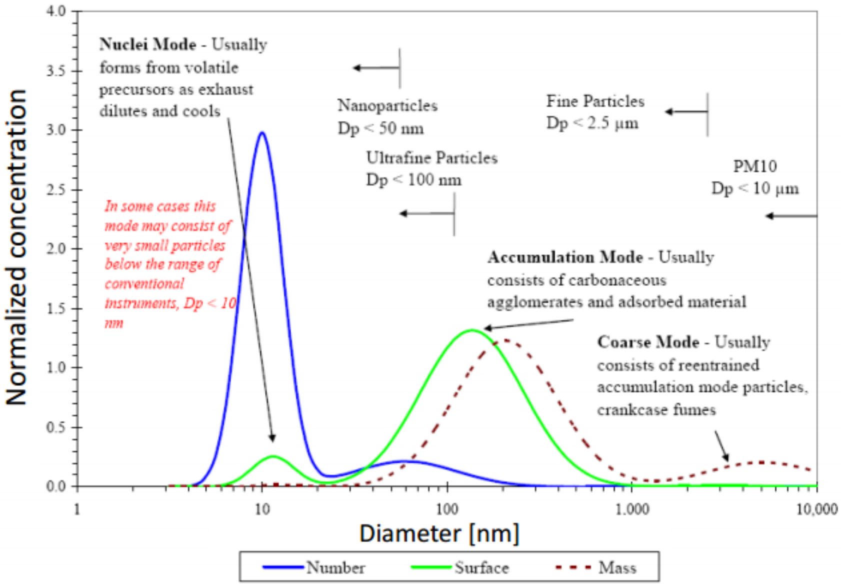

Figure 1.8: Particle size distribution in Diesel exhaust gases [23]

1.2.7 Soot health damages and current legislation

The effect of soot on human health has been recognized since 1775, in England, when it was found that the main cause of scrotum carcinoma in chimney sweepers was related to soot [5]. Nowadays, it is well known that the main impact of soot on human health is related to the damages on the breathing system. In particular, PAH of the soluble fraction is the main cause of these. The most used practical classification for soot particles, by a legislative point of view, is the following:

- *PM 10*: biggest particles, with a $D_p > 10^4$nm
- *PM 2.5*: commonly named fine particles, with a $D_p > 2500$ nm
- ultrafine particles: with a mean diameter lower than 100 nm
- nano-particles: whose mean diameter is lower than 50 nm

Decreasing its size, the particles become more dangerous, since the time in suspension in air is larger and our breathing system, with the natural filters of nose and bronchi that have retaining functions, does not work properly. Nano particles are the most dangerous. That is why DPF is not considered the best solution in soot retaining, since it is not able to trap them, and it is better to try to reduce soot amount inside the combustion chamber. Here (Fig. 1.9) it is reported the PM concentration in Europe in 2012.

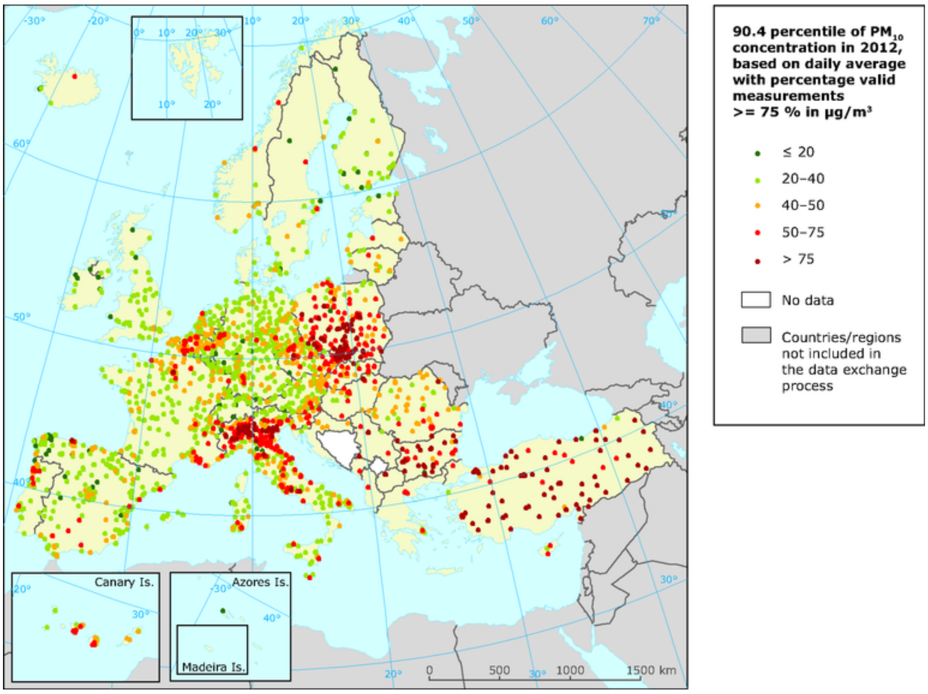

Figure 1.9: PM concentration in Europe (2012).

Current legislation about Diesel particulate emissions limits the total mass, but as said previously, most of the problems are related to small particles that give a small contribution in terms of mass.

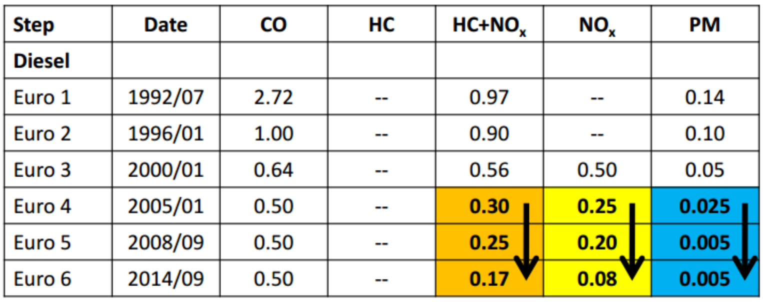

Step	**Date**	**CO**	**HC**	**HC+NO$_x$**	**NO$_x$**	**PM**
Diesel						
Euro 1	1992/07	2.72	--	0.97	--	0.14
Euro 2	1996/01	1.00	--	0.90	--	0.10
Euro 3	2000/01	0.64	--	0.56	0.50	0.05
Euro 4	2005/01	0.50	--	**0.30**	**0.25**	**0.025**
Euro 5	2008/09	0.50	--	**0.25**	**0.20**	**0.005**
Euro 6	2014/09	0.50	--	**0.17**	**0.08**	**0.005**

Figure 1.10: EU Emission Standards for Passengers Cars (Diesel Engines) [g/km]

As it is possible to see in Fig. 1.10, the amount of harmful species that can be emitted has been drastically reduced over the years. However, the main criticism to the actual measuring method is related to the fact that they are referred to a non realistic driving cycle (New European Driving Cycle, NEDC), that does not simulate the braking-acceleration cycles of a real vehicle. So starting from 2017 it will be substituted by a more accurate test, called Worldwide Harmonized Light Vehicles Test Procedure (WLTP) [6].

1.2.8 Control of diesel particulate emissions

Here the methods that can be adopted in order to reduce soot emissions in a Diesel engine are listed [23].

During combustion:

- reducing the quantity of fuel not mixed with air, controlling the equivalence ratio. This can be done decreasing the equivalence ratio or adopting multiple-injections
- increasing air fuel mixing by means of air turbulence and improved spray penetration
- lowering the combustion temperatures, compression or supercharging ratios, the heat losses in cooling system and the energy release in time

After combustion:

- make available oxygen in order to avoid small pockets of non aerated fuel
- keep high temperatures in order to complete oxidation reactions
- give enough time to make the reactions completed

Many of these actions unfortunately are bad from the point of view of performance and fuel saving. It is often preferred to use a DPF outside the combustion chamber. It consists in a honeycomb matrix able to catch the biggest soot particles and burn them completely after a certain number of engine cycles, thanks to a combustion process that is called regeneration. Although this element has been improved a lot over the years, in terms of reduced pressure drop and efficiency in soot catching, this solution is still not considered definitive.

Chapter 2

Combustion Modeling

In this chapter the main features of combustion and soot modeling are explained.

2.1 Combustion modeling

2.1.1 Governing equations

In combustion modeling, as in every fluid-dynamic problem, the governing equations are mathematical statements of physical conservation laws of mass, momentum and energy. Reacting flows have a changeable composition according to chemical reaction rates. So a mass conservation equation for each species must be added, causing an increase in the number of equations to be solved proportional to the number of species involved. In addition, an equation of state for each chemical species is added. Assuming thermodynamic equilibrium (in which a substance is described by two state variables by means of equations of state) and Newtonian fluid (for which the viscous stress is proportional to the gradient of velocity component), the system composed by the equations presented here is mathematically closed.

2.1.1.1 Continuity equation

This conservation equation is referred to a scalar property, the density ρ; written for only the gaseous phase:

$$\frac{\partial \rho}{\partial t} + \overrightarrow{\nabla} \cdot (\rho \overrightarrow{u}) = \rho \dot{S} \tag{2.1}$$

where $\dot{S}$ is the source term related to fuel spray evaporation. Since mass does not diffuse, diffusive term is not present.

2.1.1.2 Transport equation for chemical species

Each chemical species i in the domain has a transport equation in the form of:

$$\frac{\partial \rho Y_i}{\partial t} + \vec{\nabla} \cdot (\rho \vec{u} Y_i) = \vec{\nabla} \cdot \left(\rho D_i \vec{\nabla} Y_i\right) + \rho \dot{S}_i + \dot{\omega}_i \tag{2.2}$$

in which there are the variation in time, the convective term, the diffusive term and the source terms ($\dot{S}_i$ again takes into account the fuel spray evaporation, whereas $\dot{\omega}_i$ considers the generation/destruction rates of the i species due to chemical reactions).

2.1.1.3 Momentum equation

This conservation equation is referred to a vectorial property, $\rho\vec{u}$, and it takes into account the effect of the forces that act on the system. It can be written as:

$$\frac{\partial \rho \vec{u}}{\partial t} + \vec{\nabla} \cdot (\rho \vec{u} \vec{u}) = -\vec{\nabla} p + \vec{\nabla} \cdot \bar{\bar{\tau}} + \rho \vec{g} + \vec{f_s} \tag{2.3}$$

where there are the variation in time, the convective term, the pressure term, the divergence of the viscous shear stress tensor, the momentum source term due to the gravity acceleration (which is different from zero only for the momentum component in the direction along which acceleration acts) and the component related to the interaction between gaseous phase and the liquid spray.

In particular, the viscous shear stress tensor (that represents the internal friction force of fluid layers against each other) can be written as:

$$\bar{\bar{\tau}} = \mu \left[\left(\vec{\nabla} \vec{u} \right) + \left(\vec{\nabla} \vec{u} \right)^T - \frac{2}{3} \left(\vec{\nabla} \cdot \vec{u} \right) \bar{\bar{I}} \right] \tag{2.4}$$

where μ is the dynamic viscosity.

2.1.1.4 Energy conservation equation

Energy equation can be written in different ways. In case of combustion, where there are chemical reactions, it is useful to express it with respect to enthalpy:

$$h = \sum_{i=1}^{NS} Y_i \left(\triangle h^0_{f,i} + \int_{T_0}^{T} c_{p,i} dT \right) \tag{2.5}$$

so the energy conservation equation becomes:

$$\frac{\partial \rho h}{\partial t} + \vec{\nabla} \cdot (\rho \vec{u} h) = \frac{Dp}{Dt} - \vec{\nabla} \cdot \vec{J} + \dot{Q}_s - \dot{Q}_r \tag{2.6}$$

where $\dot{Q}_s$ is the heat exchange due to the presence of the liquid spray, while $\dot{Q}_r$ takes into account the radiative fluxes. For what concerns, $\vec{\nabla} \cdot \vec{J}$, it is the sum of the conductive flux and the one related to the chemical species diffusion:

$$\vec{J} = -\lambda \vec{\nabla} T + \sum_{i=1}^{NS} \vec{J_i} h_i \tag{2.7}$$

2.1.2 Turbulent combustion

Turbulence is still a very complex task to deal with in CFD problems and the great part of engineering problems are turbulent. Turbulent combustion is influenced by high heat release rates which cause strong flow accelerations through the flame front and by severe changes in kinematic viscosity due to significant temperature variations. On the other hand, turbulence modifies the flame structure and enhances chemical reaction rates. Different approaches are possible to deal with turbulence.

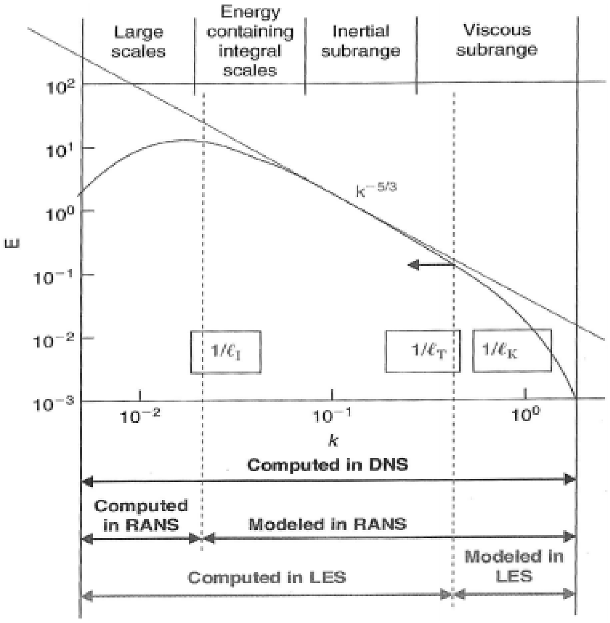

Figure 2.1: DNS, LES and RANS

The first consists in using Direct Numerical Simulations (DNS): here all scales of motion (down to Kolmogorov scale, at which turbulent kinetic energy is converted into heat) are solved using appropriate initial and boundary conditions for the flow. Results are very detailed, but computational costs are unfeasible for complex problems.

Then it is possible to use Large Eddy Simulations (LES): only larger scales of motion are solved, while the smallest ones are modelled. Required computational costs are lower with respect to DNS, but still too heavy for complex industrial applications.

The third method (the best from the computational effort point of view) consists in using Reynolds-Average-Navier-Stokes (RANS): here all the Navier-Stokes equations (Section 2.1.1) are averaged defining a generic flow property $f(t)$ as the sum of a steady mean quantity $\overline{f}$ and a time varying fluctuating component with zero mean value f':

$$f(t) = \overline{f} + f' \tag{2.8}$$

$$\overline{f} = \frac{1}{\triangle t}\int_0^{\triangle t} f dt \tag{2.9}$$

$$\overline{f'} = 0 \tag{2.10}$$

For compressible flow (as in combustion), instead of the Reynolds averaging (eq. 2.8), Favre averaging is used:

$$f(t) = \tilde{f} + f^{''} \tag{2.11}$$

$$\tilde{f} = \frac{\overline{\rho f}}{\overline{\rho}} \tag{2.12}$$

$$\widetilde{f^{''}} = 0 \tag{2.13}$$

So now all the equations shown before (Section 2.1.1) can be written according to RANS approach:

$$\frac{\partial \overline{\rho}}{\partial t} + \overrightarrow{\nabla} \cdot (\overline{\rho}\overrightarrow{u}) = \overline{\rho}\tilde{\dot{S}} \tag{2.14}$$

$$\frac{\partial \overline{\rho}\widetilde{Y_i}}{\partial t} + \overrightarrow{\nabla} \cdot \left(\overline{\rho}\widetilde{\overrightarrow{u}}\widetilde{Y_i}\right) = \overrightarrow{\nabla} \cdot \left(\overline{\rho D_i \overrightarrow{\nabla} Y_i}\right) + \overline{\rho}\widetilde{\dot{S}_i} + \widetilde{\dot{\omega}_i} - \overrightarrow{\nabla} \cdot \left(\overline{\rho}\widetilde{\overrightarrow{u^{''}} Y_s^{''}}\right) \tag{2.15}$$

$$\frac{\partial \overline{\rho}\widetilde{\overrightarrow{u}}}{\partial t} + \overrightarrow{\nabla} \cdot \left(\overline{\rho}\widetilde{\overrightarrow{u}\,\overrightarrow{u}}\right) = -\overrightarrow{\nabla}\overline{p} + \overrightarrow{\nabla} \cdot \overline{\overline{\overline{\tau}}} + \overline{\rho}\,\overrightarrow{g} + \widetilde{\overrightarrow{f_s}} - \overrightarrow{\nabla} \cdot \left(\overline{\rho}\overrightarrow{u^{''}}\overrightarrow{u^{''}}\right) \tag{2.16}$$

$$\frac{\partial \overline{\rho}\widetilde{h}}{\partial t} + \overrightarrow{\nabla} \cdot \left(\overline{\rho}\widetilde{\overrightarrow{u}}\widetilde{h}\right) = \frac{D\overline{p}}{Dt} - \overrightarrow{\nabla} \cdot \overrightarrow{\overline{J}} + \widetilde{\dot{Q}_s} - \widetilde{\dot{Q}_r} - \overrightarrow{\nabla} \cdot \left(\overline{\rho}\widetilde{\overrightarrow{u^{''}} h^{''}}\right) \tag{2.17}$$

In all the equations (except for continuity), extra terms appear after the averaging procedure. These terms, that can be seen as turbulent fluxes, must be modeled in order to close the problem.

2.1.3 Closure problem

The majority of the models used to close the problem are based on the physical effect of turbulence on mean flow properties: the presence of vortex eddy motions enhances transportation, mixing of momentum and energy and thus the associated unclosed terms are considered as source terms. These can be divided in 2 groups: *stress transport models* and *eddy viscosity models*. The models that belong to the first group require high computational time and sometimes are unstable, so the eddy viscosity ones can be used due to their low CPU consuming and their robustness. For example Spalart-Allmaras model, $k-\varepsilon$ model and $k-\omega$ model belong to the latter group. They are based on the Boussinesq hypothesis, which considers the Reynolds stress proportional to the mean rates of deformation:

$$-\overline{\rho}\widetilde{u_j''u_i''} = \mu_t \left(\frac{\partial \widetilde{u_j''}}{\partial x_i} + \frac{\partial \widetilde{u_i''}}{\partial x_j} - \frac{2}{3}\delta_{ij}\frac{\partial \widetilde{u_k''}}{\partial x_k} \right) + \frac{2}{3}\overline{\rho}k \tag{2.18}$$

$$-\overline{\rho}\widetilde{u_i''Y_k''} = \frac{\mu_t}{Sc_{t,k}}\frac{\partial \widetilde{Y_k}}{\partial x_i} \tag{2.19}$$

$$\overline{\rho}\widetilde{u_i''h''} = \frac{\mu_t}{Pr_t}\frac{\partial \widetilde{h}}{\partial x_i} \tag{2.20}$$

where μ_t is the turbulent or eddy viscosity, $k = \sum_{i=1}^{3}\frac{1}{2}\widetilde{u_j''u_i''}$ is the turbulent kinetic energy and δ_{ij} is the Kronecker delta. Pr_t is the turbulent Prandtl number (usually assumed equal to 0.85) and $Sc_{t,k}$ is the turbulent Schmidt number of the $k-th$ species (it can vary from 0.2 to 1.5):

$$Pr_t = \frac{\nu_t}{\alpha_t} \tag{2.21}$$

$$Sc_{t,k} = \frac{\nu_t}{D_{t,k}} \tag{2.22}$$

For what concerns μ_t, its definition depends on the used turbulence model. For $k-\varepsilon$ model:

$$\mu_t = \overline{\rho}C_\mu\frac{k^2}{\varepsilon} \tag{2.23}$$

in which k is the turbulent kinetic energy and ε is its dissipation rate. They are obtained solving two transport equations:

$$\frac{\partial \overline{\rho}k}{\partial t} + \frac{\partial \overline{\rho}\widetilde{u}_i k}{\partial x_i} = \frac{\partial}{\partial x_i}\left[\left(\mu + \frac{\mu_t}{\sigma_k}\right)\frac{\partial k}{\partial x_i}\right] - \overline{\rho}\widetilde{u_j''u_i''}\frac{\partial \widetilde{u}_i}{\partial x_j} - \overline{\rho}\varepsilon \tag{2.24}$$

$$\frac{\partial \overline{\rho}\varepsilon}{\partial t} + \frac{\partial \overline{\rho}\widetilde{u}_i\varepsilon}{\partial x_i} = \frac{\partial}{\partial x_i}\left[\left(\mu + \frac{\mu_t}{\sigma_\varepsilon}\right)\frac{\partial \varepsilon}{\partial x_i}\right] - C_{\varepsilon 1}\frac{\varepsilon}{k}\overline{\rho}\widetilde{u_j''u_i''}\frac{\partial \widetilde{u}_i}{\partial x_j} - C_{\varepsilon 2}\overline{\rho}\frac{\varepsilon^2}{k} \tag{2.25}$$

In which:

C_μ	σ_k	σ_ε	$C_{\varepsilon 1}$	$C_{\varepsilon 2}$
0.09	1.00	1.30	1.44	1.92

Table 2.1: Constant for $k-\varepsilon$ model

It worths to underline that $k-\varepsilon$ model works very well far from the wall. While at the wall ε equation 2.25 is singular (due to $\frac{\varepsilon^2}{k}$ term), so wall functions must be used. Due to these characteristics, it is suitable for application in which what happens at the wall is not so relevant (e.g. combustion in a vessel), while it is not suitable, for example, if the behaviour at the wall is crucial (e.g. analysis of the stall in a compressor: other models such as Spalart-Allmaras and $k-\omega$ should be used).

The closure of RANS equations needs turbulence models to deal with turbulent fluctuations and turbulent combustion models to describe chemical species conversion and heat release. Whereas the first ones have been just presented, now the idea that stays behind the modeling of turbulent combustion [41], is explained.

In particular, in the next Sections the three combustion models employed in this work are presented:

- RIF model (Section 2.2): a direct-integration model with turbulence-chemistry interaction

- TWM model (Section 2.3.1): a tabulated chemistry model without turbulence-chemistry interaction

- TRIF model (Section 2.3.2): a tabulated chemistry model with turbulence-chemistry interaction

2.2 Representative Interactive Flamelet (RIF) model

2.2.1 Flamelet concept

Complex phenomena that happen during combustion can be modeled using the laminar flamelet concept, proposed by Peters [41]. According to it, turbulent flames can be seen as an ensamble of stretched laminar flamelets. This concept covers a regime in turbulent combustion where chemistry, as compared to transport processes, is fast enough that it occurs in thin layers, called flamelets, embedded within the turbulent flow fields, i.e. the laminar flame structure is stretched and distorted by turbulent eddies but it is preserved (Fig. 2.2). Thus, the flame can be treated as an ensable of laminar counterflow diffusion flamelets where chemical reactions occur. This assumption of fast chemistry is suitable for diffusion flames, since the overall reaction rate is limited by species diffusion towards the flame front.

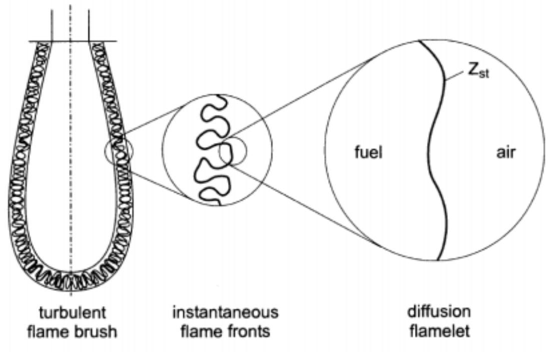

Figure 2.2: Laminar flamelet concept [24]

So basically, thanks to this approach, turbulent flames are locally stretched and so they can be studied using a monodimensional model. Resuming, two domains are used:

- the *physical* one, in which the classic trasport equations and the equations for the mixture fraction are solved
- the *chemical* one, where the flamelet equations (based on mixture fraction Z and on the scalar dissipation rate χ) are solved

Now, before introducing flamelet equations, it worths to remind some concepts regarding Z and χ.

2.2.1.1 Mixture fraction Z

This scalar parameter describes the mixing between air and fuel in a non-premixed flame. In particular, it is defined as the ratio of the mass of all elements originated from the fuel stream and the sum of both mass fluxes of air and fuel. Therefore an index of the local air-fuel ratio. In the physical domain its trasport equations are solved. The main steps to achieve them are here reported [55].

Under the hypotesis of constant pressure, low Mach number, diffusion coefficient D_i and specific heat $c_{p,i}$ equal for all the species, it is possible to write a generic simplified reaction as:

$$\nu_F F + \nu_O O \rightleftarrows \nu_P P \tag{2.26}$$

and rewrite the transport equations for energy, fuel mass and oxidixer mass as:

$$\frac{\partial \rho Y_F}{\partial t} + \frac{\partial \rho u_i Y_F}{\partial x_i} = \frac{\partial}{\partial x_i}\left(\rho D \frac{\partial Y_F}{\partial x_i}\right) + \dot{\omega}_F \tag{2.27}$$

$$\frac{\partial \rho Y_O}{\partial t} + \frac{\partial \rho u_i Y_O}{\partial x_i} = \frac{\partial}{\partial x_i}\left(\rho D \frac{\partial Y_O}{\partial x_i}\right) + s\dot{\omega}_F \tag{2.28}$$

$$\frac{\partial \rho T}{\partial t} + \frac{\partial \rho u_i T}{\partial x_i} = \frac{\partial}{\partial x_i}\left(\frac{\lambda}{c_p}\frac{\partial Y_F}{\partial x_i}\right) + \frac{Q}{c_p}\dot{\omega}_F \tag{2.29}$$

where $\dot{\omega_F}$ is the fuel reaction rate, Q is the heat released per unit of fuel mass and s is defined as:

$$s = \frac{\nu_O W_O}{\nu_F W_F} \tag{2.30}$$

Combining these equations and assuming a Lewis number (that is the ratio between thermal diffusivity and mass diffusivity) equal to 1:

$$Le = \frac{\alpha}{D} = \frac{\lambda}{\rho c_p D} = 1 \tag{2.31}$$

three conserved scalars appear:

$$z_1 = sY_F - Y_O \tag{2.32}$$

$$z_2 = \frac{c_p T}{Q} + Y_F \tag{2.33}$$

$$z_3 = s\frac{c_p T}{Q} + Y_O \tag{2.34}$$

that follows the same advective-diffusive transport equation (with $j = 1, 2, 3$):

$$\frac{\partial \rho z_j}{\partial t} + \frac{\partial \rho u_i z_j}{\partial x_i} = \frac{\partial}{\partial x_i}\left(\rho D \frac{\partial z_j}{\partial x_i}\right) \tag{2.35}$$

These three conserved scalars have different boundary conditions, so they are normalized in order to have boundary condition equal to 1 at the fuel side and 0 at the oxidizier side. The new obtained scalars are Z_j:

$$Z_j = \frac{z_j - z_j^O}{z_j^F - z_j^O} \tag{2.36}$$

These new scalars have the same boundary conditions and they follow the same trasport equation, so they can be considered as the mixture fraction Z, which trasport equation is:

$$\frac{\partial \rho Z}{\partial t} + \frac{\partial \rho u_i Z}{\partial x_i} = \frac{\partial}{\partial x_i}\left(\rho D_Z \frac{\partial Z}{\partial x_i}\right) + \rho\dot{S} \tag{2.37}$$

where D_z is the mixture fraction diffusivity and $\rho\dot{S}$ is the source term associated to the fuel spray evaporation. As it has been done for all the trasport equations, also this one should be averaged using the Favre average:

$$\frac{\partial\overline{\rho}\widetilde{Z}}{\partial t}+\frac{\partial\overline{\rho}\widetilde{u}_i\widetilde{Z}}{\partial x_i}=\overline{\rho}\widetilde{\dot{S}}-\frac{\partial\overline{\rho}\widetilde{u_i''Z''}}{\partial x_i} \tag{2.38}$$

The transport equation for the mixture fraction needs a further transport equation for the mixture fraction variance $\widetilde{Z''^2}$. This transport equation is in the form of:

$$\frac{\partial\overline{\rho}\widetilde{Z''^2}}{\partial t}+\frac{\partial\overline{\rho}\widetilde{u}_i\widetilde{Z''^2}}{\partial x_i}=-\frac{\partial\overline{\rho}\widetilde{u_i''Z''^2}}{\partial x_i}-2\left(\overline{\rho}\widetilde{u_{ii}''Z''}\right)\frac{\partial\widetilde{Z}}{\partial x_i}-2\overline{\rho}D_Z\widetilde{\left(\frac{\partial Z''}{\partial x_i}\right)^2}+2\left(1-Z\right)\overline{\rho}\widetilde{Z''\dot{S}}-\overline{\rho}\widetilde{Z''^2\dot{S}} \tag{2.39}$$

2.2.1.2 Scalar dissipation rate χ

The instantaneous scalar dissipation rate measures the gradient of Z and the molecular fluxes of species towards the flame; it is defined as:

$$\chi=2D_Z\left(\frac{\partial Z}{\partial x_i}\right)^2 \tag{2.40}$$

The scalar dissipation rate is the only parameter depending on spatial variables and represents the influence of flow field and mixing on flamelet structure. It can be considered as the term which accounts for the departure from chemical equilibrium [58]. For this reason, its reciprocal is a measure of diffusive time: for long diffusion time (low χ), chemical conditions are close to equilibrium, whilst a very high rate stands for extreme strained flame, near extinction.

The averaged scalar dissipation rate is:

$$\widetilde{\chi}=2D_Z\widetilde{\left(\frac{\partial Z''}{\partial x_i}\right)^2} \tag{2.41}$$

2.2.2 Laminar flamelet equations

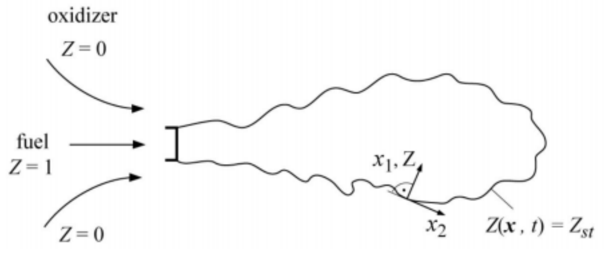

Figure 2.3: Physical and chemical domains

By definition, Z is defined locally normal to the reaction zone (almost corresponding to the stoichiometric mixture). Therefore, considering Z as one coordinate and the other two (x_1 and x_2 (Fig. 2.3)) lying within the reaction zone, the conservation equations for species mass fractions and temperature can be transformed into the new coordinate system: in theory there is no reduction of the number of variables. But a simplification can be done assuming that:

- flame front is located where there is a stoichiometric mixture
- flame front is very thin if compared to turbulent flame front corrugation and to the dimensions of the mean flux structures

If these assumptions are accepted, gradients along x_1 and x_2 are negligible, so the introduction of the mixture fraction allows to write temperature and chemical composition as function only of time and Z:

$$Y_i = Y_i\left(\overrightarrow{x}, t\right) \Longrightarrow Y_i = Y_i(Z, t) \tag{2.42}$$

$$T = T(\overrightarrow{x}, t) \Longrightarrow T = T(Z, t) \tag{2.43}$$

So now it is possible to rewrite energy equation and transport equation for chemical species as [9]:

$$\rho\frac{\partial Y_i}{\partial t} - \rho\frac{\chi}{2Le_i}\frac{\partial^2 Y_i}{\partial Z^2} = \dot{\omega}_i \tag{2.44}$$

$$\rho\frac{\partial T}{\partial t} - \rho\frac{\chi}{2}\frac{\partial^2 T}{\partial t^2} - \rho\frac{\chi}{2c_p}\frac{\partial T}{\partial Z}\frac{\partial c_p}{\partial Z} - \sum_{i=1}^{NS}\rho\frac{\chi}{2Le_i}\frac{c_{p_i}}{c_p}\frac{\partial Y_i}{\partial Z}\frac{\partial T}{\partial Z} + \frac{1}{c_p}\sum_{i=1}^{NS}\dot{\omega}_i h_i - \frac{1}{c_p}\frac{\partial p}{\partial t} - \frac{\dot{q}_r}{c_p} = 0 \tag{2.45}$$

in which there are the specific heat of the i-th species c_{p_i}, the specific heat of the mixture c_p, the production rate of the i-th species $\dot{\omega}_i$ (expressed in $\left[\frac{Kg}{m^3 s}\right]$), the thermochemical enthalpy of the i-th species h_i, the radiative heat $\dot{q}_r$ and the Lewis number of the i-th species Le_i, supposed to be equal to 1 [40].

2.2.2.1 Flamelet domain initialization

Flamelet domain, as the CFD one, needs boundary and initial conditions. It is difficult to say a priori what is the distribution of chemical species, enthalpy and temperature in the Z domain: so for the initial conditions the hypothesis of *pure mixing* is done:

$$Y_i(Z) = (1 - Z)Y_i^O + Z\,Y_i^F \tag{2.46}$$

$$h_s(Z) = (1 - Z)h_s^O + Z\,h_s^F \tag{2.47}$$

Enthaply and chemical species profiles are evaluated starting from a linear profile considering $Z = 0$ (oxydizer side) and $Z = 1$ (fuel side), imposing a pure mixing: what it is obtained is a linear profile for enthalpy in Z domain, whereas temperature profile is non linear (since c_p changes according to chemical composition). Y_i^O is the mass fraction of i-th species in the air stream (usually only N_2, O_2, H_2O and CO_2 are considered) and Y_i^F is the mass composition of fuel stream. Y_i^O and Y_i^F are also the boundary conditions for compositions and they are kept fixed during the simulation. The temperature profile in the Z domain is estimated from the local enthalpy and composition. In relation to boundary conditions, T_{fuel} is kept fixed throughout the simulation, whereas temperature on the air side changes according to $\frac{dp}{dt}$.

2.2.2.2 Coupling between CFD and flamelet domains

A flamelet based approach defines the time evolution of all reacting scalar as a function of Z. The Favre average composition in the physical domain (CFD) can be assessed from composition in the Z domain by means of a probability density function (PDF) of the mixture fraction. The PDF may be either a solution of transport equations or presumed by assuming structure and randomness of the flow field. In this work, as in many engineering studies, the presumed β-PDF is used (Fig. 2.4), which is calculated as:

$$\widetilde{P}\left(Z; \overrightarrow{x}, t\right) = \frac{Z^{\alpha-1}\left(1-Z\right)^{\beta-1}}{\Gamma(\alpha)\,\Gamma(\beta)}\Gamma(\alpha+\beta) \tag{2.48}$$

where:

$$\Gamma(z) = \int_0^{+\infty} t^{z-1} exp(-t)\, dt \tag{2.49}$$

$$\alpha = \widetilde{Z}\gamma \tag{2.50}$$

$$\beta = \left(1 - \widetilde{Z}\right)\gamma \tag{2.51}$$

and

$$\gamma = \frac{\widetilde{Z}\left(1 - \widetilde{Z}\right)}{\widetilde{Z''^2}} - 1 \tag{2.52}$$

For $\alpha < 1$, $\widetilde{P}(Z)$ has a vertical asymptote at $Z = 0$, for $\beta < 1$ the asymptote is at $Z = 1$ whereas for both $\alpha < 1$ and $\beta < 1$ the function has 2 asymptotes in $Z = 0$ and $Z = 1$.

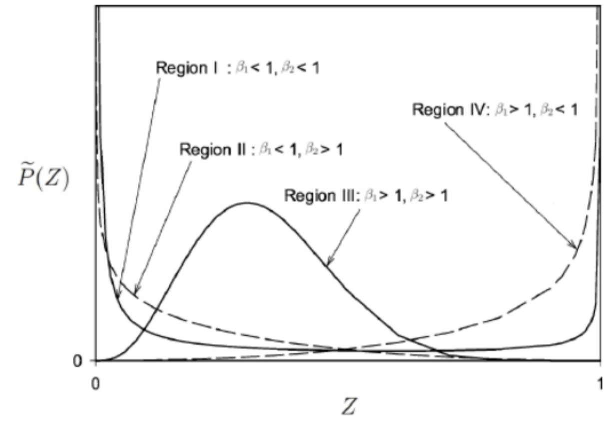

Figure 2.4: β-PDF function (where β_1 corresponds to α and β_2 to β)

It is interesting to underline, looking at Fig. 2.4, that the so-called *Region I* is typical of a young flamelet, where fuel and oxidizer streams are still separated. Otherwise an old flamelet has a PDF with a shape similar to the *Region III*, where a peak at approximatively stoichiometric mixture indicates that fuel vapour and oxidizer are well mixed.

In order to evaluate the β-PDF, transport equations for both $\widetilde{Z}$ (eq. 2.38) and $\widetilde{Z''^2}$ (eq. 2.39) must be solved. As it happens for RANS equations, also in this case a closure model is needed. The new transport equations are so:

$$\frac{\partial \overline{\rho}\widetilde{Z}}{\partial t} + \frac{\partial \overline{\rho}\widetilde{u}_i\widetilde{Z}}{\partial x_i} = \frac{\partial}{\partial x_i}\left(\frac{\mu_t}{Sc_{t,\widetilde{Z}}}\frac{\partial \widetilde{Z}}{\partial x_i}\right) + \overline{\rho}\widetilde{\dot{S}} \tag{2.53}$$

$$\frac{\partial \overline{\rho}\widetilde{Z''^2}}{\partial t} + \frac{\partial \overline{\rho}\widetilde{u}_i\widetilde{Z''^2}}{\partial x_i} = \frac{\partial}{\partial x_i}\left(\frac{\mu_t}{Sc_{t,\widetilde{Z''^2}}}\frac{\partial \widetilde{Z''^2}}{\partial x_i}\right) + 2\frac{\mu_t}{Sc_{t,\widetilde{Z}}}\left(\frac{\partial \widetilde{Z}}{\partial x_i}\right)^2 - \rho\widetilde{\chi} + 2\left(1 - Z\right)\overline{\rho}\widetilde{Z''\dot{S}} - \overline{\rho}\widetilde{Z''^2\dot{S}} \tag{2.54}$$

in which $Sc_{t,\widetilde{Z}}$ and $Sc_{t,\widetilde{Z''^2}}$ are the turbulent Schimdt numbers, set equal to 0.85 whereas $\widetilde{\chi}$ is the average scalar dissipation rate (the one seen in eq. 2.41). Since the average scalar dissipation rate acts for Z the same role of ε for turbulent kinetic energy, this analogy is used to model $\widetilde{\chi}$ using a relation that expresses proportionality between scalar dissipation rate and turbulence dissipation time:

$$\widetilde{\chi} = c_\chi \frac{\widetilde{\varepsilon}}{\widetilde{k}}\widetilde{Z''^2} \tag{2.55}$$

where, introducing the integral time scale $\tau_L = \frac{k}{\varepsilon}$ and the scale $\tau_Z = \frac{\widetilde{Z''^2}}{\widetilde{\chi}}$, c_χ is the ratio between them:

$$c_\chi = \frac{\tau_L}{\tau_Z} \tag{2.56}$$

c_χ is set equal to 2.

Once the solution in the flamelet domain is calculated and the β-PDF is known, the mass fractions of each chemical species in the CFD domain can be computed without solving any chemical reaction in the CFD domain:

$$\widetilde{Y}_i\left(\overrightarrow{x},t\right) = \int_0^1 \widetilde{P}\left(Z;\ \overrightarrow{x},t\right) Y_i\left(Z,t\right)\,dZ \tag{2.57}$$

Then temperature field is calculated iteratively combining $\widetilde{h}$ (obtained solving RANS equations) and $\widetilde{Y}_i$:

$$\widetilde{h}\left(\overrightarrow{x},t\right) = \sum_{i=1}^{NS} \widetilde{Y}_i\left(\overrightarrow{x},t\right) h_i\left(\widetilde{T}\left(\overrightarrow{x},t\right)\right) \tag{2.58}$$

where h_i is the thermochemical enthalpy of the i-th species.

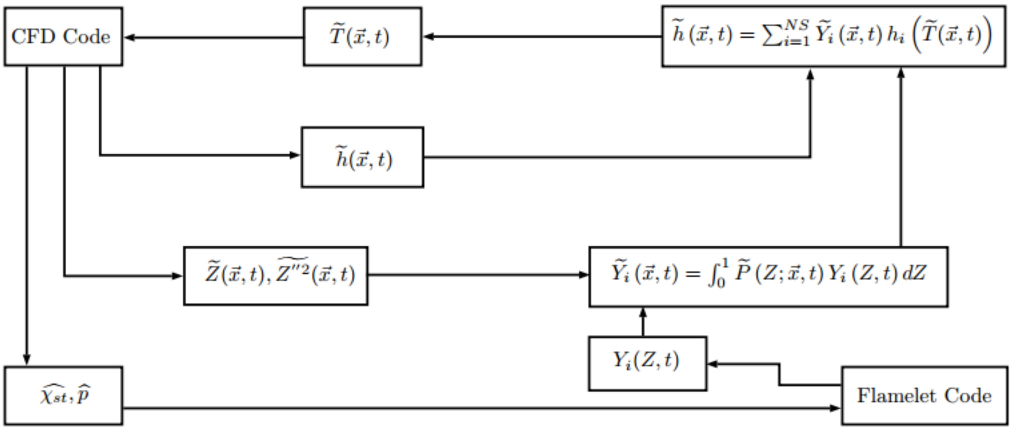

(a) Without virtual species.

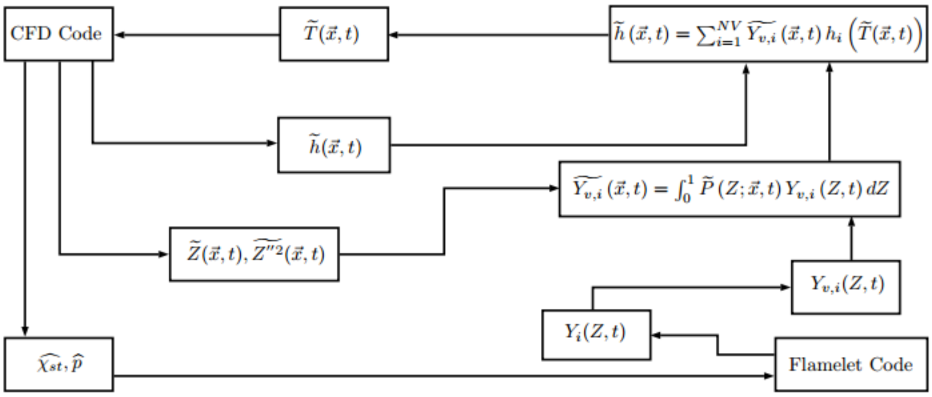

(b) With virtual species.

Figure 2.5: RIF structure

However, in order to reduce the computational time required by the simulations, the virtual species approach is adopted: a reduced set of chemical species (N_2,

O_2, $fuel$, CO_2, CO, H_2O, H_2) is introduced, and its distribution $\widetilde{Y_{v,i}}\left(\overrightarrow{x},t\right)$ in the CFD domain is calculated integrating the β-PDF starting from their distribution in the flamelet domain $Y_{v,i}\left(Z,t\right)$, which in turn is calculated from the solution of the complete mechanism $Y_i\left(Z,t\right)$. Of course, this process must guarantee mass and thermodynamic properties conservation. For further informations, see next Section 2.3.

Looking at the structure of RIF model, in Fig. 2.5 it is possible to see what are the differences using virtual species or not.

2.3 Tabulated mechanisms

The required time to perform an entire simulation with the already described RIF model can be too long to be suitable for industrial applications, so it is somehow necessary to try to reduce it. However, this task may be very complex if it is required also to compute carefully some aspects such as flame structure and pollutant formation. In order to get this, detailed kinetics must be present. So the adoption of tabulated kinetics in combustion modeling is one of the main focus of this work. The basic concept of tabulation is that chemical species reaction rates are stored in a table according to the mechanism and flame structure, that can be:

- TWM: Tabulated Well-Mixed model
- TRIF: Tabulated Representative Interactive Flamelet model
- TPPDF: Tabulated Presumed PDF model

Only the first and the second were used in the simulations for this work, since as suggested by [36], the adoption of a probability density function (that is fundamental to include the turbulence-chemistry interaction) did not lead to significant improvement in terms of results with respect to the TWM. The only advantage was a better estimation of the lift-off length. TRIF instead includes turbulence-chemistry interaction.

As said before, in both the models, the reaction rates of the chemical reactions are calculated in a different way with respect to RIF. In the latter, they are computed by direct-integration of the conservation equations using very short temporal intervals ($10^{-7} - 10^{-9}$ s), giving very wide flexibility in terms of adoptable fuel or operating condition, with a penalty in computational time. These very small scales are necessary since chemical characteristic times are much smaller than the fluid-dynamic ones, demanding very stiff ODE solvers. Nowadays, the maximum number of species that can be handled is around 100. This may lead to some uncertainity in predicting some pollutant or soot precursors. The main features of RIF were already described (Section 2.2), so no other words are necessary to explain how it couples chemical and CFD (physical) domains.

In the models that use tabulation, chemical composition and other useful variables (as pressure and temperature) are stored in tables in function of a variable called progress variable. By its integration, it is possible to reconstruct the chemical composition and the reaction rates everywhere without solving transport equations for each species.

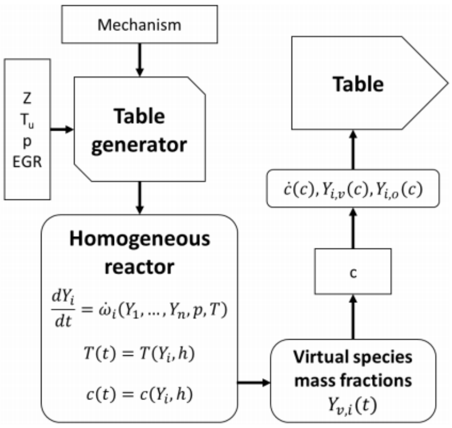

Figure 2.6: Generation of chemistry table (based on homogeneous reactor assumption)

Chemistry is tabulated according to the approach in Fig. 2.6. First, the mechanism and a range of initial conditions are imposed, including mixture fraction Z, ambient pressure p, initial reactor temperature T_u and residual gas fraction EGR. The reactor temperature is initialized considering a dependence with the mixture fraction of this kind (recalling that the enthalpy of the mixture is a function of temperature):

$$h(Z) = (1 - Z) \cdot h(T_{Z=0}) + Z \cdot h(T_{Z=1}) - Z \cdot h_l(T_{Z=1}) \tag{2.59}$$

where h_l that is the fuel heat of vaporization, remembering that Z goes from 0 (only air) to 1 (only fuel). This method offers the chance of better reproducing the thermochemical state of the system, since the possibility of considering both the effect of mixing and evaparation of the fuel, in the moment the table is generated, is included. This is true because changing the amount of injected fuel (that is colder), the temperature of the mixture that is formed is different, so also the enthalpy depends on the mixture fraction distribution (mixing line assumption).

In any specified condition, the reaction rates of every chemical species are solved:

$$\frac{dY_i}{dt} = \dot{\omega}_i(T, p, Y_1, ..., Y_n) \tag{2.60}$$

The temperature is computed from the initial enthalpy value. At every time step, the progress variable C and the chemical composition must be evaluated, using the virtual species approach. There are several definition for the progress variable, that must well represent the combustion progress. There are 3 key rules that it must satisfy [36]:

- it must be transportable in the fluid-dynamic domain
- the used scalar must evolve with comparable time scales
- in each time step its value must represent a single thermodynamic state

There are also 3 possible choices that can be used in the model, however here only the best one (according to Lehtiniemi et al. [18]) is used:

$$C = \sum_{i=1}^{N_s} h_{298,i} \cdot Y_i(t) - \sum_{i=1}^{N_s} h_{298,i} \cdot Y_i(0) \tag{2.61}$$

This formula represents the difference between the current and the initial value of the reactor formation enthalpy, summing up the contributions of all the species.

At the end of the calculation, its rate and the chemical composition are stored in function of a normalized value of C, called c:

$$c = \frac{C - C_{min}}{C_{max} - C_{min}} \tag{2.62}$$

where C_{min} is the value of the progress variable at initial condition and C_{max} is its value after auto-ignition condition. In the table, they are stored in function of Z, T_u and p. Its reaction rate is calculated with forward differencing scheme:

$$\dot{c_i} = \frac{c_{i+1} - c_i}{t_{i+1} - t_i} \tag{2.63}$$

This term has some boundary conditions, as for instance if the end of combustion is considered. The progress variable has its own transport equation, so to make it suitable for that, it must be multiplied by $C(t_{end}) - C(0)$ to get a $\dot{C}$ term. With the progress variable value, also chemical composition has to be stored, but in order to not exagerate with the dimension of the stored table (that would be huge if all the possible species were conserved) also here the virtual species approach is applied. They are a set of 7 species, N_2, O_2, $fuel$, CO_2, CO, H_2O, H_2, whose mass fractions are computed in order to preserve the main thermochemical properties of the whole set used in the detailed mechanism. For each c value, their composition is calculated, recalling that the total number of elements must be preserved, so, for example, the number of hydrogen atoms of all the virtual species must be the same of the number of hydrogen atoms of the real species. The same concept applies to all the elements. Moreover, the conservation of the total enthalpy h (considering again the contributions to the mass fractions of the real species and the virtual ones) and the equivalence of the mass specific heats c_p calculated once with the real, once with the virtual ones, must be guaranteed:

$$h = \sum_{i=1}^{N_s} Y_i \cdot c_{p,i}(T) = \sum_{k=1}^{N_v} Y_{i,v} \cdot c_{p,k}(T) \tag{2.64}$$

$$c_p = \sum_{i=1}^{N_s} Y_i \cdot c_{p,i}(T) = \sum_{k=1}^{N_v} Y_{i,v} \cdot c_{p,k}(T) \tag{2.65}$$

The left part of the equations refers to the real species, the right the virtual ones. In addition to the virtual species, selecting properly the desired elements in the output species in the software, it is possible to store in the table also the mass fractions of the species required for post-processing, as for example OH, C_2H_2, C_6H_6 and so on.

It must be underlined that tabulation introduces a strong simplification with respect to direct-integration because the problem dimensions pass from N_s+2 (number of species, enthalpy and pressure) to only four. This fact affects the ignition process when C is diffused to rich mixtures ($\phi > 3$) that have a longer ignition delay and a very fast single stage ignition. This leads to rich regions that ignites almost immediately and high values of C will diffuse back to leaner or stoichiometric regions, causing an anticipated auto-ignition. In order to avoid this, reaction rates are set equal to zero in regions where dual-stage ignition does not happen (so where $\phi > 3$). Of course this phenomenon has negative effects on soot prediction, because rich mixture is involved in soot generation process (see Section 1.2.1).

2.3.1 Tabulated Well-Mixed (TWM) model

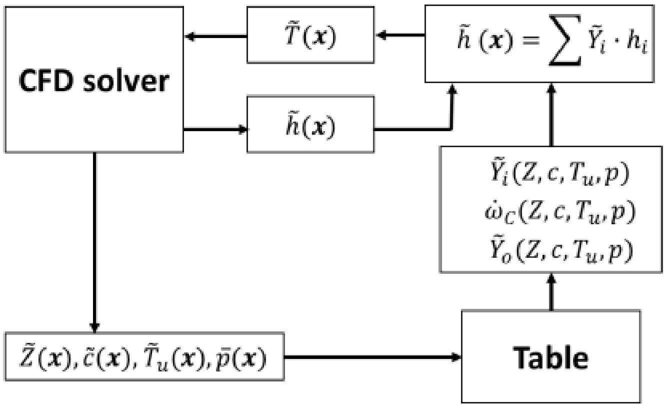

Figure 2.7: Structure of TWM model

With the Well-Mixed approach, each cell in the CFD domain (the only one that is used) is schematized as a homogeneous reactor identified by unburned gas temperature, pressure and mixture fraction values and there is no turbulence-chemistry interaction, i.e. the mean chemical source term is evaluated using directly the mean temperature and composition, neglecting turbulent fluctuations. Moreover, the variation in time of energy and mass fractions are caused only by source terms since reactor geometry is a simple cell with homogeneous composition. In several works it was shown that this model, coupled with chemistry direct-integration, gives satisfactory results in non-premixed flame simulations [34] demonstrating that turbulence-chemistry interaction is not fundamental. So it is interesting to evaluate how the Well-Mixed behaves if coupled with the tabulated chemistry: in this case, it works as indicated in Fig. 2.7. Transport equations for mixture fraction, enthalpy, unburned gas temperature and progress variable are solved in the CFD domain, then the table is accessed with the local cell values. Interpolation of table values at cell conditions is performed by means of an inverse, distance weighted technique. Mixture fraction equation (the same seen in 2.37), includes fuel evaporation.

The progress variable source term $\dot{C}$ used in the transport equation is derived from eq. 2.63:

$$\frac{\partial \rho C}{\partial t} + \frac{\partial}{\partial x_i}\left(\rho \overrightarrow{u} C\right) - \frac{\partial}{\partial x_i}\left(\frac{\mu_t}{Sc_t}\frac{\partial C}{\partial x_i}\right) = \rho \dot{C} \tag{2.66}$$

$$\dot{C} = \left(C_{max} - C_{min}\right)\dot{c} \tag{2.67}$$

To access the table data, it is necessary to solve an additional equation for the unburned gas enthalpy, which is then used to estimate the unburned gas temperature T_u (which is one of the independent variables of the table):

$$\frac{\partial \rho h_u}{\partial t} + \frac{\partial}{\partial x_i}\left(\rho \overrightarrow{u} h_u\right) - \frac{\partial}{\partial x_i}\left(\alpha_t \frac{\partial h_u}{\partial x_i}\right) = \dot{Q}_s + \frac{\rho}{\rho_u}\cdot\frac{D_p}{D_t} \tag{2.68}$$

where α_t is the turbulent thermal diffusivity and ρ_u is the unburned gas density which is computed looking at cell pressure, chemical composition at $C = 0$ and T_u. $\dot{Q}_s$ is the term related to spray evaporation, and its values depend on the fact that mixing line is assumed or not in the table generation process (2.3).

2.3.2 Tabulated Representative Interactive Flamelet (TRIF) model

This model, as the RIF one, is based on the laminar flamelet concept. As already said, the most important assumption is that the smallest turbulent time and length scales are bigger than the chemical ones. So it exists a region called flamelet where reactions occur that can be seen as en ensamble of stretched counterflow diffusion flames (Fig. 2.8).

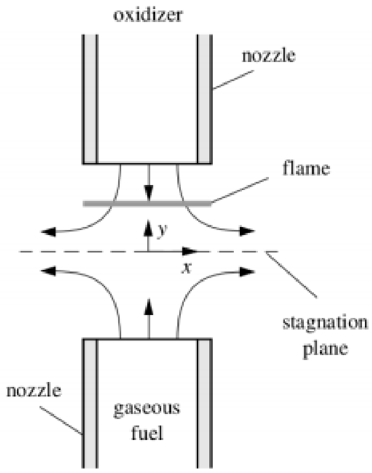

Figure 2.8: Schematic of a counterflow flame [40]

As it happens in RIF model, all reacting scalars only depend on Z (which, for non-premixed combustion, is related to the local air-fuel ratio) and the chemical composition is obtained from Z field in the CFD domain, assuming that its sub-grid distribution can be represented by a β-PDF function. Multiple number of flamelets can be used in order to achieve better results in terms of turbulence effects on the flame structure and prediction of flame stabilization. Each flamelet represents a certain portion of the injected fuel mass. Chemical composition in each cell is computed from mixture fraction and flamelet marker distribution as follows:

$$Y_i(\overrightarrow{x}) = \sum_{j=1}^{N_f} M_j \int_0^1 Y_{j,i}(\widetilde{Z}) P\left(\widetilde{Z}, \widetilde{Z''^2}\right) dZ \tag{2.69}$$

where N_f is the number of flamelets and $Y_{j,i}$ are the mass fractions in the $j-th$ flamelet domain.

For each flamelet marker, the following transport equation is solved:

$$\frac{\partial \rho \widetilde{M_j}}{\partial t} + \frac{\partial}{\partial x_i}\left(\rho \overrightarrow{u} \widetilde{M_j}\right) - \frac{\partial}{\partial x_i} \cdot \left(\frac{\mu_t}{Sc_Z} \frac{\partial}{\partial x_i} \widetilde{M_j}\right) = \dot{S}_{M_j} \tag{2.70}$$

where the source term $\dot{S}_{M_j}$ corresponds to $\dot{S}_Z$ only for specified interval of the injection duration, while it is zero elsewhere. In addition, flamelet markers must also satisfy the following relation:

$$Z = \sum_{j=1}^{N_f} M_j \tag{2.71}$$

The local flame structure is defined by the flamelet equations that are solved for the progress variable C and enthalpy assuming a Lewis number equal to 1 in the mixture fraction space:

$$\rho\frac{\partial C}{\partial t}=\rho\frac{\chi_Z}{2}\frac{\partial^2 C}{\partial Z^2}+\dot{C} \tag{2.72}$$

$$\rho\frac{\partial h}{\partial t}=\rho\frac{\chi_Z}{2}\frac{\partial^2 h}{\partial Z^2}+\frac{dp}{dt} \tag{2.73}$$

The chemical composition in the mixture fraction space is recalled from the chemistry table in the same way as for TMW model in the CFD domain. The scalar dissipation rate χ_Z (which is function of the scalar dissipation rate at stoichiometric mixture fraction conditions $\widetilde{\chi_{st,j}}$, computed for each flamelet) contains the effects of mixing related to turbulence and flow-fields.

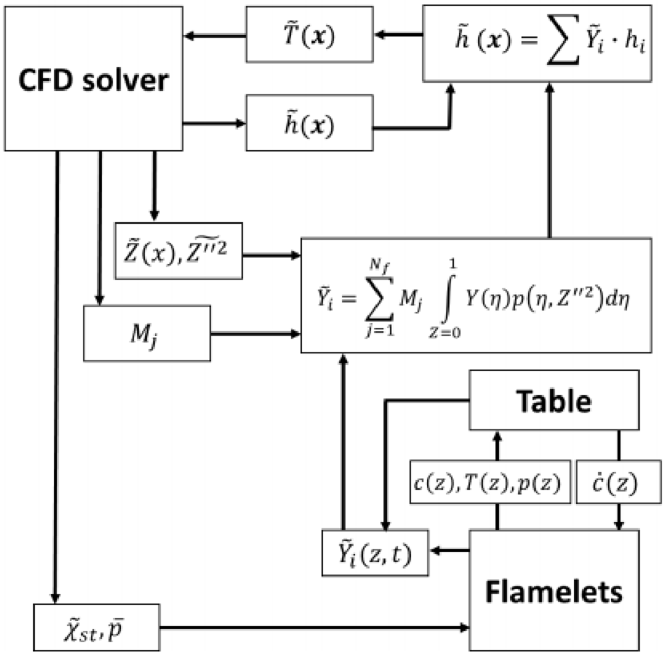

Figure 2.9: Structure of TRIF model

Looking at Fig. 2.9, it is possible to see how the interaction between CFD domain, flamelet domain and chemistry table is realized: at each time step, $\widetilde{\chi_{st}}$ (average stoichiometric scalar dissipation rate) values are passed to each flamelet, that solves equations 2.72 and 2.73. Source term for progress variable equation (eq. 2.72) $\dot{C}$ is computed from the chemistry table and it is function of C and of the local thermodynamic conditions in the mixture fraction space. Also in this model, progress variable reaction rate is set to zero for mixture fraction values corresponding to equivalence ratio $\phi > 3$ (see 2.3). The chemical composition $\widetilde{Y_i}$ in the CFD domain is computed from the mixture fraction Z, its variance and the flamelet marker distribution. Then temperature T is updated from new chemical composition and total enthalpy (whose variation is only due to flow and spray evaporation).

With respect to the tabulation of unsteady flamelets, table sizes of TRIF model are smaller since scalar dissipation rate and mixture fraction segregation are not tabulated.

2.4 Reduction of computational time

Here the adopted techniques to reduce computational effort are reported [50]. A reacting flow, to be entirely solved, must have a certain number of independent variables to be computed, that in general are the mass fractions, enthalpy and pressure. So there are $N_s + 2$ independent variables. However, there are some constraints that must be respected in order to make the solution of the problem feasable. These limitations are:

- $T > 0$
- $p > 0$
- $\sum_{i=1}^{N_s} Y_i = 1$

For this reason, the number of independent variable reduces and decrease to $D = N_s + 2 - n_l$ with n_l that are the linear dependent variables.

The vector that contains all the D independent variables is in function of time and follow the differential equation here reported:

$$\frac{d\overrightarrow{\phi}(t)}{dt} = S[\overrightarrow{\phi}(t)] + \overrightarrow{M}(t) \tag{2.74}$$

The two contributions are related to the chemical reactions (the first) and the flow transported quantities (the second, called also mixing term). Since the characteristic times of the phenomena are radically different, the equation can be split in two parts:

$$\frac{d\overrightarrow{\phi}(t)}{dt} = S[\overrightarrow{\phi}(t)] \tag{2.75}$$

$$\frac{d\overrightarrow{\phi}(t)}{dt} = \overrightarrow{M}(t) \tag{2.76}$$

Eq. 2.76 is solved starting from an initial conditions vector $\overrightarrow{\phi}(t_0)$ of the chemical composition. The solution is defined as ϕ^0 and represent a trajectory in the space of chemical composition. After a time interval Δt, a solution is obtained when the chemical equilibrium is reached. Given the time interval, the solution of eq. 2.75 at a time $t_0 + \Delta t$, denoted as $\overrightarrow{\phi}(t_0 + \Delta t) = R(\phi^0)$ (called reaction mapping), is found integrating the equation and it is only function of ϕ^0. This must be evaluated for each grid node and for every time step. Please notice that this solution is an approximation of the real solution of eq. 2.74, since the characteristic times of the phenomena are radically different.

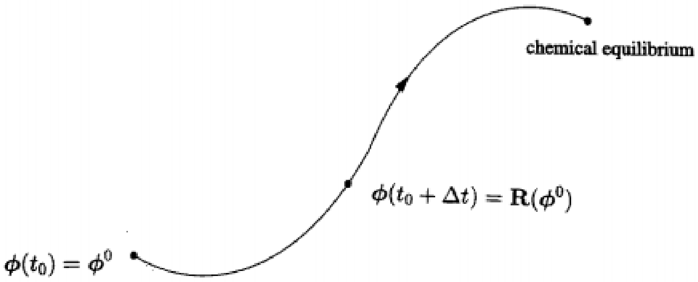

Figure 2.10: Sketch of the reaction trajectory, from [50]

Determining the reaction mapping by means of direct integration is very expensive by a computational point of view since the reaction term requires very short time steps.

The logic of ISAT (in-situ adaptive tabulation) algorithm is that it is possible to save computational time if reaction mappings, that are stored inside specific tables, can be re-used, under particular conditions that will be soon explained. In fact, their computation is time-consuming and often not necessary. Moreover, not all the variables involved in the flow must be solved. Only a limited space, called accessed region, must be stored in these tables. Of course, this depends on the specific case setup and boundary condition at each time step, so a priori it is not possible to know that. For this reason, the table containing all the reaction mappings must be build contemporarily to the simulation (i.e. in situ) and it can be modified at each time step. The reaction mapping concept is used also to define a general query point (i.e. the requirement of solving new thermochemical conditions):

$$\phi^q = \phi^0 + \delta\phi \tag{2.77}$$

$$R(\phi^q) = R(\phi^0) + \delta R \tag{2.78}$$

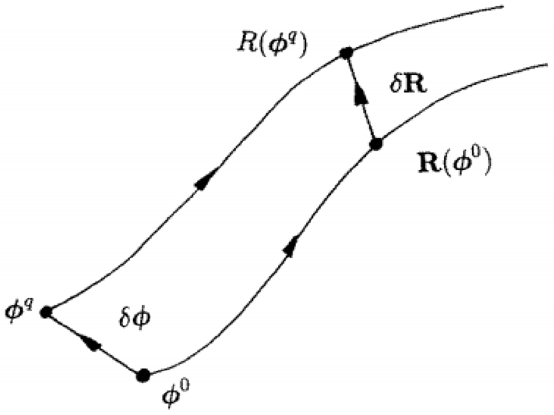

Figure 2.11: Sketch of mapping from tabulation point to query point, taken from [50]

The table stores ϕ^0 and its reaction mapping, but also the mapping gradient matrix defined as:

$$A_{ij}(\phi) = \frac{\partial R_i(\phi)}{\partial \phi_j} \tag{2.79}$$

An approximation can be done for $R(\phi^q) = R^q$:

$$R^{\phi^q} \approx R_l^{\phi^q} = R^{\phi^0} + \delta R_l \tag{2.80}$$

This is a linear approximation, performed using the matrix A and the difference between the starting and the query point vectors. The error related to this can be evaluated as the norm of the difference between the two δR, but only if it is properly scaled by a matrix B for the different components of R (this is done only if required):

$$\varepsilon = |B(\delta R_l - \delta R)| \tag{2.81}$$

If the scaling is applied to the composition, a new vector is obtained defined as $\psi = B\phi$ (if required). The accuracy of this method is defined by means of an accuracy region, that is simply considered to be the space containing ϕ^0 consisting of point ϕ^q for which the error does not exceed a user-chosen tolerance ε_{tol}.

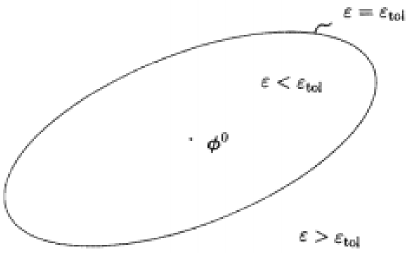

Figure 2.12: Sketch of the ROA, taken from [50]

The ISAT algorithm represents and estimates that region according to 3 rules:

- For each point ϕ^0 the region is approximated by a hyper ellipsoid of accuracy (EOA), defined by two matrices Q and Λ
- An initial conservative estimation of the EOA is done, in order to avoid the generation of unduly large principal axes
- If during the calculation a query point ϕ^q (solution of further reactions) is encountered and it lies within the region of accuracy but outside che estimated one, the EOA is grown, becoming a new hyper ellipsoid of minimum volume enclosing the new point, as it can be viewed clearly in Fig. 2.13.

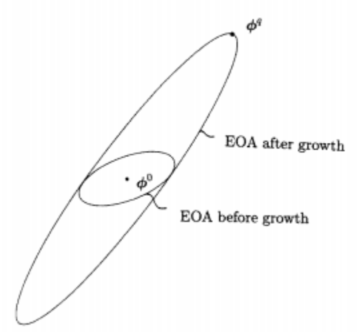

Figure 2.13: Growing process of the ROA, taken from [50]

The ISAT works according to the following box scheme (Fig. 2.14):

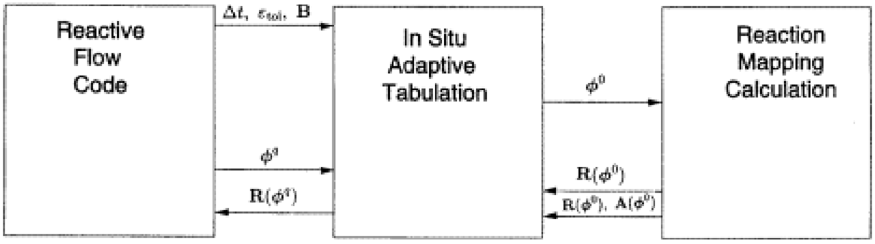

Figure 2.14: Overview of ISAT algorithm, taken from [50]

In practice, for every Δt, a query point is generated, given as input to the reaction mapping calculation that gives the solution $R^{\phi^0}$to ISAT box than again gives back R^{ϕ^q} to the reactive flow code with the required accuracy (it can be both approximated or DI solved).

The table that is generated consists of a binary tree that at each leaf stores a set of records, while for each node it stores a set of cutting plane.

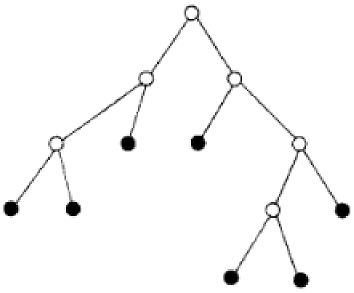

Figure 2.15: Binary tree, taken from [50]: black dots are leafs, white ones are nodes

A record contains:

- tabulation point ϕ^0
- reacting mapping
- mapping gradient (if selected)
- matrices Q and λ, that represents the more updated EOA

The elements of the last point change whenever the EOA grows. After the first query, a record is generated and the reaction mapping is returned, then a serie of steps are followed:

- given a ϕ^q the tree is transversed until a leaf with a ϕ^0 close to ϕ^q is reached
- check if it lies into the EOA

- if the check is ok, the linear approximation is applied and the approximated reaction mapping $R_l^{\phi^q}$ is calculated according to 2.80; the equations involved in this query point are not solved by stiff ODE solvers and time is saved
- if not, direct integration of equation 2.75 is done to calculate R^{ϕ^q} and the error ε is measured
- if the error is within the tolerance, a growth of the EOA is done, according to what is done in Fig. 2.13.
- if the error is outside the tolerance, a new record in the table is done on the query composition that has not satisfied the criteria of the previous steps; the tree will be updated with a new stored leaf and the composition space will be increased using the cutting planes, as seen in Fig. 2.16.

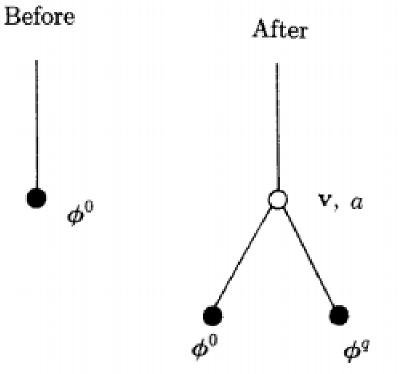

Figure 2.16: Addition of a new query point, taken from [50]

The ISAT approach is more efficient by a computational time point of view than the detailed models, but however it takes more time than the models using reduced schemes, like the DAC, that reduces the species of the kinetic mechanism in function of the thermodynamic conditions. The DAC method dynamically reduces the chemical mechanism is each cell and time-step before every call to the stiff solver according to the directed relation graph (DRG) method, which identifies the relevant species and reactions according to the thermodynamic conditions in each cell [33]. The TDAC chemistry solver model, adopted in the *Lib-ICE* (see 3.1 and Fig. 3.2) of Politecnico di Milano ICEG research group, offers a good compromise between accuracy of results and further reduction in computational time, combining DAC, ISAT and stiff ODE solver. As it can be understood from Fig. 2.17, it is an update of the ISAT algorithm:

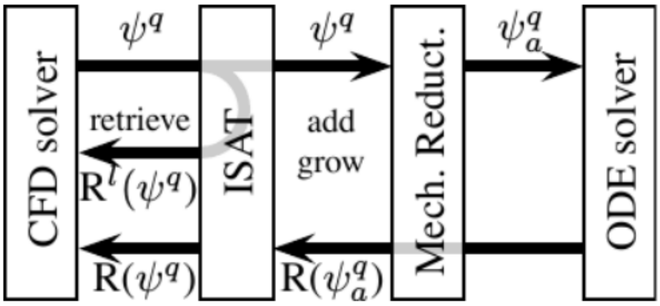

Figure 2.17: TDAC algorithm [32]

Before entering the ODE solver, a sort of double-filtering of the query point is done.

The concept behind the mechanism of reduction is that a minimum number of all the species that are carried on by the chemistry solver are useful to well describe the combustion process. So many species and reactions are cut off from the detailed mechanism. Looking at Fig. 2.17, it is clear that most of the element of the vector ϕ^q entering in the mechanism reduction box does not enter in the ODE system solver, so a huge computational time is saved. The output mapping coming out from the ODE solver box is then returned as an input in the ISAT box to add or grow the binary tree an to build the whole reaction mapping R^{ϕ^q} that is required to compose the full chemical composition in space.

The use of TDAC ensures speed-up factors ranging from 10 to 1000 depending on the mechanism size and simulated combustion mode [33].

2.5 Soot modeling

The main difficulties in modeling the soot generation and destruction processes are related to the very big number of complex chemical and physical phenomena that are involved and still, at least partially, not understood completely. Very different results are obtained if a model is applied with respect to another one, but also significant mismatching are present if some chemical reactions, for instance, are included in the model or not. As every fluid-dynamic problem, increasing the level of detail of the adopted model causes a relevant rising of the computational time. Moreover, coupling a given soot model with a complex turbulence one, can be practically unfeasible. Basically, Kennedy [29] suggested that there are 3 main categories: empirical, semi-empirical and detailed models.

2.5.1 Classification of soot models

Empirical models relies entirely on the experimental evidences, so they are linked to very specific setups and cannot be adopted to describe a general combustion case, but only to cases with initial and boundary conditions similar to the starting one. They are useful to calculate the soot tendency of the fuel by means of an index called TSI, that is calculated empirically. Empirical studies are also carried on to analyze the TSI dependency over the C/O atoms ratio. *Semi-empirical* models were implemented to try to not consider soot as something that is generated suddenly, but to describe in a more or less detailed way those phenomena that contribute to the generation of soot particles (inception, nucleation etc..). Each of these steps is generally described by a single reaction. Of course, in such a complex field, a key role is played by the description of the chemical reactions happening inside the combustion region and its coupling with soot kinetics. The very first semi-empirical model that has been developed was the Tesner and co-workers [56], that was simply based on two soot reactions: formation and destruction (oxidation). Although it seems a too simplified approach, simple methods based on the same concepts, as the Hiroyasu at al. model [16], are currently used for some applications, paying attention to calibrate well the case. Two equations soot models are very used and they are mainly based on the transport equations for soot mass and density. In practice, this is a reduced momentum methods where the first two moments of particle size distribution (PSD) are solved [34]. The PSD variance is considered null (spherical and mono-dispersed particles), however it is possible to insert a third equation in this model to relax this assumption, considering that, as proposed by [51], particles size follow a log-normal shape. Other relevant semi-empirical models are the Moss et al. [38] and the Leung et al. [30]. In this work, the adopted model is the latter, so it will not be spent time in the description of the Moss model. In the next Section instead a detailed description of Leung soot model will be provided. The last category is the *detailed* models. They attempt to describe the detailed elementary chemistry reactions and the physics of soot formation (with all its sub-steps), in gas phase, solid phase and interface between them. The first detailed model was developed by Frencklach and co workers [37]. The big advantage that derived from it was the possibility of predicting the soot particle size distributions in the domain, that in general affect the optical properties of the soot cloud and the radiative heat loss. More complex models have been derived from it. The great majority of the detailed models are included in the categories of the discrete-sectional methods, where an aerosol distribution is divided into finite size groups representing a sub-group of particles, and the method of moments (MOM). The latter is slightly more efficient by a computational point of view and it is based on a statistical approach in dealing with the particle dynamics. The peculiarity of this method is that instead of describing the complex chemistry involving hundreds of reaction to describe soot formation, soot particles can be seen as ensembles of single carbon atoms of different sizes. The distributions of particle sizes are function of particles that collide to each other to form PAHs [49]. In this way, particle dynamics fully describes the evolution in time of these ensemble during the undergoing soot formation sub-processes. This purely mathematical approach was followed by MOMIC, an implementation based on numerical interpolation that allowed to solve some numerical issues present in MOM. The weak point was that they can be used only for mono-dimensional flames. However, the addition of the flamelet theory, allowed to get new methods, like the discrete-sectional one, that is a sort of fully detailed model for multidimensional laminar co-flow flame [53]. The very high computational costs of these methods is often not justified by better results, since reliable ones are obtained also using semi-empirical models [49].

2.5.2 Leung Lindstedt Jones model

As already said before, this is the model that is used in the numerical calculation of this thesis. The model has two transport equations: one solves the soot molar density cN_p (that is the ratio between the particle number density n_{soot} and the number of Avogadro, and it is expressed in $[kmol_{soot}/m^3_{mixture}]$) while the other one solves the soot mass density $\rho_s f_v$ (where ρ_s is the soot density, equal to 2000 $[kg_{soot}/m^3_{soot}]$, and f_v is called soot volume fraction, expressing the volume occupied by soot per unit volume of mixture $[m^3_{soot}/m^3_{mixture}]$). So, soot mass density is the mass of soot per unit volume $[kg_{soot}/m^3_{mixture}]$. Particles are assumed to be spherical with a mono-disperse size distribution, so:

$$f_v = \frac{\pi d_p^3}{6} \cdot n_{soot} \tag{2.82}$$

The first thing to say about this model is that the i^{th} process (nucleation, surface growth, oxidation, agglomeration) involved in the soot formation is described by simple, modified version of the Arrhenius equation:

$$k_i = A_i T^{B_i} \exp\left(\frac{-E_i}{RT}\right) \tag{2.83}$$

An important assumption of the model derives from an experimental evidence, according to which the higher the products that are formed due to the pyrolysis phenomena, in particular acetylene that is the most abundant, the higher the soot amount. That is why it is selected as soot precursor, keeping in mind, as suggested by Leung [30], that this assumption is valid only in the location where nuclei are generated. The dissociation of acetylene, derived the breakdown of the fuel, corresponds to the nucleation step and follows the formula:

$$C_2H_2 \rightarrow 2C(s) + H_2 \tag{2.84}$$

The $C(s)$ notation, due to a non negligible amount of hydrogen, is not completely correct, but the absence of a valid alternative theory make it still widely accepted.

The problems related to the determination of the reaction rates and the temperatures of activation ($\frac{E_i}{R} = T_a$) of each sub-process are the central part of this theses. For now, only the assumptions made by Leung are reported. First, it must be said that the nuclei generated in this phase are considered to have a minimum carbon atoms and a minimum diameter. For what concerns the atoms, this number is 100, but there are many works [34] that actually uses 60. Instead, the minimum diameter is 1.24 nm. However, no significant changes in the results are obtained choosing different numbers. There are many T_a possible values, as for example the one proposed by Gilyazefdinov [31] that used 49000 K. However the most commonly used when Leung wrote the article was 21100 K, value that is also close to the overall activation energy suggested by Vandsburger et al [57]. The reaction rate can be finally written as:

$$R_1 = k_1(T)[C_2H_2] \tag{2.85}$$

$$k_1(T) = 0.1 \cdot 10^5 e^{-21000/T} \tag{2.86}$$

Here, it is expressed as $[kmol_{soot}/m^3_{mix}/s]$, but it can be easily converted into $[Kg]$ by multiplying by the soot molar mass, i.e. carbon one. It is clear that it contributes to the overall soot mass increasing $\rho_s f_v$. The pre-exponential term was determined starting from the experimental analysis of a flame burning ethylene (C_2H_4) at ambient conditions. It is clear so that this could not fit well the characteristics of flames burning with another fuel in other thermodynamical conditions. The soot nucleation step contributes also to the number density cN_p, adding a source term. A proper explanation will be provided soon.

The following step is the surface growth that, as proposed by Harris and Weiner [26], is function of the acetylene concentration:

$$C_2H_2 + nC(s) \rightarrow (n+2)C(s) + H_2 \tag{2.87}$$

$$R_2 = k_2(T)[C_2H_2]\sqrt{\pi\left(\frac{6M_s}{\pi\rho_s}\right)^{\frac{2}{3}}} \cdot [C(s)]^{\frac{1}{3}}[\rho N]^{\frac{1}{6}} \tag{2.88}$$

where Y_s is the soot mass fraction, M_s is soot molar mass, $[C(s)]{=}\rho\frac{Y_s}{M_s}$, N is number of particles per kg-mixture. Again, it is expressed as $[kmol_{soot}/m^3_{mix}/s]$. The whole expression that is multiplied by $k_2(T)[C_2H_2]$ is called $f(S)$ and it is used to keep into account the phenomena of the surface ageing already described in Section 1.2.3. This is useful to express the complex dependency of the surface growth with the active surface S. It is proportional to the square root of the surface. For what concerns the constant, the activation temperature equal to 12100 K has been defined after a big number of computations, while the pre-exponential term of $0.6 \cdot 10^4$ has been calculated by means of the a semi-empirical approach very similar to the one used for nucleation. The surface growth only contributes to the increasing of the total mass, so no variation of soot particle number happens. The weakest part of the original Leung model is the oxidation treatment. The assumption that is done is to consider null the OH oxidation, while it is well known that this specie plays a key role in soot destruction, as said in Section 1.2.5. The undergoing reactions that govern oxidation processes are:

$$C(s) + \frac{1}{2}O_2 \rightarrow CO \tag{2.89}$$

$$C(s) + OH \rightarrow CO + H \tag{2.90}$$

However, the structure of the formula describing this phenomena in practice is the same of the processes already seen. An important addition, that helps to consider also the fundamental OH oxidation, was suggested in the works of Kronenburg [17] and Bolla [34] and it has been added to complete the Leung model:

$$R_3 = k_3(T)S[O_2] + k_6(T)\Gamma_{OH}S[OH] \tag{2.91}$$

$$k_3(T) = 0.1 \cdot 10^5 T^{\frac{1}{2}} e^{-\frac{19600}{T}} \tag{2.92}$$

$$k_6(T) = 9 \cdot T^{\frac{1}{2}} \tag{2.93}$$

Γ_{OH} is called collisional effect and it is equal to 0.04. Again, it contributes only to the mass variation. The original constants, while used only for the O_2 oxidation formula, significantly underestimate the oxidation rate [42]. That's why it was immediately recognized that OH played a key role in this process. Finally, to close entirely the system of soot mass formation/destruction and particles number density ($\rho_s f_v$ and cN_p), a final reaction is added, keeping into account the reduction of the density. This corresponds to the particle agglomeration:

$$nC(s) \rightarrow C_n(s) \tag{2.94}$$

$$R_4^{agg} = -2C_a d_p^{\frac{1}{2}} \left(\frac{6\kappa T}{\rho_s}\right) (cN_p N_A)^2 \tag{2.95}$$

This formula contains inside the $k_4(T)$ term. For the full formulation, see [30].

Therefore, a complete source term can be written considering the overall density increasing, related the joint effect on cN_p of nucleation and agglomeration:

$$R_4 = R_4^{nuc} + R_4^{agg} = \frac{2}{C_{min}} N_A R_1 - 2C_a d_p^{\frac{1}{2}} \left(\frac{6\kappa T}{\rho_s} \right) \left(cN_p N_A \right)^2 \tag{2.96}$$

where N_A is the Avogadro's number, C_{min} is the minimun number of carbon atoms of a particle, k is the Boltzmann constant, ρ_s is soot density and C_a is the agglomeration rate constant, assigned as 9, higher than the one used in other works [20].

Finally, it is possible to build the two equations of the model:

$$\frac{\partial cN_p}{\partial t} - \frac{\chi}{2} \frac{\partial^2 cN_p}{\partial Z^2} + \frac{1}{2} \frac{\partial \chi}{\partial Z} \frac{\partial cN_p}{\partial Z} = R_4 \tag{2.97}$$

$$\frac{\partial \rho_s f_v}{\partial t} - \frac{\chi}{2} \frac{\partial^2 \rho_s f_v}{\partial Z^2} + \frac{1}{2} \frac{\partial \chi}{\partial Z} \frac{\partial \rho_s f_v}{\partial Z} = M_s \left(R_1 + R_2 - R_3 \right) \tag{2.98}$$

In RIF and TRIF models they are solved in flamelet domain, just as a simple chemical species. Then the distribution in the CFD domain is obtained using, as decribed in Section 2.2.2.2, a β-PDF. However it must be underlined that source terms related to soot formation and oxidation are not included in the kinetic gas-phase mechanism: they are obtained using values of temperatures and species concentrations calculated in the considered time-step, so they do not contribute to the consumption of chemical species involved in soot creation and destruction processes. Anyway, some works [39, 45] have demonstrated that this way to proceed gives good results.

Chapter 3

Simulations Setup

In this chapter the used solvers and the setup of the simulations will be presented. All the simulations in this work are performed using *OpenFOAM* (Fig. 3.1) and in particular the applications and libraries contained in the *Lib-ICE*, entirely developed by the *ICEGroup* (Internal Combustion Engines Group, [8]) of Politecnico di Milano.

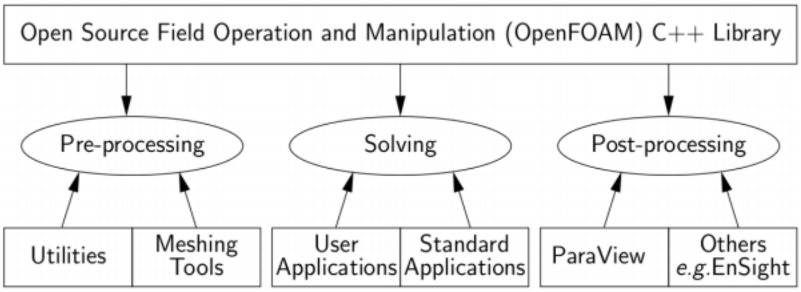

Figure 3.1: *OpenFOAM* structure

3.1 *Lib-ICE*

In Fig. 3.2 the tree structure of the *Lib-ICE* folders is reported.

Folder *src* contains the libraries implemented in the *Lib-ICE* (lagrangian spray model, chemical solvers, pollutant models) that are used by the solvers, contained in the folder *applications*. Inside the latter there is another one called *utilities*, inside which there are pre-processing and post-processing tools.

In *applications/utilities/preProcessing* there are *setTabulatedFlameletFields* and *setFlameletFieldsRegion*, used respectively for the flamelet initialization for the tabulated solvers (TRIF and TWM) and for the RIF.

Instead in *applications/utilities/postProcessing* there are *getTabulatedFlameletsData* and *getFlameletsData*, that collect (among the others) the soot mass as function of time again respectively for the tabulated solvers and the RIF.

Flamelet Combustion Library (*src/flameletCombustionLibrary*) contains the func-

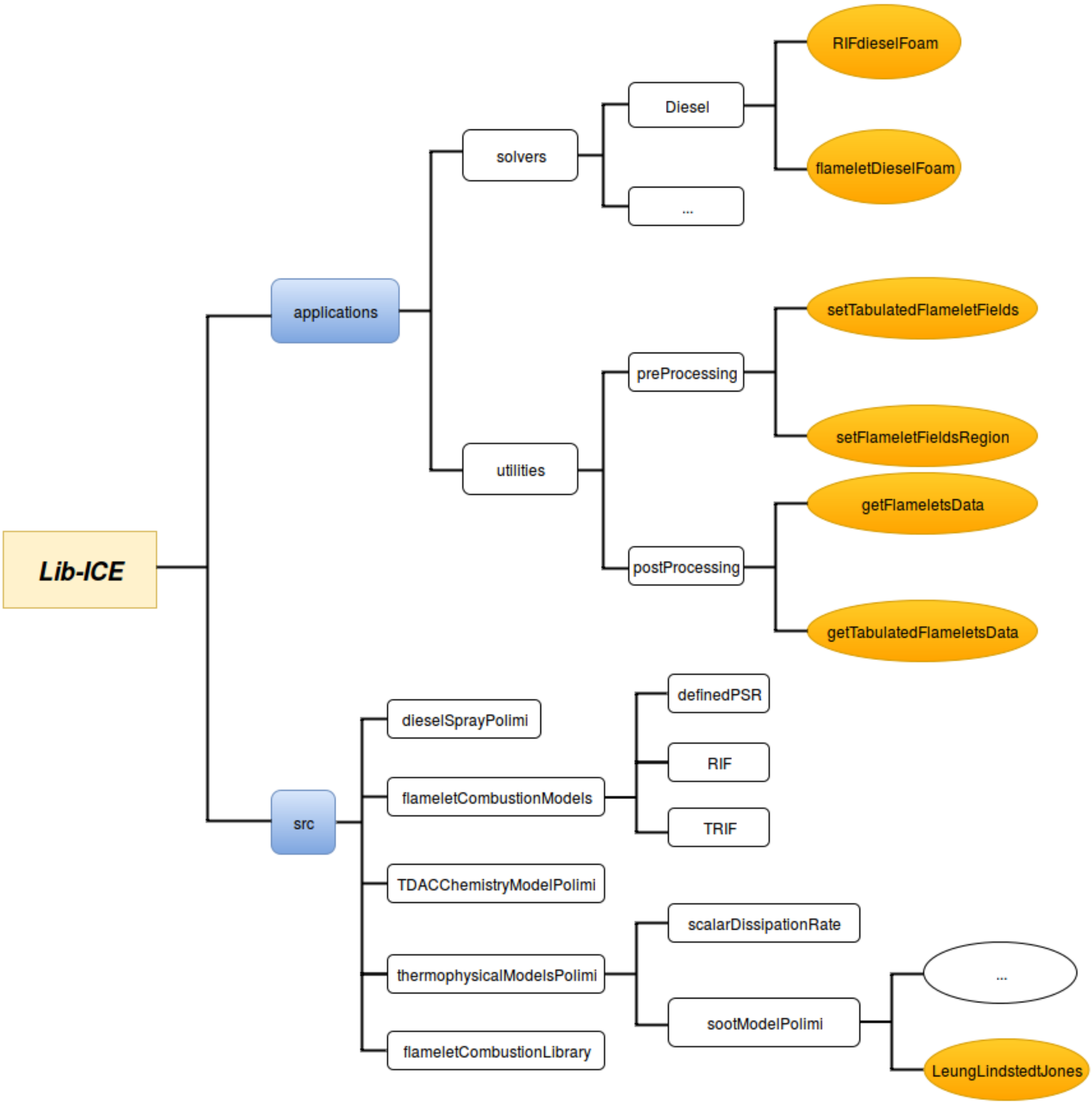

Figure 3.2: *Lib-ICE* structure

tions that couples the generation of the table with the CFD resolution: in particular it calculates the source term for the progress variable $\dot{c}$ (see eq. 2.63).

The adopted solvers are *RIFDieselFoam* (for RIF and TRIF model) and *flameletDieselFoam* (for TWM model), already implemented in the *Lib-ICE*.

3.2 Structure of OpenFOAM case

The typical structure of an *OpenFOAM* case is the one depicted in Fig. 3.3: in *0* folder all the initial and boundary conditions are contained, in *constant* there are all the properties of the case that do not change in time, while in *system* the timing of the simulation, the discretization schemes and the solvers for all the equations are set.

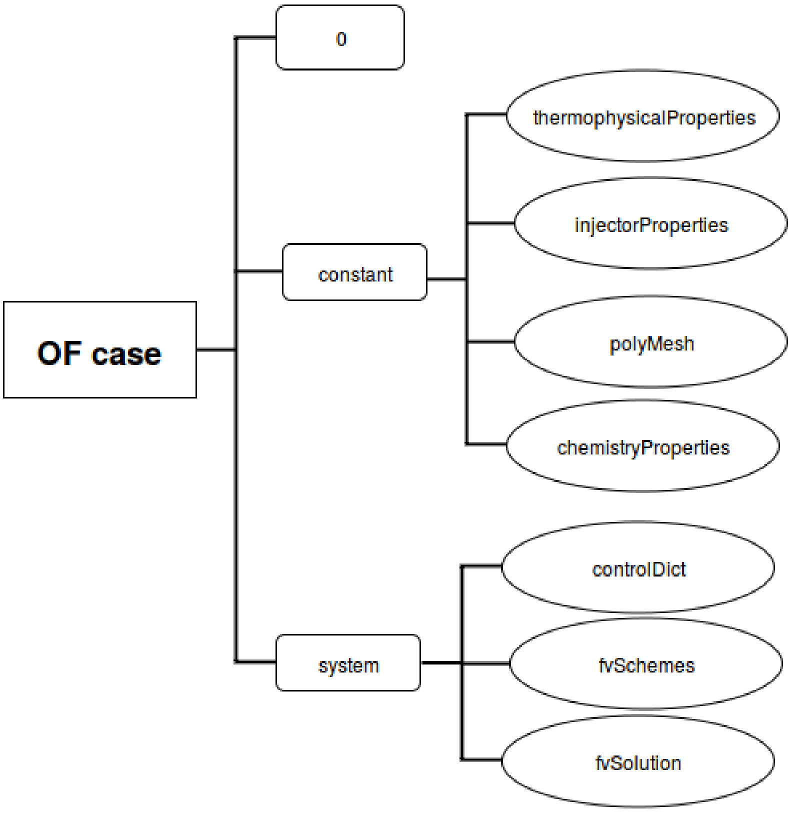

Figure 3.3: *OpenFOAM* case structure.

3.3 Simulations setup

3.3.1 Mesh

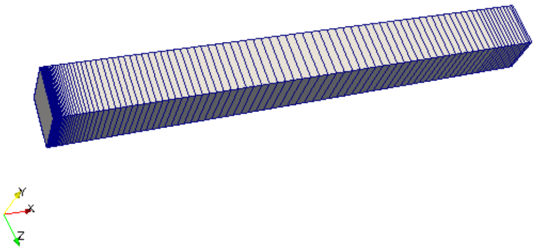

Figure 3.4: Chemical domain

Due to the axisymmetric nature of the real problem (see Chapter 4), the bomb (i.e. the CFD domain) has been discretized using a wedge of 5° with sides of 108 mm and 60.93 mm (Fig. 3.5), resulting in a volume of 1.75071 cm^3 using 26784 hexahedral cells (with particular refinement close to the axis and close to the nozzle). Considering the 360° geometry, the overall volume is equal to 0.000126051 m^3 (practically the same of the experimental setup, see Section 4.2).

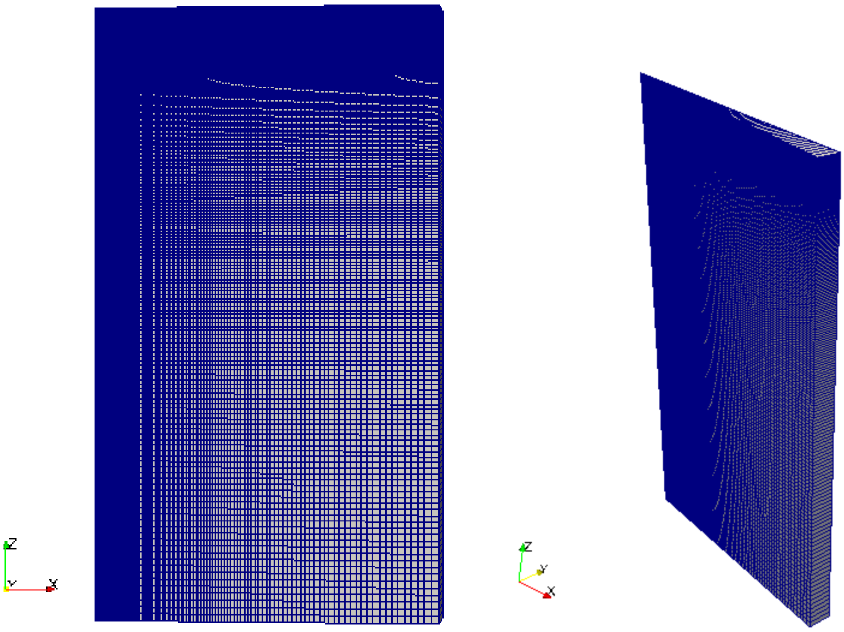

Figure 3.5: CFD domain

For what concerns the chemical domain (Fig. 3.4), it has been discretized using a monodimensional parallelepiped (please notice that in this domain gradients along y and z directions are neglected, as already said in Section 2.2): the x axis corresponds to the Z coordinate, and its boundaries represent the oxidizer side ($x = 0$) and the fuel side ($x = 1$). A refinement is done at the boundaries because required by the β-PDF integration (due to the fact that β-PDF (Fig. 2.4) has a steep behaviour close to oxidizer and fuel sides, so a refinement is required to discretize it correctly).

3.3.2 Spray modeling

Spray evolution is described by the Lagrangian solver implemented in the *LibICE* (*src/dieselSprayPolimi*). The gas-phase of the spray is described using RANS equations, while liquid spray is assumed to be made up by a discrete number of parcels, and each one is composed by an ensamble of droplets with the same physical properties. These two phases are coupled since there is an exchange of momentum, energy and mass. In order to define the starting conditions of the first drops at nozzle exit, blob-injection model is used: the main idea is that when the fuel is injected inside the combustion chamber, it can be seen as a big spherical droplet with a size equal to the nozzle diameter; the number of drops injected per unit time depends on the mass flow rate. Both the primary and the secondary break-up are described using the KH-RT model, a combination of the Kelvin-Helmholtz model and the Rayleigh-Taylor model (Fig. 3.6). For further informations, see [12, 25, 48].

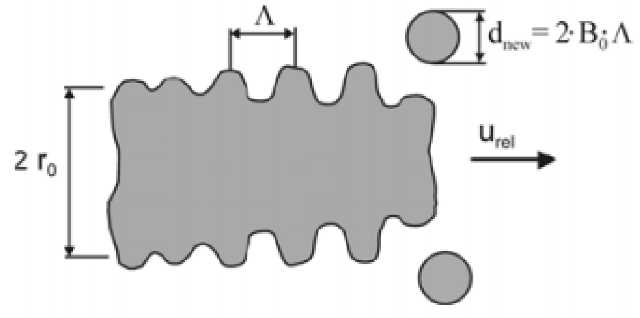

(a) Kelvin-Helmoltz (KH) model

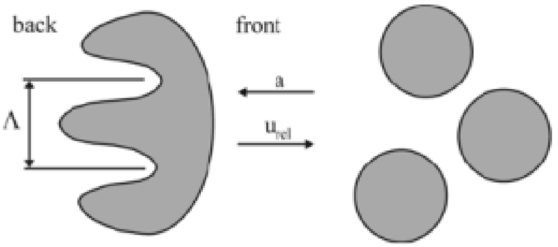

(b) Rayleigh-Taylor (RT) model

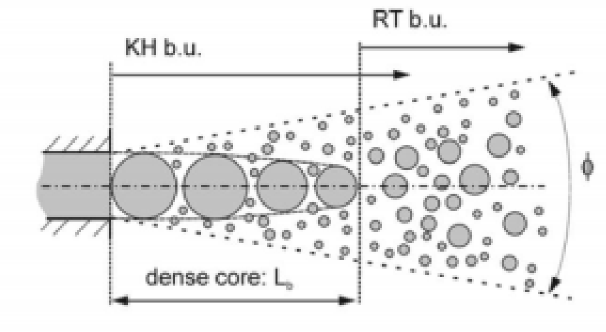

(c) KHRT model

Figure 3.6: Spray break-up models

3.3.3 Injection law

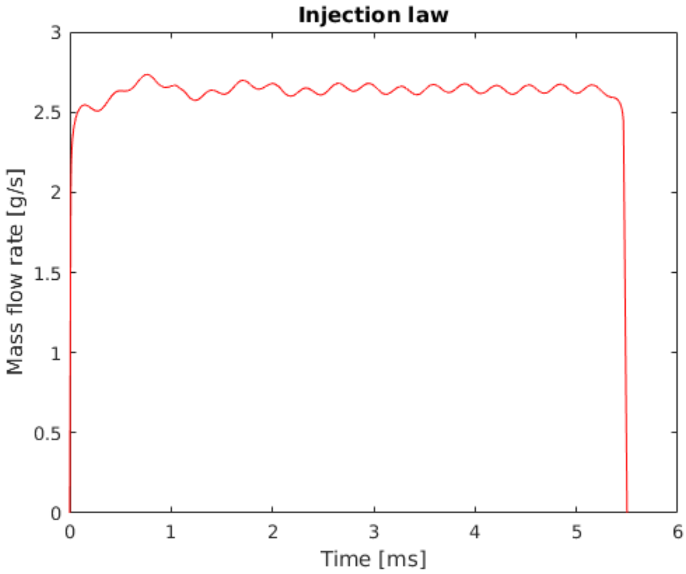

Figure 3.7: Injection law

The injection law has been generated using the utility available at [7]. An injection duration of 5.5 ms has been chosen (Fig. 3.7), and the injected total mass has been calculated numerically integrating the mass flow rate over the time, and it is equal to $1.441389688 \cdot 10^{-5}\ Kg$. The new injection law has been updated in *OFcase/constant/injectorProperties*.

3.3.4 Kinetic mechanism

As said in previous sections, the real number of chemical reactions and chemical species involved in a combustion process is huge. For instance, a detailed model is the *POLIMI_TOT_1407* [1] that contains more than 450 species and around 15000 reactions. Of course, it is practically impossible to deal with such a huge quantity of reactions, also considering that a vast majority of them do not take place during combustion. For this reason, lumped and reduced mechanism are used, obtained starting from *POLIMI_TOT_1407*. Among the various possibilities, the best compromise in terms of time saving and level of precision was to choose the extended *Faravelli sketal mechanism* with 133 species, which is a more detailed mechanism with respect to the simple reduced mechanism containing 96 species, validated by the works of Stagni [54] and Ranzi [47]. The latter has been used by other authors working with the *ICEGroup* and in particular it has been shown in [15] that the reactivity is not significately influenced by the additional 37 species. However the main advantage of using this extended mechanism is related to the necessity of well representing the soot formation, that is directly related to the PAHs presence [15]. From this point of view, the formation of species as cyclopentadiene, methyl-cyclopentediene, benzene, toluene, phenylacetylene, indene and naphthalene is very important to simulate. Here a resuming table is reported:

	Species	*Reactions*
POLIMI_ TOT_ 1407	>450	>15000
Faravelli	96	993
Extended Faravelli	133	2275

Table 3.1: Number of species and reactions of each mechanism

3.3.5 Soot constants

In *src/thermophysicalModelsPolimi/sootModelPolimi/LeungLindstedtJones* the soot model described in Section 2.5.2 is implemented. The equations for all soot generation and destruction processes are in the form of the typical Arrhenius expression (eq. 2.83), with a pre-exponential term and an exponential one. The constants nomenclature is slightly different with respect to the one employed by Leung, but the concepts are the same:

- *aAlpha*: pre-exponential term for nucleation $[{}^{1}/_{s}]$
- *TaAlpha*: exponential term for nucleation $[K]$
- *bBeta*: pre-exponential term for surface growth $\left[{}^{m^{\frac{1}{2}}}/_{s}\right]$
- *TaBeta*: exponential term for surface growth $[K]$
- *Cbeta*: pre-exponential term for coagulation $[-]$
- *Coxi*: pre-exponential term for both OH and O_2 oxidation $[-]$
- *cOmegaOH*: pre-exponential term for OH oxidation $\left[{}^{Kg\cdot m}/_{s\cdot K^{\frac{1}{2}}\cdot Kmol}\right]$
- *cOmegaO2*: pre-exponential term for O_2 oxidation $[{}^{m}/_{s}]$
- *TaOx*: exponential term for O_2 oxidation $[K]$
- *Cmin*: minimum number of carbon atoms required to generate a soot particle $[-]$
- *Schmidt soot number* $[-]$: is a dimensionless number defined as the ratio of momentum diffusivity and mass diffusivity. In this case, it measures the ratio between the diffusion of soot particles in axial direction due to their momentum (since fuel injection is axial too) and the mass diffusion, that of course happens also in radial direction. The bigger the soot particle diameter, the higher the *Schmidt soot number* because the higher the momentum (and so the axial diffusion).

During the calibration of the model, in *OFcase/constant/thermophysicalProperties* all the previous default constants, already implemented in the model, can be overwritten. In addition, it is possible to select also the precursor and the soot oxidation model.

3.3.6 Discretization methods and solvers

The equations presented in Section 2.1.1 must be discretized in order to be solved. Since the effects of the discretization schemes and of the solvers on the results is not the aim of this work and they have been already validated by past works [35] [36], they are simply reported in Tab. 3.2. Except for Euler scheme, they are all second order schemes, so accuracy is guaranteed.

	RIF	TWM	TRIF
$\frac{\partial}{\partial t}$	Euler	Euler	Euler
$\nabla\varphi$	Gauss linear	Gauss linear	Gauss linear
$\nabla\cdot\varphi$	Gauss limited linear 1	Gauss limited linear	Gauss linearUpwind
$\nabla^2\varphi$	Gauss linear corrected	Gauss linear corrected	Gauss linear limited 0.5

Table 3.2: Discretization schemes.

For what concerns the solvers, in RIF and TRIF iterative solvers based on the conjugate-gradient are used: PCG (*Preconditioned conjugate gradient*) is used to solve pressure equation and PBiGC (*Preconditioned bi-conjugate gradient*) is used to solve the others. In order to increase the rate of convergence and avoid ill-conditioning problems, DIC (*Diagonal incomplete Choleski*) and DILU (*Diagonal incomplete-LU*) preconditioners are applied respectively to PCG and PBiGC. For TWM instead GaussSiedel solver is used.

In *OFcase/system/controlDict* it is possible to impose some simulation parameters: the *endTime* of the simulation has been set equal to 8 ms in order to simulate flame extinction, while the time step duration (kept constant during the simulation) is equal to $2.5 \cdot 10^{-7}s$. The maximum Courant number is set equal to 0.25, in order to improve stability.

3.3.7 Optical window

Soot mass data are collected using an optical window, which dimensions are specified in *OFcase/constant/chemistryProperties* in order to reproduce the Sandia measurement setup (see next Chapter). The dimensions of the window are (with respect to the CFD domain reference system):

xWinMin	xWinMax	yWinMin	yWinMax	zWinMin	zWinMax
0	0.054	-100	100	0.04	0.108

Table 3.3: Optical window data, in [mm].

Chapter 4

Sandia Experimental Setup

The validation of the adopted combustion models and the calibration of the soot model are done comparing the numerical results with the experimental data provided by the engine combustion network ECN, an organization that carries on experiments regarding combustion. There is a huge amount of data made available on their website. In particular, this thesis is focused on the analysis of the results obtained with the so called Spray-A campaign, which is a Diesel (non-premixed) experimental one.

4.1 Spray-A

The fuel that are adopted by Sandia are surrogates of real diesel fuel, which means that they behave in a very similar way with respect to commercial fuels. In this case, normal dodecane *n-dodecane* ($C_{12}H_{26}$) is used:

Chemical formula	$C_{12}H_{26}$
Density (at 25°C)	$752.1\ {}^{Kg}/_{m^3}$
Molar mass	$170,34\ {}^{g}/_{mol}$
Autoignition temperature	$476,15\ K$

Table 4.1: *n-dodecane* properties

The injector is a common rail Bosch solenoid-activated of generation 2.4. In Tab. 4.2 its main characteristics are reported.

The spray is injected inside a proper vessel (see next section 4.2).

4.2 Constant Volume Bomb

The experiments are carried in a combustion vessel, called bomb, with a constant volume (Fig. 4.1).

Fuel injector nominal nozzle outlet diameter	$0,090\ mm$
Nozzle K factor	$K = 1.5$
Mini-sac volume	$0.2\ mm^3$
Discharge coefficient at 10 MPa pressure drop	$C_d = 0.86$ (at T_{amb} using diesel fuel)
Number of holes	1
Orifice orientation	axial
Injection pressure	150 Mpa
Injector serial number	210370
Nominal fuel temperature	363K

Table 4.2: Injector and nozzle specifications

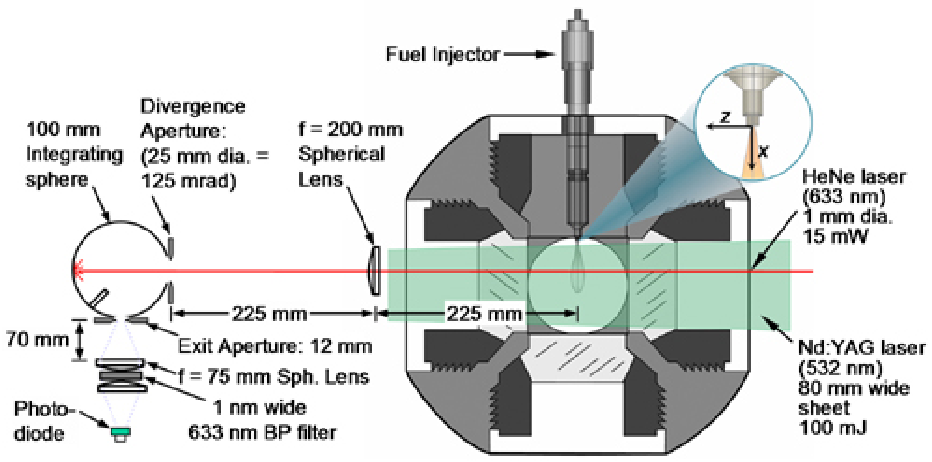

Figure 4.1: Sandia constant volume bomb

All the informations provided are taken from the Sandia ECN website [4]. The bomb is a cube with a side of 0.108 m (and so with a volume of 0.001259712 m^3) and it is equipped with sapphire optical openings that are used to perform some optical measurements. Soot is also measured by means of these special openings. In particular, the techniques of laser extinction and planar incandescence (PLII) are used to measure quantitatively the amount of soot generated. For laser extinction, a modulated (50 kHz) 15-mW, 1-mm diameter HeNe laser beam (wavelength 632.8 nm) passes through the sooting region of the flame and it is collected by an integrating sphere, narrow band pass filter and photodiode. The trasmitted intensities are related to the soot optical thickness KL:

$$\frac{I}{I_0} = exp(-KL) \tag{4.1}$$

where K is extinction coefficient, L is the path length trought the soot and I and I_0 are trasmitted laser intensities with and without soot presence. KL can be quantitatively related to the soot volume fraction f_v by means of the formula provided by small particle Mie theory [52] (Fig. 4.3):

$$f_v = \frac{K\lambda}{k_e} \tag{4.2}$$

Note that this relation is affected by uncertainties in soot optical properties. Instead, PLII images are obtained by passing a thin (0.3 mm) Nd:YaG laser sheet (532 nm) through the fuel jet centerline, as shown in picture. The PLII signal was imaged with an intensified CCD camera (50 ns gate). The lens and the filter used were a Nikkor 105 nm, f/2.8 lens, a 450 nm short-pass filter and a zero-incidence 532 nm laser mirror. It must be undelined that laser extinction measurements are time-averaged over the quasi-steady, mixing-controlled phase of the combustion event (Fig. 4.2).

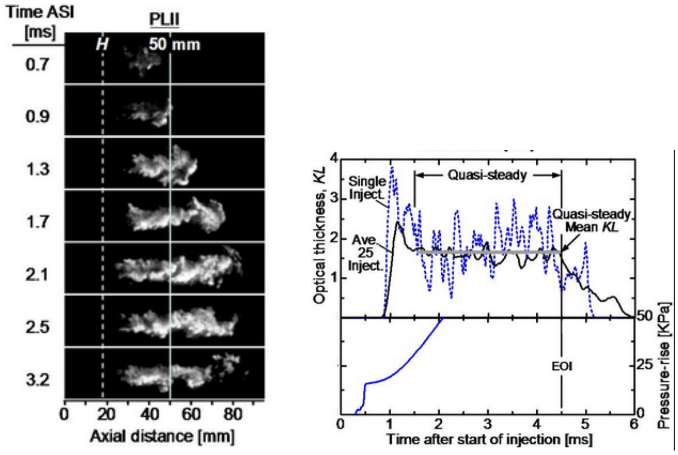

Figure 4.2: KL averaging

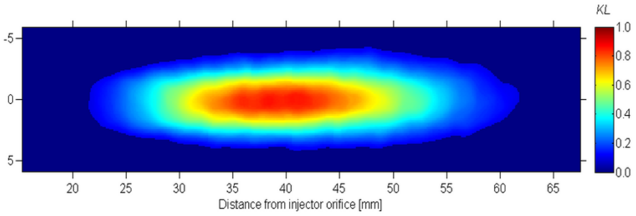

(a) KL

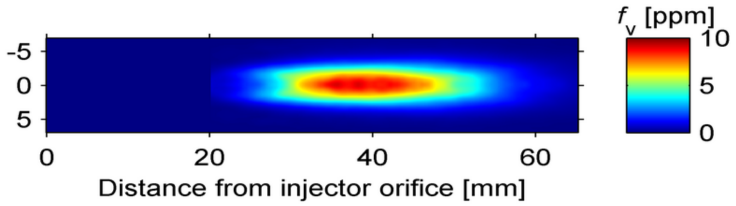

(b) f_v

Figure 4.3: Example of optical thickness KL and the related soot volume fraction f_v

4.3 Nominal ambient conditions

Different flames, obtained with different ambient conditions, were studied. Several oxygen and temperature conditions are available from Sandia, but this work is focused on the study of sweeps of temperature and oxygen, in order to reproduce different possible diesel engine conditions (e.g. exhaust gas recirculation *EGR*) using n-dodecane. So the considered initial conditions are the ones in Table 4.3:

T [K]	p [MPa]	O_2 [%]	N_2 [%]	CO_2 [%]	H_2O [%]	Amb. air ρ [$^{Kg}/_{m^3}$]
850	5.63	15	75.15	6.22	3.62	22.8
900	6.04	13	77.09	6.26	3.64	22.8
900	5.98	15	75.15	6.22	3.62	22.8
900	5.91	21	69.33	6.11	3.56	22.8
1000	6.62	15	75.15	6.26	3.64	22.8

Table 4.3: Nominal ambient initial conditions (species expressed in mole fractions)

Please notice that in Chapter 5 and 6 the different initial conditions are recalled and indicated considering temperature and oxygen values. For instance, the third condition reported in Tab. 4.3 is called 900 K 15% O_2.

4.4 Lift-off length and ignition delay

The quasi-steady lift-off length, that is the distance from the injector at which the flame stabilizes, can be measured through chemiluminesce from excited-state OH [27]. Time-averaged, line-of-sight images of light emitted from a burning fuel jet at 310 nm were acquired with an intensified CCD camera using a 310 nm band-pass filter (10 nm FWHM) (Fig. 4.4). This is possible since OH is the major source of light emission at 310 nm. Altough also soot lumonosity is significant in this case, but OH chemiluminescene dominates in lift-off region. Unlike ground state OH (that is an equilibrium product), the OH analyzed in this experimental setup is related to chemical reactions in near-stoichiometric, high-heat release regions.

As it is shown in picture 4.4, OH chemiluminescence starts to be clearly visible at a very well defined distance from the injector. The standard to identify the exact location of lift-off length says that the flame starts where the light intensity is 50% greater than the levelling-off value, after a proper averaging procedure between the luminosity values up and down to the center line. High speed movies of chemilumiescence shows that this distance quickly stabilizes after autoignition and remain stationary. Ignition delay can be evaluated in two different ways: chemiluminescene and pressure based method. The first is based on the high-temperature chemiluminescence, by means of a light based method that is required since some devices are open-system at constant pressure. Moreover, the second method requires speed of sound correction to the transducer. When chemiluminescene is studied, the most difficult part is to understand if the luminosity comes from the flame itself (whose timing is the one that determines the ignition delay) or from soot/cool-flame luminosity. The difference lies on the fact that the light we are interested on is at least an order of magnitude more intense than the other. The ignition delay is established at a time that is an average between the cool-flame chemiluminescence detection time and the high-T flame one. The second method instead refers to the measurement of the pressure rise curve by means of a pressure transducer placed inside the vessel, paying attention to the delay in the pressure measurement caused by the speed of sound and the distance between the ignition site and the pressure transducer [27]. A further correction is done to consider the heat transfer phenomena inside the vessel during the injection.

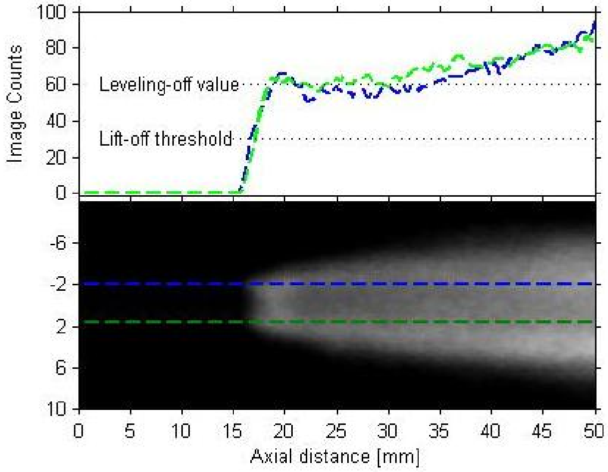

Figure 4.4: Example image of time-averaged OH chemiluminescence [2]

Chapter 5

Validation Of Combustion Models

In this chapter the validation of the 3 combustion models (RIF, TWM and TRIF) presented in Chapter 2 and 3 is reported. The tested conditions are the ones shown in Chapter 4.

In order to validate them, it is important that all the combustion phases (Chapter 1) of a Diesel flame are well caught. Since the combustion event is not described only by the increase of temperature in the combustion chamber, but also by increase of pressure (that is much easier to measure), the comparison is done looking at the second one, provided by Sandia experimental values. Also ignition delay values are analyzed.

Data regarding the rate of heat release (A.2) of the flame and pressure (A.1) could be used too to make this analysis, but since they are strictly related to the pressure rise rate, they are just reported for completeness in the Appendix A.

In addition, also temperature, acetylene C_2H_2, oxygen O_2 and hydroxyl OH spatial distributions are reported since they will be useful in order to analyze soot results (Chapter 6). For these parameters only the reference case (900 K 15% O_2) is reported in this Chapter. All the others are reported in A.3.

In all the shown pictures, $time = 0$ ms refers to the start of the injection (SOI).

5.1 Pressure rise rate and ignition delay

Pressure rise rate has been calculated starting from pressure profiles (see A.1). Experimental ignition delay is luminosity-based, i.e. it is the timing when intensity is 50% of high-T chemiluminescence [3], while the numerical one is obtained considering the instant at which temperature overcomes 1600 K.

Looking at the results, the first general observation is that the magnitude of the first peak, related to the premixed phase of the combustion, is different between experimental and numerical setups in any oxygen-temperature initial conditions. This value should be related also to the ignition delay one (e.g. if ignition delay increases, more mixture burns in premixed combustion mode), so the higher the ignition delay, the higher the peak [22]. Nevertheless, also when the models are able to catch correctly the ignition delay (Tab. 5.1), the magnitude of the peaks is overestimated. The model that seems to catch better the peaks magnitude is the TWM one (Fig. 5.2 and 5.5), while RIF and TRIF models apparently overestimate it everytime, in particular at 900 K 13% O_2 and 1000 K 15% O_2 conditions (Fig. 5.1, 5.3, 5.4 and 5.6). However there are experimental measurement issues related to sampling frequencies and filtering of the data that affect both magnitude (reduced by a factor of 2) and width (doubled) of the premixed peak value. Taking into account this fact, RIF and TRIF are better than TWM.

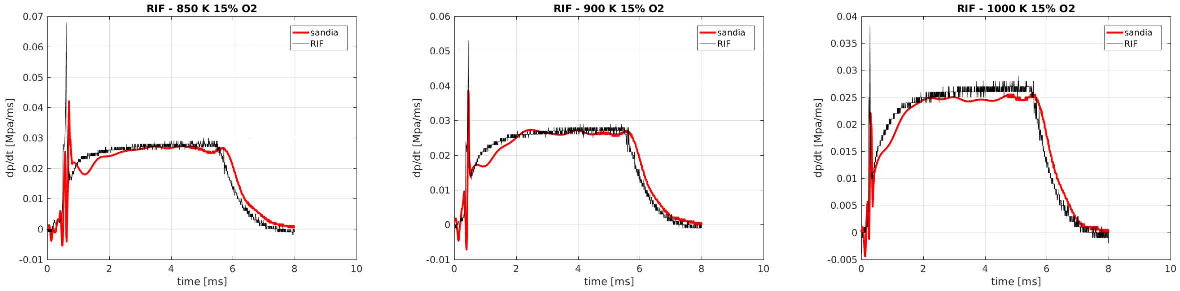

(a) 850 K (b) 900 K (c) 1000 K

Figure 5.1: RIF temperature sweep: pressure rise rate at 15% O_2

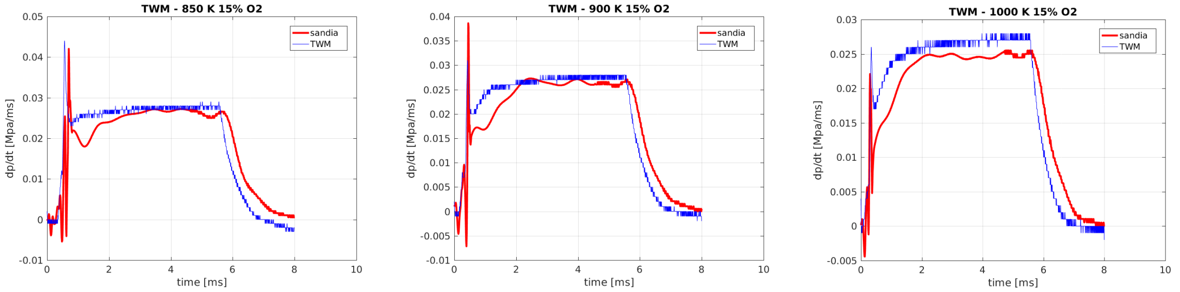

(a) 850 K (b) 900 K (c) 1000 K

Figure 5.2: TWM temperature sweep: pressure rise rate at 15% O_2

Also the timing of the first peak and ignition delay are strictly related: as it is possible to see in Tab. 5.1, at 850 K 15% O_2 and 900 K 13% O_2, none of the models is able to catch precisely the ignition delay. However, RIF gives acceptable results also in these setups. Proceeding towards higher oxygen concentrations and temperatures (Fig. 5.7, 5.8, 5.9), RIF and TWM models are very good, while TRIF suffers and it is able to reproduce correctly only the 900 K 15% O_2 condition. The underestimation of ignition delay in the tabulated models is partially justified by the problems related to auto-ignition (already described in Sections 2.3.1 and 2.3.2).

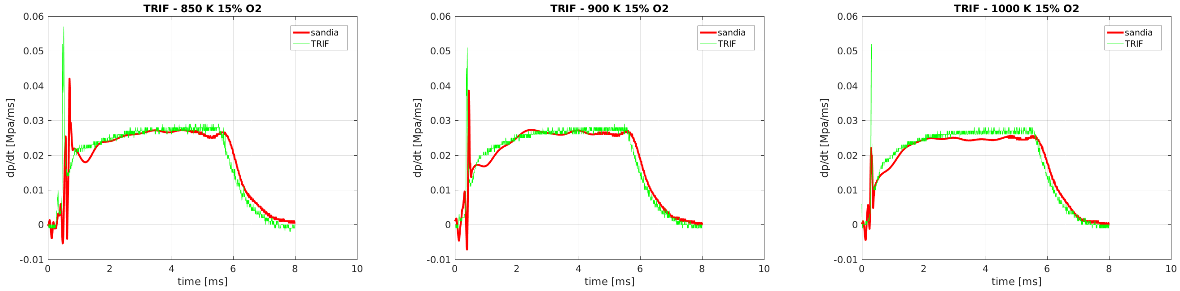

(a) 850 K (b) 900 K (c) 1000 K

Figure 5.3: TRIF temperature sweep: pressure rise rate at 15% O_2

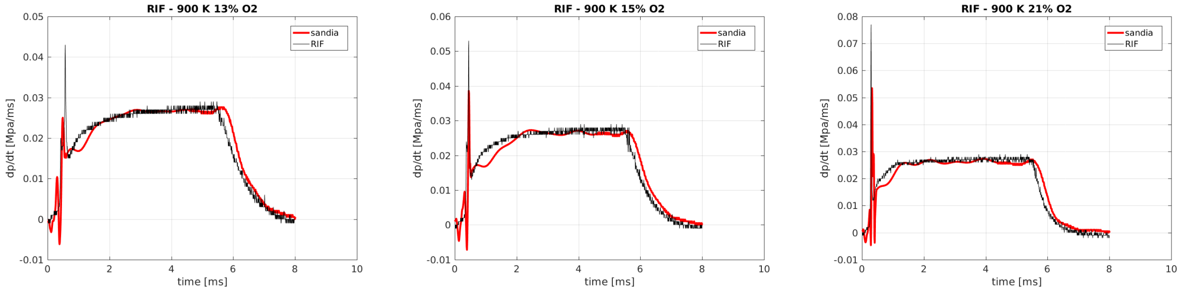

(a) 13% O_2 (b) 15% O_2 (c) 21% O_2

Figure 5.4: RIF oxygen sweep: pressure rise rate at 900 K

Nevertheless, the mixing-controlled phase of combustion is the most important for what concerns soot analysis because soot masses reach steady-state condition almost after 3 ms. So, for a correct soot prediction, a good reproduction of this combustion phase is required, while the premixed one is not so relevant. As it is possible to see, diffusive phase is generally well described in terms of pressure rise rate steady-state values. The only model that overestimates it significantly is TWM: probably it is caused by the higher flame temperature (Fig. 5.10 and Appendix A.3). This phenomenon is more evident at 1000 K 15% O_2 condition (Fig. 5.2).

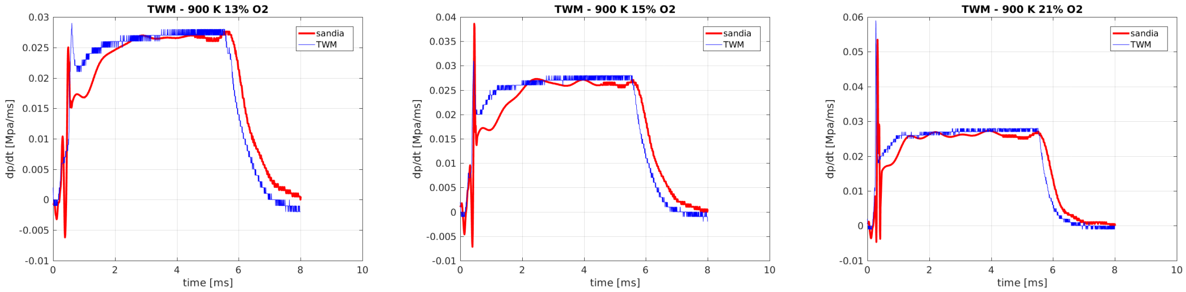

(a) 13% O_2 (b) 15% O_2 (c) 21% O_2

Figure 5.5: TWM oxygen sweep: pressure rise rate at 900 K

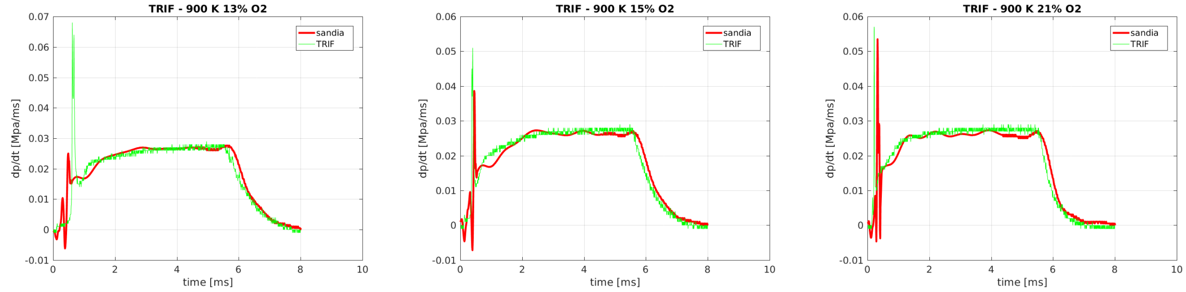

(a) 13% O_2 (b) 15% O_2 (c) 21% O_2

Figure 5.6: TRIF oxygen sweep: pressure rise rate at 900 K

Last combustion phase, also called burnout phase, corresponds to the flame extinction and it starts after the end of the injection. RIF (Fig. 5.1 and 5.4) and TRIF (Fig. 5.3 and 5.6) models perfectly match the experimental curves, while TWM (Fig. 5.2 and 5.5) pressure rise rates drop faster. Again it can be noticed that TWM behaviour is worst at 850 K 15% O_2 and 900 K 13% O_2 cases.

	850 K, 15% O_2	900 K, 13% O_2	900 K, 15% O_2	900 K, 21% O_2	1000 K, 15% O_2
Sandia	0.61	0.47	0.4	0.27	0.27
RIF	0.57450	0.52825	0.41850	0.28075	0.26225
TWM	0.50375	0.52175	0.37675	0.25325	0.26257
TRIF	0.49125	0.64475	0.38450	0.212	0.30275

Table 5.1: Ignition delay values (in [ms])

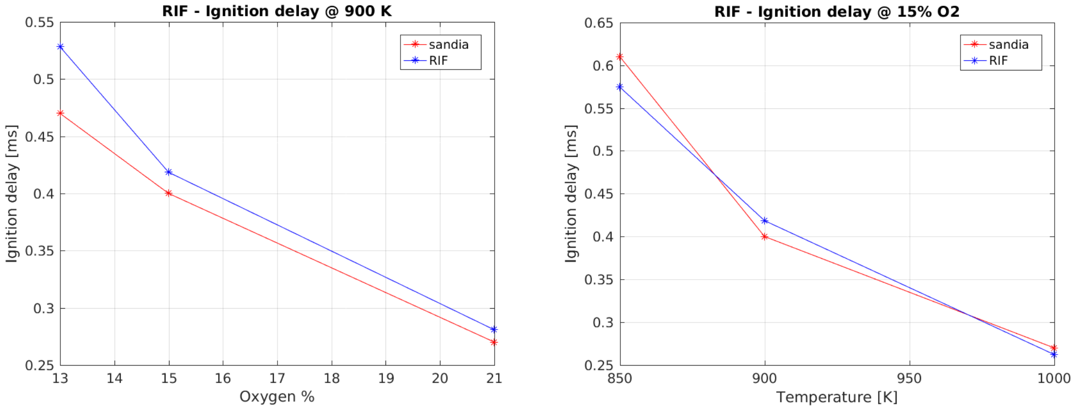

Figure 5.7: Ignition delay: RIF

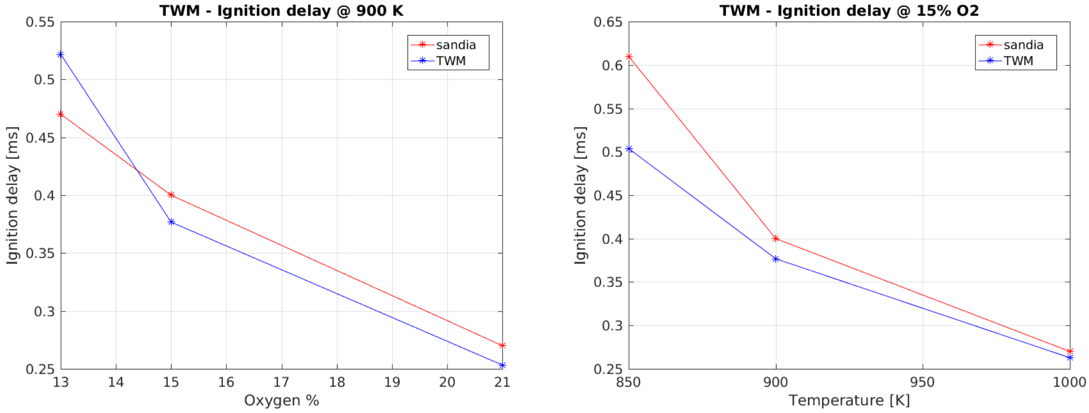

Figure 5.8: Ignition delay: TWM

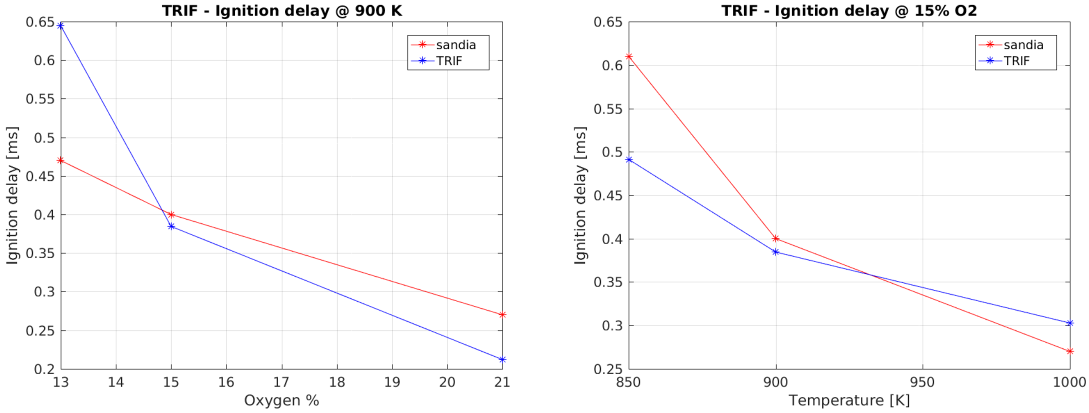

Figure 5.9: Ignition delay: TRIF

So the conclusion is that all the models are able to reproduce in a satisfactory way the combustion: in particular, RIF and TRIF are better in mixing-controlled and burnout phases. As it is said in [36], better results in terms of ignition delay can be achieved using *Pei* kinetic mechanism instead of *Faravelli* one.

However, from the computational time point of view, it is relevant that TWM model is the faster among the three method. In TRIF model it grows by 20%, while in RIF it almost doubles.

5.2 Temperature, C_2H_2, OH and O_2 spatial distributions

All the pictures reported here refer to the diffusive phase of the combustion (3.2 ms), the one when soot clouds reach their steady configuration (in fact, as explained in Chapter 4, Sandia performed the time-averaging of KL profiles between 2.5 ms and the end of the injection).

It worths to underline that spatial distributions are different because in RIF and TRIF model only one flamelet has been used. This leads to temperature and chemical species distributions up to the injector and so a wrong lift-off prediction. The usage of multiple flamelets solve this issue (as validated in [35]). However, since the required computational time increases a lot using this expedient, this limit is accepted.

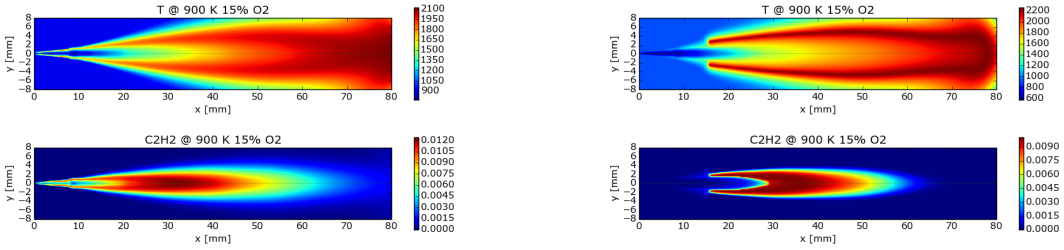

(a) RIF

(b) TWM

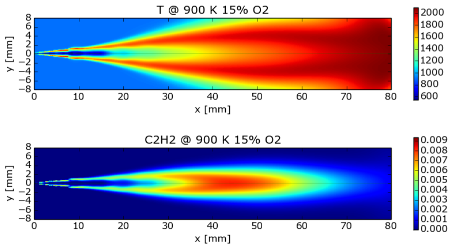

(c) TRIF

Figure 5.10: Temperature and acetylene distribution at 900 K 15% O_2

For what concerns temperature, TWM ones are higher (Fig. 5.10 and A.3) and high temperature region is extended closer to the injector and it is thinner in radial direction with respect to RIF and TRIF (that have very similar profiles and values) due to the absence of the turbulence-chemistry interaction.

	850 K 15% O_2	900 K 13% O_2	900 K 15% O_2	900 K 21% O_2	1000 K 15% O_2
RIF	0.012	0.0105	0.012	0.016	0.012
TWM	0.009	0.008	0.009	0.016	0.0105
TRIF	0.008	0.0064	0.008	0.012	0.009

Table 5.2: Peaks of acetylene concentration

As it can be observed in Tab. 5.2, acetylene concentrations in RIF model are very similar switching among different oxygen and temperature conditions, while in the other models they are more distanced (in particular, C_2H_2 at 900 K 21% O_2 is much higher than other conditions): this affects soot results (see Chapter 6). In addition, since it has an impact on the produced soot quantity, it worths to underline that for all combustion models acetylene concentration remains almost the same considering the temperature sweep while it changes a lot considering oxygen sweep (see Tab. 5.2 and A.3).

As it can be noticed in Fig. 5.11, 5.12 and 5.13, RIF has a wider acetylene concentration in the Z domain with respect to TRIF. This will lead to bad soot results (see Section 6.3.1).

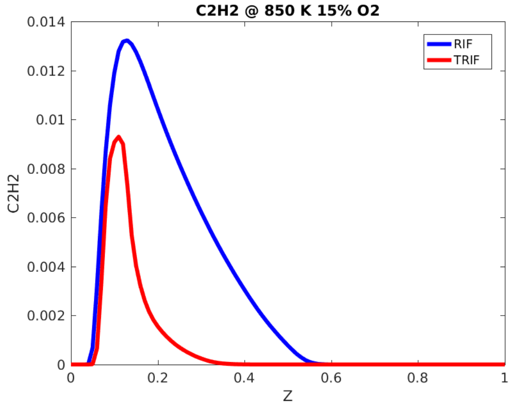

Figure 5.11: Acetylene concentration in chemical domain for RIF and TRIF model at 850 K 15% O_2

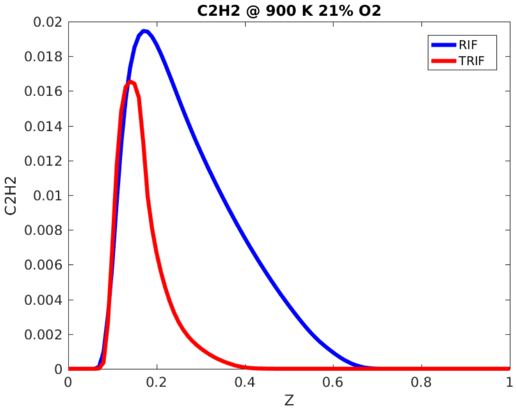

Figure 5.12: Acetylene concentration in chemical domain for RIF and TRIF model at 900 K 21% O_2

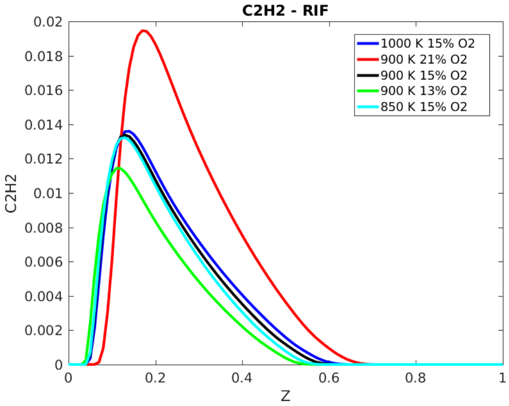

(a) RIF

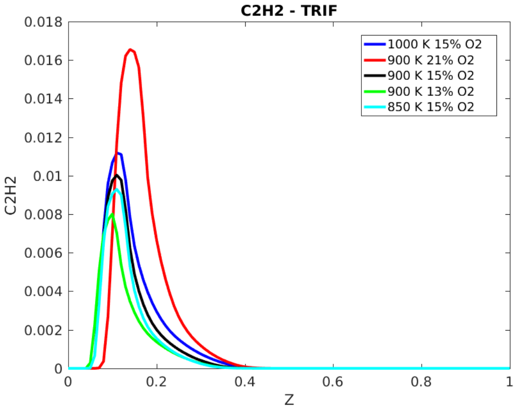

(b) TRIF

Figure 5.13: Acetylene distributions in Z domain for RIF and TRIF

Looking at O_2 and OH (Fig. 5.14), RIF and TRIF have similar spatial distribution with a wider concentration of OH downstream. Instead TWM has a very thin OH profile. As expected, O_2 is present only externally. The impact on soot oxidation of these aspects will be shown in Chapter 6.

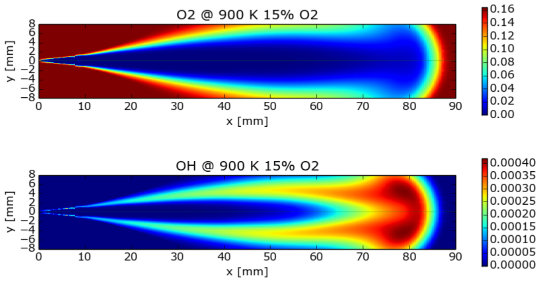

(a) RIF

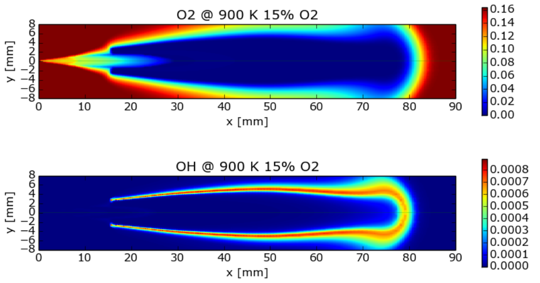

(b) TWM

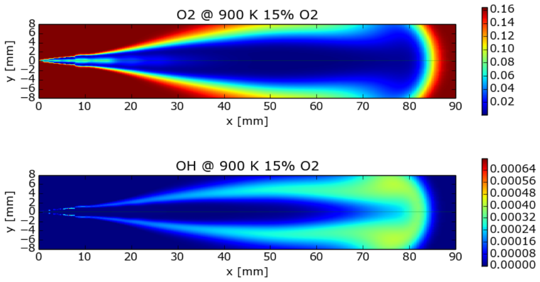

(c) TRIF

Figure 5.14: Oxygen and hydroxyl distribution at 900 K 15% O_2

Chapter 6

Soot Results

In this chapter, soot results obtained using the models validated in Chapter 5 are presented and compared with the experimental ones.

Cmin	100
aAlpha	1e4
Cbeta	3
bBeta	9e3
etaColl	1
cOmegaOH	1.08
cOmegaO2	3e4
TaOx	19800
Coxi	1
nBeta	0.5
TaAlpha	21100
TaBeta	12100
Schmidt soot number	0.7

Table 6.1: Starting constants

As anticipated before, soot prediction is a very difficult task. A detailed prediction would require complex and time-consuming models that are unfeasible in industrial applications. The main simplifications that are adopted in order to reduce computational time are related to simplified combustion models (using single flamelet in RIF based solvers, absence of turbulence-chemistry interaction and well-mixing hypothesis in TWM model) and chemistry (direct integration of chemical transport equations or tabulated approach) coupled with a semi-empirical soot model (see Chapter 2).

Features shown in Chapter 5 affect soot results. From the theoretical point of view the following statements should be verified:

- the higher the lift-off, the more downstream the soot clouds
- the lower the ignition delay, the closer to the injector the soot clouds
- position and quantity of acetylene influence position and amount of soot
- position and quantity of oxidizing species affect soot oxidation processes

All the simplifications of course leads to less accurate results. However it will be shown that good results are still achieved.

The starting point is the set of constants (Tab. 6.1) proposed by Bolla [34], that are very similar to the ones suggested by Leung [30].

The results obtained using this set with the combustion models described in this work are clearly unacceptable. Just to give an idea, soot clouds using RIF, TWM and TRIF at 900 K 15% O_2 are reported in Fig. 6.1. Soot masses in function of time are not reported since their values are completely out of scale with respect to Sandia ones. In order to state if combustion models RIF, TWM and TRIF are capable to reproduce well the soot clouds using Leung soot model, a calibration must be done. The guidelines of this process are the comparison (with respect to soot Sandia data) of :

- Soot cloud shapes
- Soot cloud positions
- Peak values of soot volume fraction f_v (Tab. 6.2)
- Soot masses as function of time

	f_v peaks [ppm]
850 K 15% O_2	1.436
900 K 13% O_2	5.243
900 K 15% O_2	6.945
900 K 21% O_2	9.094
1000 K 15% O_2	14.415

	$\frac{f_{v_i}}{f_{v_{1000_{15}}}}$
850 K 15% O_2	0.1
900 K 13% O_2	0.364
900 K 15% O_2	0.482
900 K 21% O_2	0.631
1000 K 15% O_2	1

Table 6.2: Sandia f_v peak values and normalized peaks (with respect to 1000 K 15% O_2)

Due to all the simplifications, compromises must be done: in particular, the priority is to catch well the masses. However, the interest is more focused on the understanding of the Leung model behaviour rather than a pure calibration.

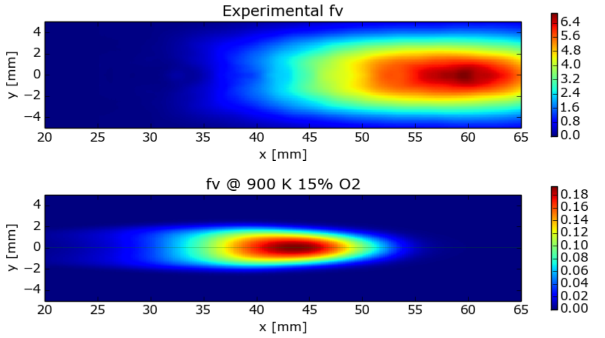

(a) RIF.

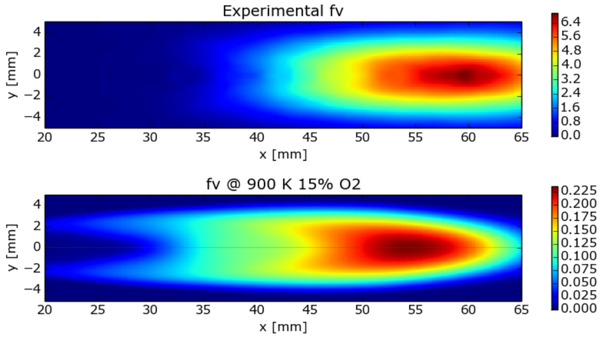

(b) TWM.

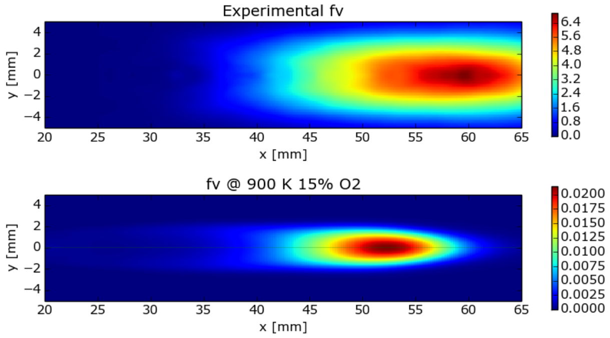

(c) TRIF.

Figure 6.1: Soot results using starting constants at 900 K 15% O_2

It worths to underline that not all these features are directly related: for instance, it is not true that big f_v values necessarily correspond to large clouds; on the other hand, soot mass depends on all the other parameters. But it is difficult to say it a priori for each model because, for example, it is not possible to say if large cloud shape and low f_v will provide high or low mass. All these topics will be discussed in the next sections.

In order to understand what is the impact of the single sub-process on soot results, a *trial-and-error* analysis was done modifying each time a specific soot constant (see Section 3.3.5). Of course this method is not optimized and it is time-consuming, but as said before the way of proceeding is not a black-box approach that tries to get best matching between numerical and experimental results.

Please notice that :

- in all the results presented here, soot volume fraction f_v is expressed in $[ppm]$ and the rates of creation and destruction are $[1/s]$
- all the results refer to an instant in which soot cloud reaches steady state (3.2 ms)

Now all soot results obtained with all the combustion models for oxygen and temperature sweeps are presented.

6.1 TWM

6.1.1 Optimal soot model constants

Cmin	100
aAlpha	2e5
Cbeta	3
bBeta	6e4
etaColl	1
cOmegaOH	1
cOmegaO2	2.5e4
TaOx	39600
Coxi	0.6
nBeta	0.5
TaAlpha	35000
TaBeta	12100
Schmidt soot number	0.7

Table 6.3: TWM: optimal soot model constants

As it is possible to see in Tab. 6.3, some significant variations from the original set are done. Looking at Fig. 6.1, of course the first thing to do is trying to increase the amount of soot, recalling that the phenomena that increase the soot mass are nucleation and surface growth. First, pre-exponential terms *aAlpha* and *bBeta* are changed in order to understand how they scale the soot volume fraction.

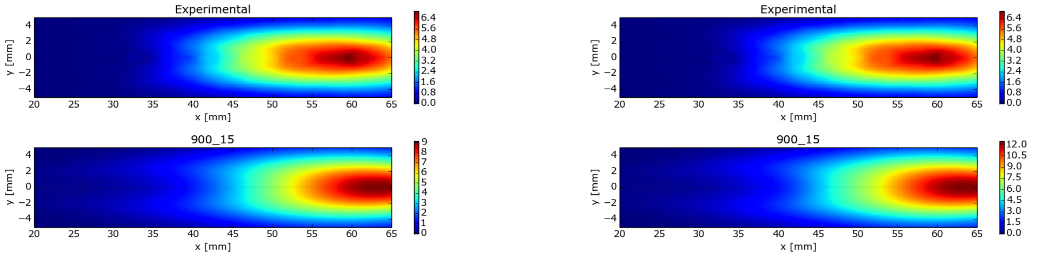

(a) $bBeta = 25000$

(b) $bBeta = 30000$

Figure 6.2: Effect of *bBeta* increasing at 900 K 15% O_2: f_v peak changes without cloud shape or position modifications

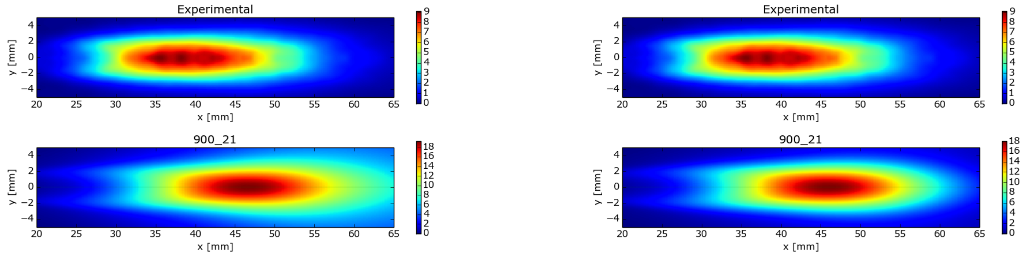

(a) $Coxi = 0.01$

(b) $Coxi = 0.05$

Figure 6.3: Effect of *Coxi* variation at 900 K 15% O_2 on soot cloud

In practice, the target is to reach the correct order of magnitude for the soot volume fractions and to see if, at least, the f_v peaks are well reproduced if compared to Sandia ones, considering that the starting numerical results were too close among themselves. This is crucial because an over/under-estimation of f_v peaks can affect the overall masses. What is noticed is that by increasing them, the correct order of magnitude of f_v peaks is reached, but the required scaling (indicated in Tab. 6.2) is not respected, and of course also masses suffer this. So the conclusion is that pre-exponential terms for nucleation and surface growth are not able to correct the wrong scaling of the starting numerical soot volume fractions.

In order to overcome this limit, oxidation pre-exponential term *Coxi* is reduced. The reasoning behind this is that at 1000 K 15% O_2 and 900 K 21% O_2 cases oxidation is stronger, so a reduction of *Coxi* should produce a higher reduction of oxidation rate with respect to the other cases. However, this effect is not observed, but at the same time soot clouds become larger (in particular in radial direction).

This can be observed in Fig. 6.3, in which only *Coxi* is changed. Same results are obtained acting on *cOmega* coefficients. Variations of *Cbeta* and *Cmin* do not produce significant variations, so they are kept equal to the starting ones.

At this point it is necessary to understand if the problem is related to a not accurate estimation of the activation temperature: since differences in temperature between the flames are observed (see Appendix A), it is possible that they play a key role in soot formation/destruction.

The first changed parameter is the exponential term of O_2 oxidation *TaOx*, since as said before oxidation is very high at 1000 K 15% O_2 and 900 K 21% O_2 cases if compared to the others. An increase of *TaOx* acts this way, without decreasing so strongly the way O_2 oxidizes the other cases. Of course, as it can be seen in Section 6.1.3, O_2 oxidation rates become almost negligible with respect to OH one. This seems to validate what it is said in previous Chapters (1.2.5). Resuming, the increase of *TaOx* has two positive effects:

- enlarging the soot clouds
- distancing the f_v peaks

This is clear looking at Fig. 6.4: if *TaOx* doubles, soot cloud becomes very large. This fact seems to be negative, but the reported pictures refer to a set of constants with a very low value of *Coxi* equal to 0.01. Coupling a high *TaOx* together with a high *Coxi* (as the chosen value 0.6) gives good shapes and peaks distancing.

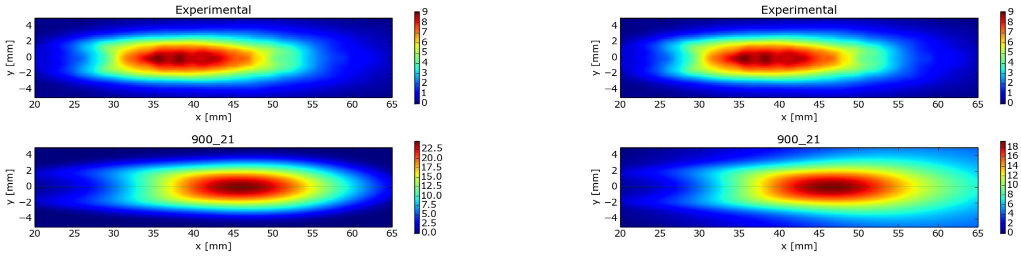

(a) $TaOx = 19800$ (b) $TaOx = 39600$

Figure 6.4: Effect of the increase of *TaOx* at 900 K 21% O_2 on soot cloud

Therefore an increase over a value of 39600 does not produce a further improvement of these effects since O_2 oxidation reaches almost negligible values. In order to get better results in this sense, also exponential terms of nucleation (*TaAlpha*) and surface growth (*TaBeta*) are modified. Good results are obtained increasing *TaAlpha* (and keeping fixed *TaBeta*), since it decreases strongly the nucleation of soot particles in particular at cases with lower temperatures. In this way, the increase of soot mass is almost totally controlled by surface growth. Similar results are obtained increasing *TaBeta* and keeping fixed *TaAlpha*, even if this time surface growth and nucleation rates become comparable.

Increasing both of them, soot almost disappears, while decreasing them soot clouds become huge because also at lower temperatures soot formation is activated, so the masses are not acceptable. So a choice between increasing *TaBeta* and increasing *TaAlpha* must be done: since there is no experimental evidences to make comparison with obtained nucleation and surface growth rates, a higher *TaAlpha* is chosen since it gives better results in term of total soot mass (that is the primary aim of this work) and cloud shape (since the behaviour is the same observed for TRIF, see Fig. 6.18). The good effect provided by *TaAlpha* increase is reinforced by high values of its pre-exponential term *aAlpha*.

For what concerns *Schmidt soot number*, some attempts have been perfomed increasing and decreasing it starting from the initial value:

- if decreased (down to 0.5), radial extension of the soot cloud is increased while axial one is reduced, and globally cloud is shifted backward

- if increased (up to 0.85), radial extension is reduced while the axial is increased; globally cloud is shifted forward

But at the end the starting value is the best one. The choice of it is justified assuming a minimum soot particle size diameter of around 1.24 nm [30], and this value agrees with the considerations made by [10]. Since these considerations are the same also for TRIF, the trend shown in Fig. 6.17 is valid also for TWM.

Resuming, the chosen set of constants for TWM (Tab. 6.3) tries to keep into account all the guidelines specified above. However two big compromises must be accepted:

- soot volume fraction peak value at 900 K 21% O_2 is largely over-estimated (Fig. 6.8) and there is no way to reduce it: in all the done attempts, it always remains much bigger than the experimental and the other numerical ones

- behaviour of the soot model at 850 K 15% O_2 is not clear: in experimental data, only a very weak soot cloud is generated, while in all the calculations it is always overestimated in terms of f_v, cloud dimension (Fig. 6.5) and mass (Fig. 6.16); since at 900 K 15% O_2 the model works properly (Fig. 6.7), a possible explaination is that in this 50 K range there is a physical phenomenom that is not well caught by the combustion or soot model

6.1.2 Soot volume fractions

	f_v peaks [ppm]
850 K 15% O_2	4.826
900 K 13% O_2	3.3209
900 K 15% O_2	7.14517
900 K 21% O_2	21.7624
1000 K 15% O_2	13.059

	$\frac{f_{v_i}}{f_{v_{1000_{15}}}}$
850 K 15% O_2	0.3695
900 K 13% O_2	0.2543
900 K 15% O_2	0.5471
900 K 21% O_2	1.666
1000 K 15% O_2	1

Table 6.4: TWM f_v peak values and normalized peaks (with respect to 1000 K 15% O_2)

For what concerns the soot volume fractions, apart from 850 K 15% O_2 and 900 K 21% O_2, peaks are quite well scaled. Considering the scaling, the 900 K 13% O_2 and 900 K 15% O_2 normalized f_v values are very good (Tab. 6.4). Cloud shapes are obtained making a compromise because the three cases at 900 K have the correct radial and axial extension, while it is impossible to extend radially the 1000 K 15% O_2 case without worsening the others (a small enlargement is paid by huge ones at 900 K). Clouds positions are well reproduced for all the cases.

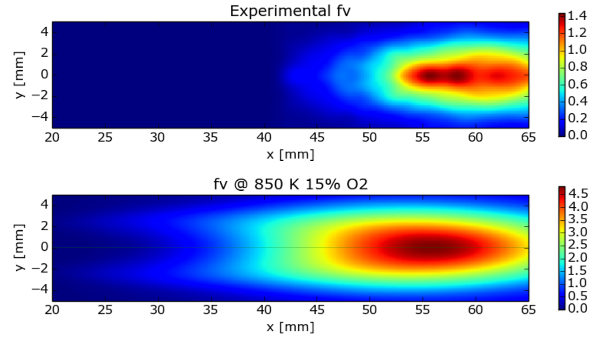

Figure 6.5: TWM: soot volume fraction at 850 K and 15% O_2

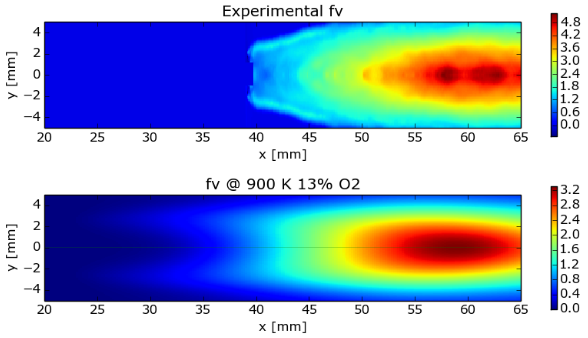

Figure 6.6: TWM: soot volume fraction at 900 K and 13% O_2

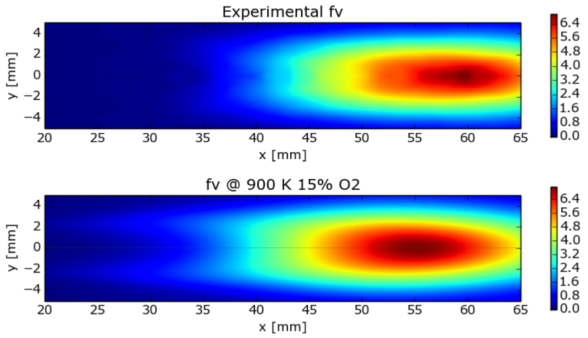

Figure 6.7: TWM: soot volume fraction at 900 K and 15% O_2

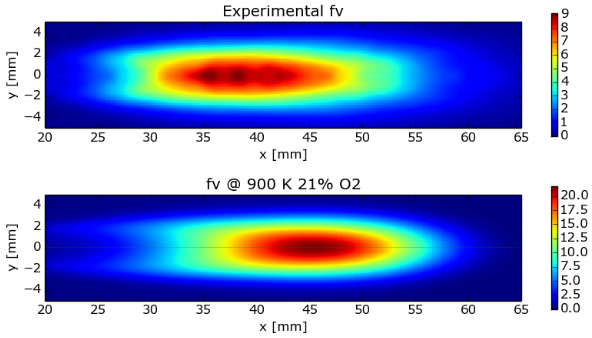

Figure 6.8: TWM: soot volume fraction at 900 K and 21% O_2

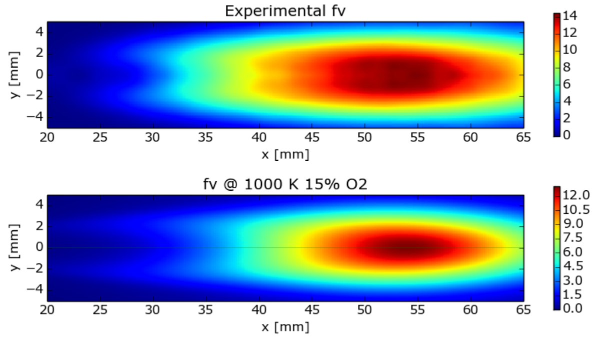

Figure 6.9: TWM: soot volume fraction at 1000 K and 15% O_2

6.1.3 Rates of creation and destruction

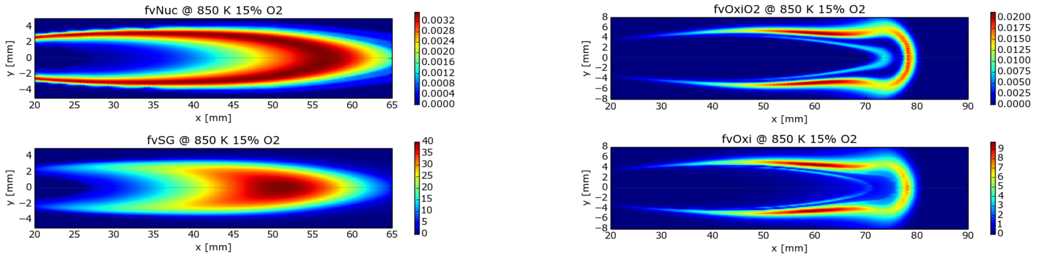

Figure 6.10: TWM: rates of nucleation, surface growth and oxidation at 850 K and 15% O_2

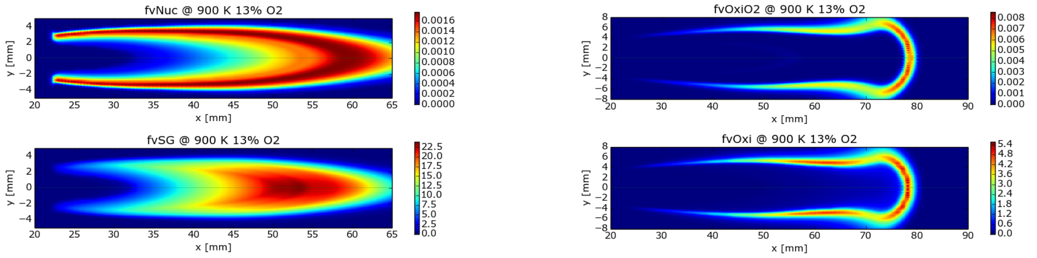

Figure 6.11: TWM: rates of nucleation, surface growth and oxidation at 900 K and 13% O_2

The choice of constants (Section 6.1.1) affects the values of all these rates. However, it is interesting to notice that oxidation rates by both the oxidizing agents are confined in a very thin region that is strictly related to OH and O_2 distributions (see Section 5.14 and Appendix A.3): O_2 is of course peripheric to the core of soot, while OH lies in a very thin region. Instead surface growth rate has a very close shape to C_2H_2 distribution (Fig. 5.10 and Appendix A.3).

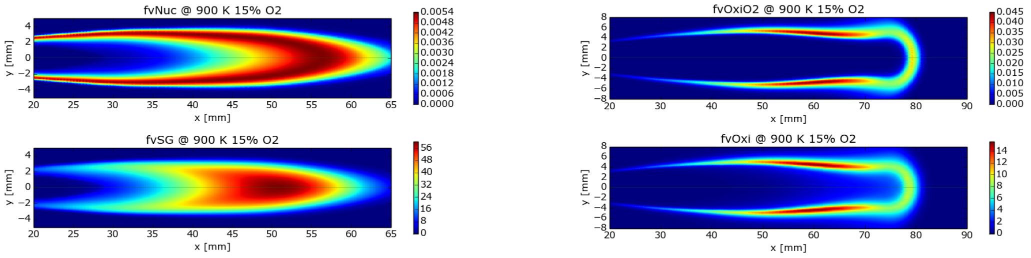

Figure 6.12: TWM: rates of nucleation, surface growth and oxidation at 900 K and 15% O_2

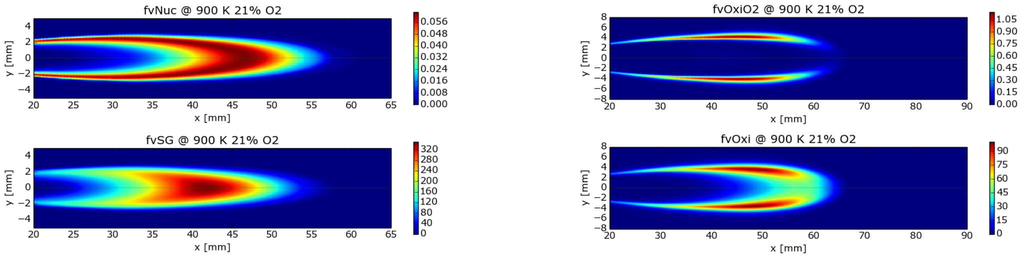

Figure 6.13: TWM: rates of nucleation, surface growth and oxidation at 900 K and 21% O_2

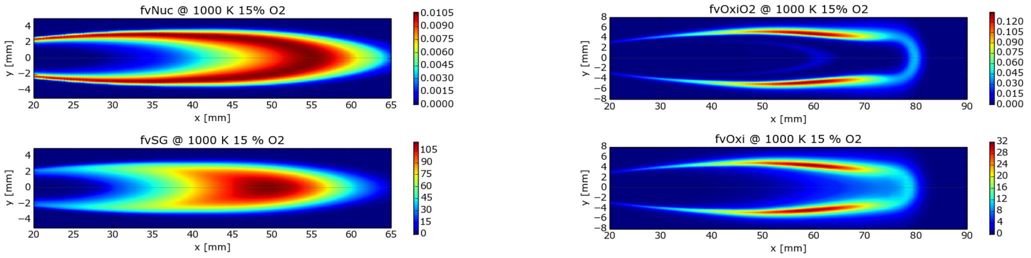

Figure 6.14: TWM: rates of nucleation, surface growth and oxidation at 1000 K and 15% O_2

6.1.4 Integral soot masses

Masses are reported considering sweeps of oxygen (Fig. 6.15) and temperature (Fig. 6.16) in order to analyze the sensitivity of the model with respect to temperature and oxygen variations. Looking at oxygen sweep, mass profiles are well scaled considering the steady state value; the absolute values are higher than experimental ones, but this is required in order to have also a good absolute value of mass at 1000 K 15% O_2 with the selected soot constants.

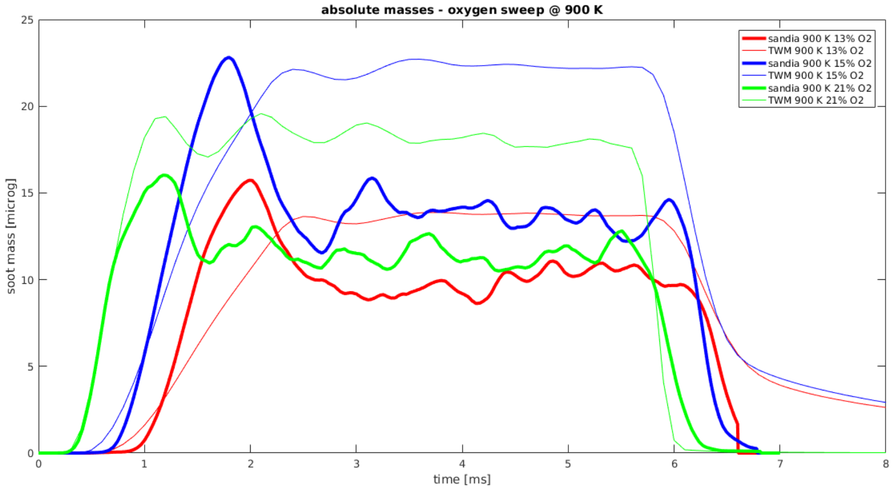

Figure 6.15: TWM: masses, oxygen sweep

In particular:

- 1000 K 15% O_2: mass is underestimated because of smaller soot cloud and lower f_v value (Fig. 6.9)
- 900 K 21% O_2: mass is overestimated because of higher f_v only (Fig. 6.8)
- 900 K 15% O_2: mass is overestimated because of bigger soot cloud (Fig. 6.7)
- 900 K 13% O_2: despite a smaller f_v peak, mass is overestimated because of the presence of a big and concentrated soot core region that, as we can see in Fig. 6.6, is very small in the experimental data
- 850 K 15% O_2: as anticipated, soot mass is overestimated

Soot mass profiles clearly show that TWM is not able to reproduce the first peak and it directly stabilizes around the steady-state value at the same time of experimental profiles. The only exception is 900 K 21% O_2 case: here the model is more reactive, since the curve grows exactly as the experimental one and it reaches the first peak at the same time.

Looking at what happens in the post-injection phase, at 900 K 21% O_2 the extinguishing of the soot is ever faster than the experimental one (due to the high amount of oxidizers available). The other 900 K cases have a weaker post-injection oxidation due to the lower quantity of oxidizers available, while case at 1000 K is a bit faster. Value of soot mass at 850 K 15% O_2 is much higher than the experimental one, so it is difficult to do this kind of considerations.

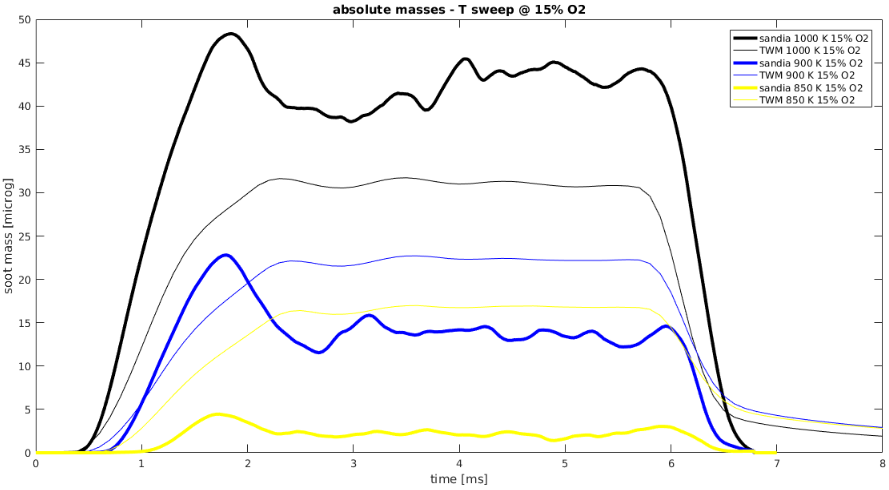

Figure 6.16: TWM: masses, temperature sweep

In Tab. 6.5 the onset of soot (based on the achievement of 5% of the peak soot mass of each case) is reported: at lower values of oxygen and temperature (850 K 15% O_2, 900 K 13% O_2, 900 K 15% O_2), numerical onsets are smaller than experimental ones. It means that soot starts generating before, even if afterwards the growing is slower for the numerical model (Fig. 6.15 and 6.16). On the other hand, onsets at 900 K 21% O_2 and at 1000 K 15% O_2 are well caught and this means that soot starts generating at the same instant: as anticipated, at 900 K 21% O_2 also the first part of the growing is the same, while for numerical 1000 K the growing process is slower.

	850 K 15% O_2	900 K 13% O_2	900 K 15% O_2	900 K 21% O_2	1000 K 15% O_2
Sandia	1.05	1.01	0.785	0.385	0.575
TWM	0.7102	0.8603	0.6416	0.37	0.5517

Table 6.5: TWM: onset of soot [ms]

6.2 TRIF

6.2.1 Optimal soot model constants

Cmin	100
aAlpha	5e4
Cbeta	3
bBeta	6.5e4
etaColl	1
cOmegaOH	1.08
cOmegaO2	0.2e4
TaOx	39600
Coxi	0.7
nBeta	0.5
TaAlpha	35000
TaBeta	12100
Schmidt soot number	0.7

Table 6.6: TRIF: optimal soot model constants

The calibration procedure for TRIF model is done applying the same logic of the TWM (Section 6.1.1). The main difference is that the starting point (i.e. Fig. 6.1) is a set of soot clouds that are thinner and with very low f_v peaks. For this reason, pre-exponential terms related to soot mass increasing (*aAlpha, bBeta*) are raised up to values that are a little bit higher than TWM ones.

Since starting soot cloud has a small radial and axial extension, the most efficient way to enlarge it is to reduce the oxidation; in particular, a reduction of pre-exponential term of O_2 oxidation (*cOmegaO2*) leads to significant reduction of this phenomenon in peripheral regions. Of course, after this change, O_2 oxidation rate becomes almost negligible.

For what concerns exponential terms, the same concepts applied in TWM are well suitable also for TRIF:

- the increasing of *TaOx* contributes to f_v peaks distancing and to soot cloud enlarging
- the increasing of *TaAlpha* decreases strongly soot nucleation at lower temperature cases, and it is more effective than the increasing of *TaBeta;* considering Fig. 6.18, the set of constants is the same except for *TaBeta* = 20000 (Fig. 6.18a) and *TaAlpha* = 25000 (Fig. 6.18b). It is clear that an increase of *TaBeta* worsens the shape of the cloud tail and reduces radial extension, especially in the front part of the soot cloud. This fact further justifies the choice of adopting an increased *TaAlpha* rather than an increased *TaBeta*

- same considerations regarding *Schmidt soot number* are valid; for example, in Fig. 6.17 the effect of its variation is reported: in Fig. 6.17a and 6.17b *Schmidt soot number* is the only changed parameter; in Fig. 6.17c, also *bBeta* has been changed, but the strong shape variation is provided by Schmidt increase because, as anticipated, pre-exponential terms for nucleation and surface growth act only on f_v values without changing significantly the shape

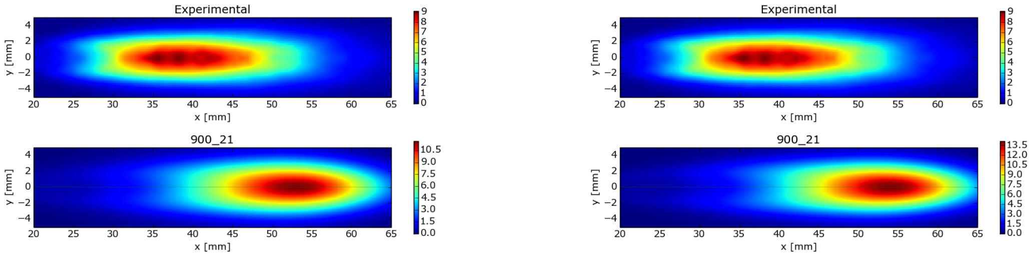

(a) $Schmidt\,soot\,number = 0.5$ (b) $Schmidt\,soot\,number = 0.7$

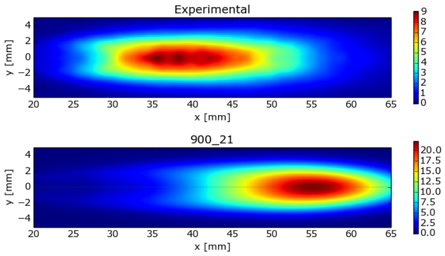

(c) $Schmidt\,soot\,number = 0.85$

Figure 6.17: Effect of Schmidt soot number on soot cloud at 900 K 21% O_2 case

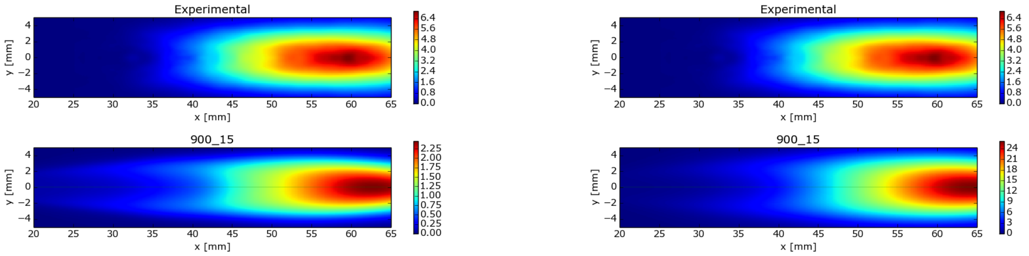

(a) Increase of *TaBeta* (b) Increase of *TaAlpha*

Figure 6.18: Effects of *TaBeta* and *TaAlpha* on soot cloud at 900 K 15% O_2

- same compromises related to 850 K 15% O_2 and 900 K 21% O_2 must be accepted

However, there are some differences with respect to TWM. Soot cloud positions are all shifted downstream from the injector, so it is difficult to make comparisons with Sandia soot clouds: the only one entirely contained in the optical window is 900 K 21% O_2 case, and it is easy to see that front part of cloud is worse than TWM one (this is related to spatial distribution of oxidation rates as it will be clear in Section 6.2.3).

6.2.2 Soot volume fractions

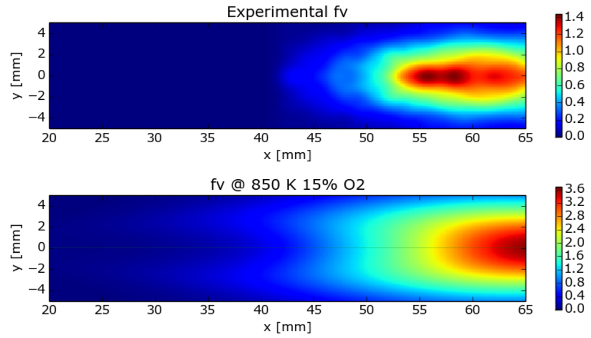

Figure 6.19: TRIF: soot volume fraction at 850 K and 15% O_2

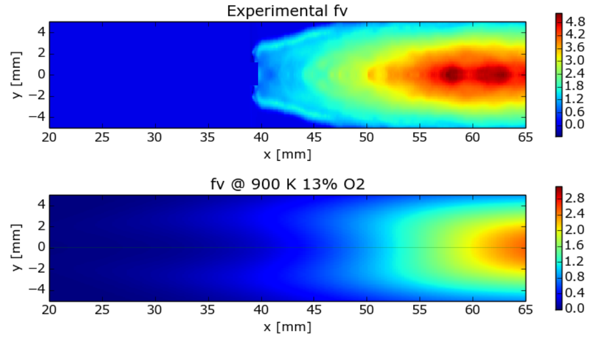

Figure 6.20: TRIF: soot volume fraction at 900 K and 13% O_2

The absolute values of f_v peaks are less accurate with respect to TWM. Considering the relative distance among the peaks (i.e. normalized peaks, Tab. 6.7), results are similar to TWM. So it could be easy to raise all the absolute peaks values just by increasing one of the pre-exponential terms without changing the normalized ones; however, it is not done for a matter of mass (Section 6.2.4).

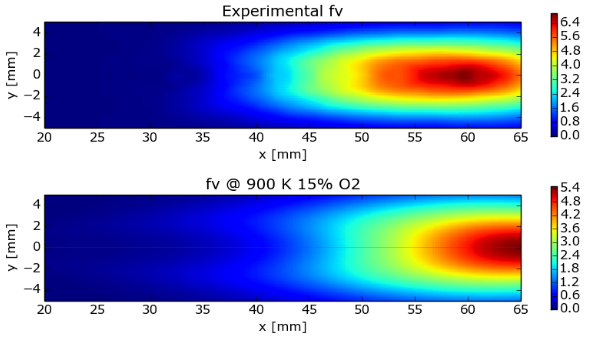

Figure 6.21: TRIF: soot volume fraction at 900 K and 15% O_2

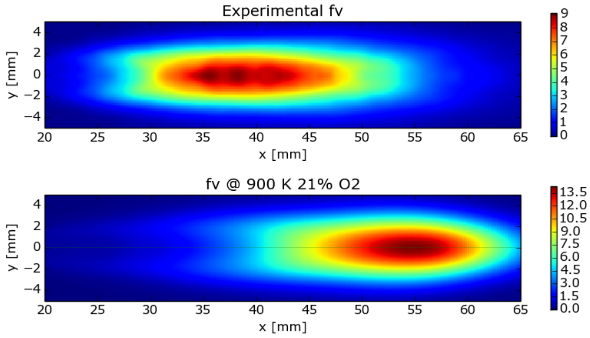

Figure 6.22: TRIF: soot volume fraction at 900 K and 21% O_2

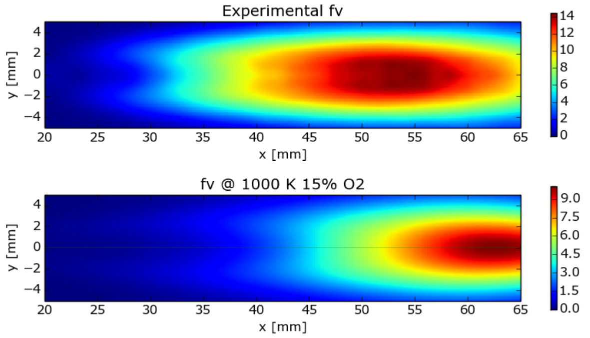

Figure 6.23: TRIF: soot volume fraction at 1000 K and 15% O_2

The soot cloud shifting described above can be justified by looking at acetylene spatial distribution (see Section 5.10 and Appendix A.3): for TRIF combustion model, C_2H_2 is concentrated more downstream with respect to other combustion models and so soot clouds. So, clearly, this is an issue related to combustion models accuracy and not to Leung model.

	f_v peaks [ppm]
850 K 15% O_2	3.69119
900 K 13% O_2	3.12013
900 K 15% O_2	5.51666
900 K 21% O_2	14.3093
1000 K 15% O_2	10.0729

	$\frac{f_{v_i}}{f_{v_{1000_{15}}}}$
850 K 15% O_2	0.3664
900 K 13% O_2	0.3097
900 K 15% O_2	0.5476
900 K 21% O_2	1.4205
1000 K 15% O_2	1

Table 6.7: TRIF f_v peak values and normalized peaks (with respect to 1000 K 15% O_2)

6.2.3 Rates of creation and destruction

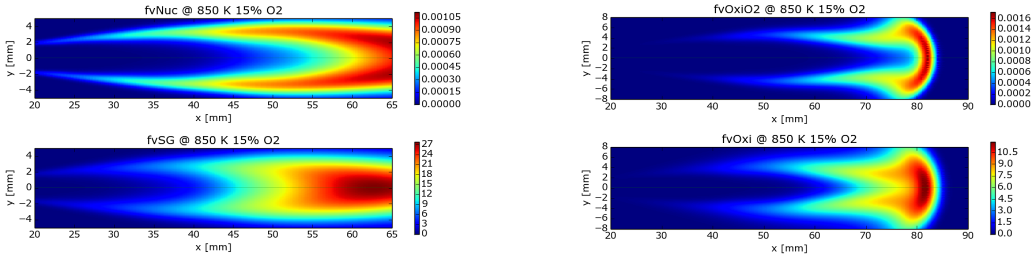

Figure 6.24: TRIF: rates of nucleation, surface growth and oxidation at 850 K and 15% O_2

Also in this case, the choice of constants (Tab. 6.6) affects the rates values (for example the fact that OH oxidation rate is much higher than O_2 one). As anticipated, since acetylene is generated downstream, rates of nucleation and surface growth are shifted too with respect to TWM model. Absolute values have the same order of magnitude seen in TWM (Fig. 6.1.3). Rates of oxidation, instead are completely different: *fvOxi* and *fvOxiO2* are concentrated in the front part of the soot cloud (Fig. 6.24, 6.25, 6.26, 6.27, 6.28), while in TWM they are distributed mainly radially far from the axis. This causes a thinner front part (as seen in Fig. 6.22), but at the same time it can be observed (Fig. 6.21) that high f_v soot regions (the red and orange ones) are wider. That is why soot masses are good even if f_v peaks are smaller with respect to experimental ones.

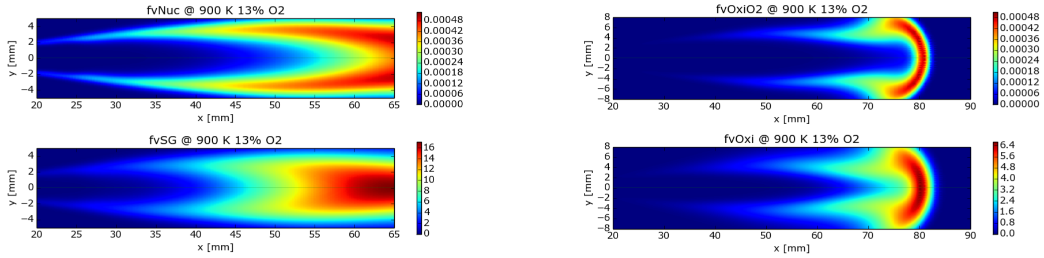

Figure 6.25: TRIF: rates of nucleation, surface growth and oxidation at 900 K and 13% O_2

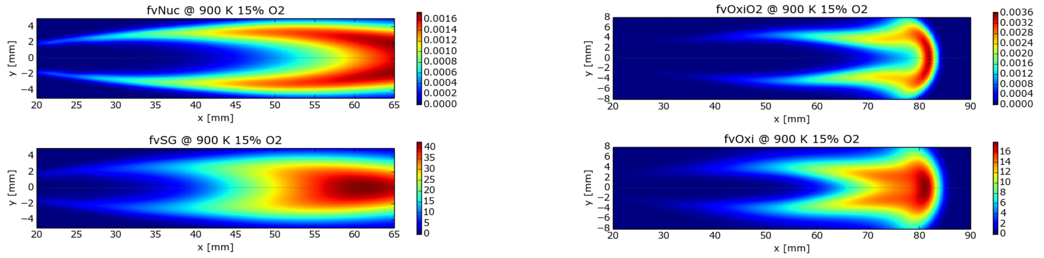

Figure 6.26: TRIF: rates of nucleation, surface growth and oxidation at 900 K and 15% O_2

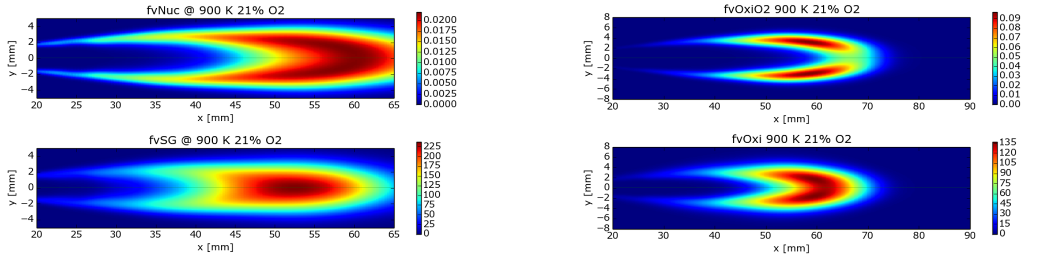

Figure 6.27: TRIF: rates of nucleation, surface growth and oxidation at 900 K and 21% O_2

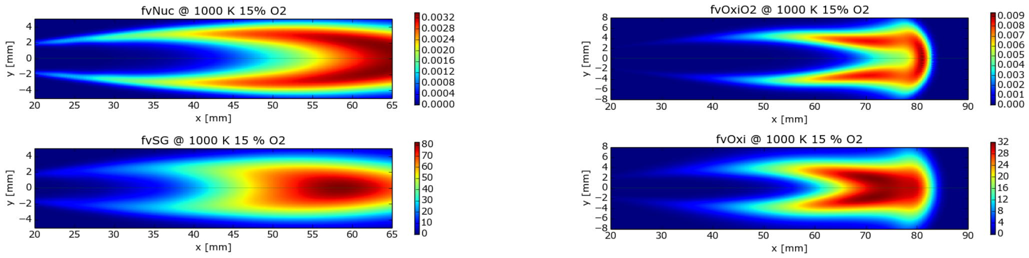

Figure 6.28: TRIF: rates of nucleation, surface growth and oxidation at 1000 K and 15% O_2

6.2.4 Integral soot masses

Again, masses are reported considering oxygen and temperature sweeps. The peculiarity of TRIF model is that it is able to correctly reproduce the overall behaviour of soot mass profile: it catches well the first peak and then it stabilizes down to a steady-state value. Oxygen sweep (Fig. 6.29) is very well reproduced, even if it seems that profiles are a bit overestimated in high oxygen configurations. The temperature sweep (Fig. 6.30) suffers again (as in TWM) the impossibility of reproducing correctly masses of 850 K 15% O_2 and 1000 K 15% O_2 cases.

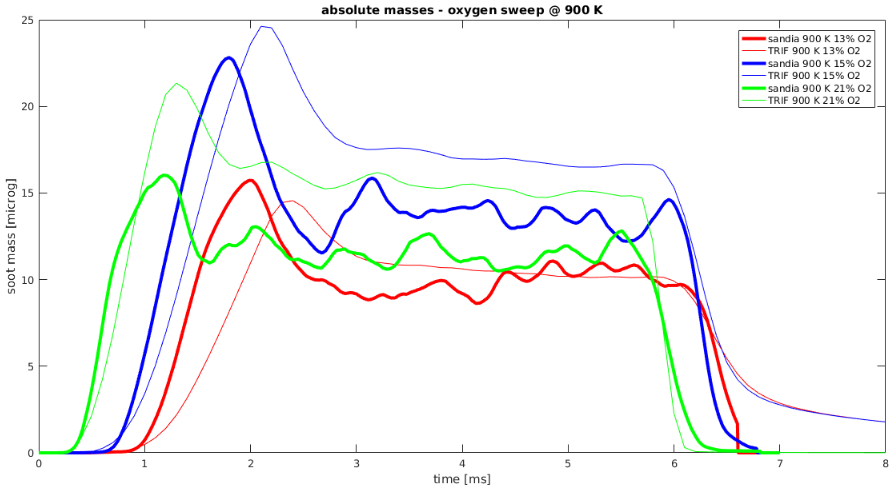

Figure 6.29: TRIF: masses, oxygen sweep

In particular:

- 1000 K 15% O_2: soot mass is underestimated since f_v peak is underestimated (Fig. 6.23)
- 900 K 21% O_2: soot mass is overestimated because f_v peak is overstimated (Fig. 6.22)
- 900 K 15% O_2: soot mass is overestimated even if f_v peak is underestimated because high core soot region is wider (Fig. 6.21)
- 900 K 13% O_2: soot mass is caught very good because, althought f_v peak is underestimated, high core soot region is wider (Fig. 6.20)
- 850 K 15% O_2: soot mass is overestimated since soot cloud is very far in terms of peak and shape with respect to the experimental one (Fig. 6.19)

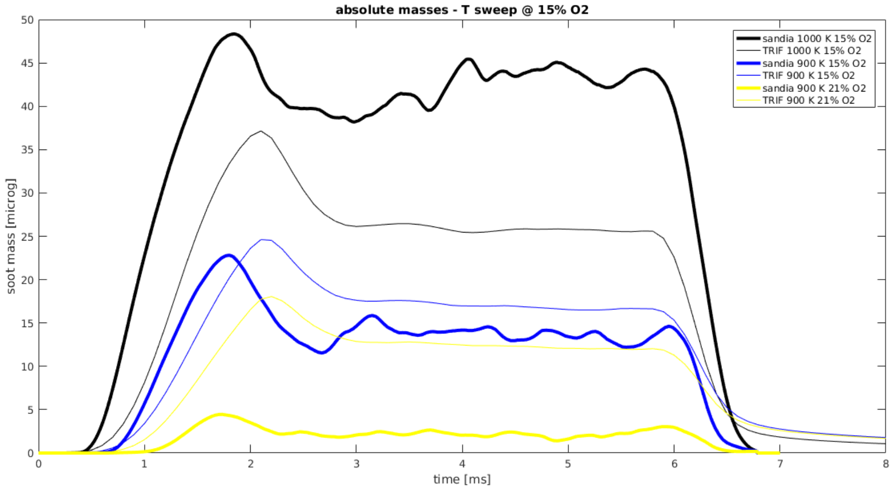

Figure 6.30: TRIF: masses, temperature sweep

Soot onset values (Tab. 6.8) are well reproduced, but the increasing of soot mass profile is significantly slower at 1000 K 15% O_2 and 900 K 13% O_2, while increasing the percentage of oxygen at 900 K, the model is more reactive (as observed for TWM). Also the timing of the soot extinction after the end of the injection shows that with low amount of oxygen the residual soot mass is not oxidized properly. By looking at 1000 K 15% O_2 mass profile, it is clear that high starting temperature helps in oxidizing residual soot mass. However it seems that more oxygen is more effective, also because at 900 K 21% O_2 higher flame temperatures are reached (Appendix A.3).

	850 K 15% O_2	900 K 13% O_2	900 K 15% O_2	900 K 21% O_2	1000 K 15% O_2
Sandia	1.05	1.01	0.785	0.385	0.575
TRIF	0.9457	1.0345	0.8938	0.4173	0.7029

Table 6.8: TRIF: onset of soot [ms]

6.3 RIF

6.3.1 Optimal soot model constants

Cmin	100
aAlpha	6e6
Cbeta	3
bBeta	1.6e4
etaColl	1
cOmegaOH	1
cOmegaO2	0.2e4
TaOx	39600
Coxi	0.1
nBeta	0.5
TaAlpha	32000
TaBeta	12100
Schmidt soot number	0.7

Table 6.9: RIF: optimal soot model constants

RIF combustion model has been widely validated in past works, and it is accepted that it can efficiently simulate all the flow fields. The main issue of this model is that, contrarily to tabulation models, does not have a limiter for the maximum Z coordinate in the chemical domain that can react. It means that acetylene is generated also where it should not and so it is distributed widely also in the CFD domain, in richer mixture regions (Fig. 5.11 and 5.12). This can be seen in Tab. 5.2, where all the peaks (especially at low temperature and oxygen concentrations) in RIF model are overestimated and close one to each other (Fig. 5.13). So soot results are expected to be not so accurate, but since the implementation of RIF model with the limiter was out of the scope of this work, the attention was concentrated only on the analysis of the impact of this issue on the results.

Also with this model, the starting soot constant values give bad results (Fig. 6.1), with close f_v peaks and wrong scaling among themselves. After some attempts, it is verified that the effects of changing every single constant are practically the same observed for TWM and TRIF model. However, the peaks distancing effect obtained by increasing *TaAlpha* and *TaOx* here is not observed because the great amount of acetylene at low temperature and oxygen cases overcomes the positive effect. Neither a further increase of the exponential terms give the desired result because nucleation and oxidation by O_2 cannot reduce anymore.

6.3.2 Soot volume fractions

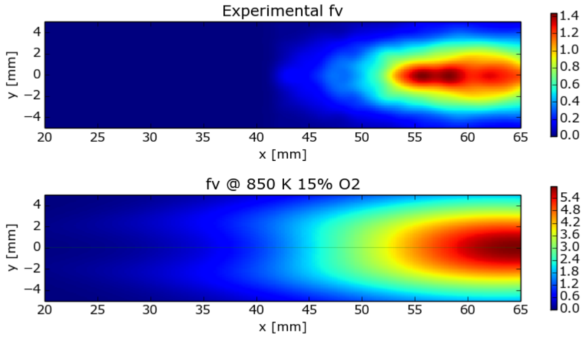

Figure 6.31: RIF: soot volume fraction at 850 K and 15% O_2

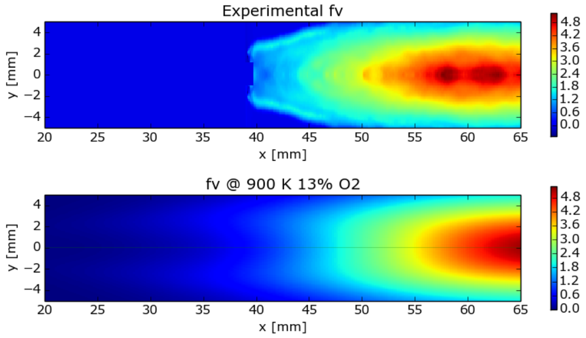

Figure 6.32: RIF: soot volume fraction at 900 K and 13% O_2

As said before, apart for lift-off, RIF model catches quite well flow fields and chemical species distribution. This determines soot cloud shapes and positions that are really good, except for 850 K 15% O_2 (Fig. 6.31). Wide radial extension is caused by the set of constants (Tab. 6.3.1), just as seen for other models, i.e. good radial extension for 1000 K 15% O_2 case (Fig. 6.35) is paid with a huge one at 900 K 13% O_2 (Fig. 6.32) and 900 K 15% O_2 (Fig. 6.33).

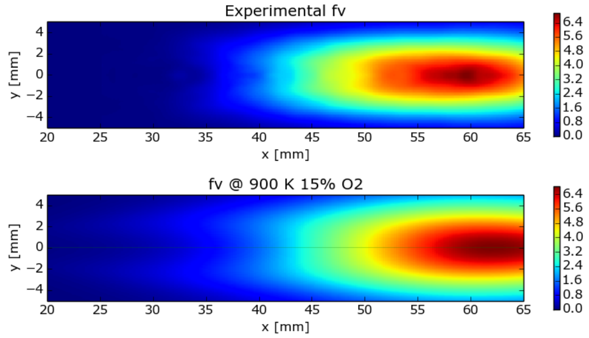

Figure 6.33: RIF: soot volume fraction at 900 K and 15% O_2

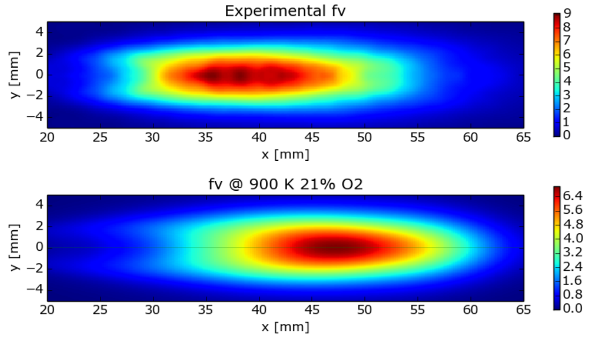

Figure 6.34: RIF: soot volume fraction at 900 K and 21% O_2

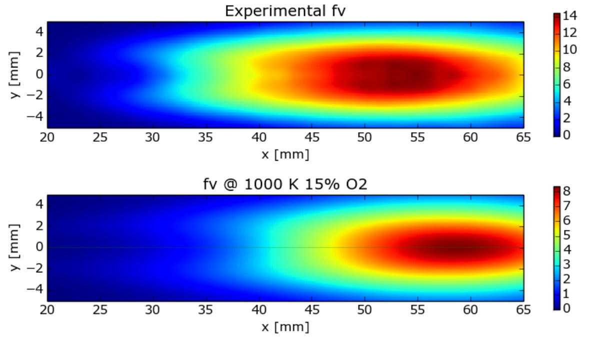

Figure 6.35: RIF: soot volume fraction at 1000 K and 15% O_2

Anyhow RIF is the only combustion model in which peak value of 900 K 21% O_2 (Fig. 6.34) stays under the 1000 K one: this is the effect of an acetylene concentration (Tab. 5.2 and Appendix A.3) that is not so bigger than the others (as it happens in TWM and TRIF).

	f_v peaks [ppm]
850 K 15% O_2	5.98904
900 K 13% O_2	5.29215
900 K 15% O_2	6.85306
900 K 21% O_2	7.00765
1000 K 15% O_2	8.3992

	$\frac{f_{v_i}}{f_{v_{1000_{15}}}}$
850 K 15% O_2	0.713
900 K 13% O_2	0.6301
900 K 15% O_2	0.8159
900 K 21% O_2	0.8343
1000 K 15% O_2	1

Table 6.10: RIF f_v peak values and normalized peaks (with respect to 1000 K 15% O_2)

Rates of creation and destruction have shapes very close to TRIF ones, except for the fact that nucleation and surface growth rates are shifted more upstream because acetylene distribution is upstream too. For this reason, they are reported in Appendix B.

6.3.3 Integral soot masses

Mass profiles suffers the problems underlined above. For low values of oxygen (Fig. 6.36) and temperature (Fig. 6.37) mass is overestimated. For what concerns the soot extinction phenomena, post-injection oxidation is favoured by high temperature and high oxygen concentration.

Another important observation is that mass profiles do not reach a steady value during the diffusive phase of combustion. Looking at the temporal evolution of the soot cloud in ParaFOAM (the post-processing viewer of OpenFOAM), it is clear that it does not stabilize as instead it happens in the other two models. The reason is probably again related to excessive formation of acetylene.

Onset values (Tab. 6.11) are the best one achieved among the three models and the growing phase of the first peak is caught very well.

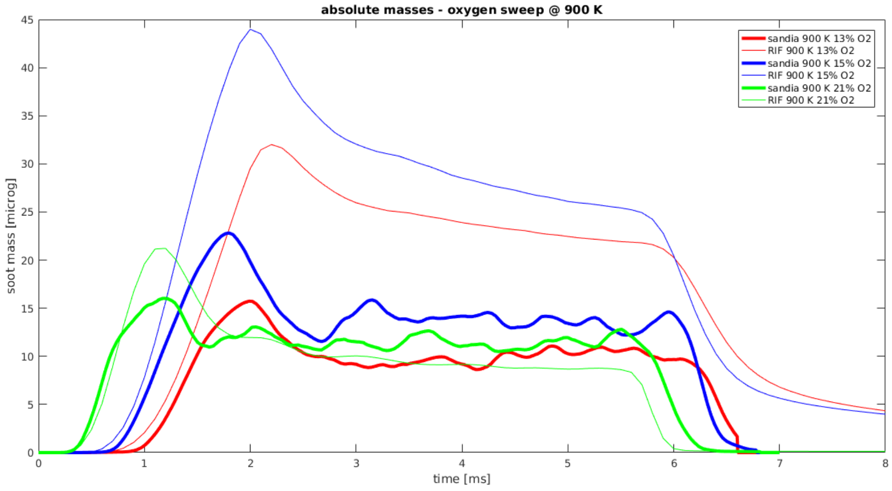

Figure 6.36: RIF: masses, oxygen sweep

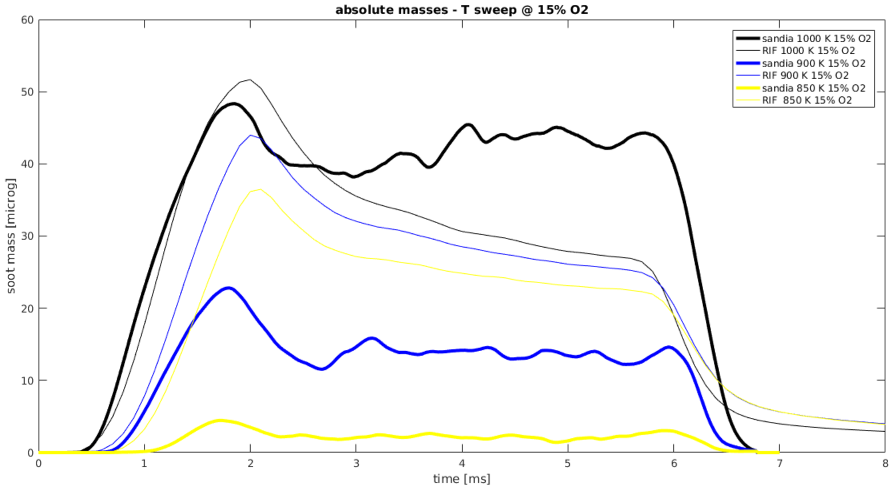

Figure 6.37: RIF: masses, temperature sweep

	850 K 15% O_2	900 K 13% O_2	900 K 15% O_2	900 K 21% O_2	1000 K 15% O_2
Sandia	1.05	1.01	0.785	0.385	0.575
RIF	0.9886	0.9459	0.7287	0.4190	0.6038

Table 6.11: RIF: onset of soot [ms]

Conclusions

CFD analysis of non-premixed combustion is the main topic of this thesis. Numerical calculations are performed using the open-source CFD software OpenFOAM, where combustion and soot models are implemented by the ICEGroup of Politecnico di Milano. The principal scope is to investigate the phenomena that govern soot formation and destruction. Another important point is to understand if simplified combustion and soot models can be adopted in order to obtain reliable numerical results, in particular for the prediction of soot, reducing the computational cost with alternative detailed approaches. The validation of the obtained results is done comparing them with the data provided by the ECN of Sandia National Laboratories. Five flame setups are used, with different oxygen concentration and temperature, in order to simulate various diesel engine conditions (i.e. EGR). The combustion chamber (i.e. vessel) is a constant volume bomb.

The only soot model that is employed is the well known Leung model, coupled with three different combustion models: RIF, TRIF and TWM. In particular, the last two adopts a tabulated chemistry approach, that allows to save a lot of computational time with respect to the RIF model, which solves directly chemistry without tabulation, but much slowly.

First, a validation of the thermodynamic fields and relevant chemical species distribution inside the bomb is performed, then soot results are analyzed. Here the main conclusions are listed:

- all the combustion models are able to reproduce precisely the evolution in time of the pressure rise curve, that is an indicator of the progress of combustion in time. Some uncertainties related to the first heat release peak (premixed phase) are present. The phases of the combustion that are more relevant for a soot analysis are the diffusive (mixing-controlled) and the burnout (post-injection) ones. RIF and TRIF models are a bit more precise than the TWM, that in some conditions tends to overestimate steady state value of diffusive phase and has a faster burnout.

- RIF model catches very well the ignition delays for all the cases, while TWM and TRIF have some issues, in particular for what concerns low initial temperature and oxygen concentration setups. This seems to confirm further which combustion model is the most accurate.

- in order to save computational time, in RIF and TRIF models, only one flamelet is employed, expecting less accurate results. However, computational time is still quite large for RIF (twice the TWM), while TRIF lasts more or less the 20 % more than TWM. Of course, as well known from previous studies, in both RIF based approaches with one flamelet, the flame is attached to the injector, leading to a wrong lift-off evaluation. TWM instead, since it has no shifting to the flamelet domain, is able to reproduce lift-off. For these reasons, no analysis related to the lift-off values was done. However, it must be said that for TWM model it is caugth perfectly.
- temperature profile in TWM model is thinner in radial direction (due to absence of turbulence-chemistry interaction), but with higher values in all the near-stoichiometric region. Temperature distribution plays a key-role in soot formation and destruction.
- acetylene (that is the only soot precursor that is employed in this work) spatial distributions strongly influences the positions of soot clouds. In RIF based approaches the fact that the temperature profile is attached to the injector makes acetylene attached too. In TWM approach of course this does not happen. However, again, the absensce of turbulence-chemistry interaction in the latter makes acetylene concentration thinner in radial direction. RIF and TRIF have instead wider precursor distribution. Oxidizing species region, in particular hydroxyl distribution, are much wider in RIF, TRIF with respect to TWM. In summary, turbulence-chemistry interaction seems to improve the results. For instance, hydroxyl distribution must be wide, as it is in reality, as confirmed by chemiluminescence data provided by Sandia.
- in RIF model, acetylene has not a limiter on the maximum Z where the reaction can take place, thus an overestimation of its concentration in rich mixture regions, in particular at low temperature and oxygen concentration, is observed, causing a completely wrong estimation of soot. Correction of this mistake is not done since it is not a scope of this thesis to implement again RIF model. Tabulated methods does not suffer this.
- numerical soot results obtained with the initial set of constants proposed by Leung are very different with respect to the Sandia data, so a calibration procedure is done, in order to understand how the soot generation/destruction processes vary if the parameters of the Arrenhius-like equations are modified. A black-box approach (i.e. authomatic optimization) would not allow to understand the sensitivity of the model. In the end, after a lot of attempts, all

the models showed similar reactions to the same parameter changes. The final optimal sets of constant has shown that oxidation processes are not well represented in the starting setups, since O_2 oxidation is too strong. Better results are obtained with strong hydroxyl oxidation. This verifies what said in Section 1.2.5. Also activation temperatures was re-defined in order to match better the experimental soot cloud shapes, inhibiting soot mass formation at low temperature and oxygen concentration (that was overestimated for sure).

- soot results at 850 K 15% O_2 are quite bad, probably for a wrong acetylene distribution, in particular for RIF. However further investigations are necessary. In other configurations, despite non perfect f_v peaks, soot clouds shapes are well reproduced in all the models. For what concerns the positions, TRIF has a more downstream acetylene distribution, causing a shifted soot cloud position.

- apart from RIF model, that as said before is not able to catch soot mass profiles, the other models are able to well reproduce the time advancing of soot mass. In particular, oxygen sweep cases at 900 K are very good also by a quantitative point of view for both TWM and TRIF. Soot onset is almost always very good, with the soot mass profiles that grow quickly. During post-injection phase, OH amount is very low, so the oxidizing effect, that as said previously, is mainly caused by it, becomes almost null. That seems to be the reason why the cases at low initial temperature and oxygen concentration are not capable of catching well the extinction of soot mass profile after the end injection. In this final phase, O_2 oxidation should be more evident, but it was already said that this is a compromise that is done in order to get good steady state soot cloud shapes, position and mass. The only exception is the 900 K 21% O_2 case, that has a very high oxidation rate due to OH, so it is able to fully oxidize the remaining soot mass within few instants after the the end of injection, while the other cases, after an initial fast oxidation phase due to abundance of hydroxyl, suffers the impossibility of oxidizing with O_2 only.

- the first peaks of the soot mass profiles are caught only by the TRIF model, even it seems that also RIF without the problem described before concerning soot estimation, would be able to efficiently reproduce it. TWM instead has a slower transition to the steady-state phase and it is not able to catch it. Generally, each model seems to be more suitable to simulate well cases with oxygen sweep, suffering instead ambient temperature variation. In order to better understand this phenomenon and why it happens, it would be necessary to have a larger set of experimental data. In particular, temperature, oxidizer and precursor spatial distributions would be very useful to understand which combustion model is able to reproduce better these aspects, since each of them shows big differences one from the other.

The final conclusion is that tabulation can be adopted in this kind of simulations, accepting only some compromises. For eventual future developments in this research fields, suggestions from the authors of this thesis are:

- trying to use a different soot precursor, in particular it would be interesting to investigate the role of benzene C_6H_6 in soot formation process
- using multiple flamelets in TRIF model, since in our opinion it could give very accurate results, thanks to the correct lift-off estimation, much faster than the simple multiple RIF (mRIF) combustion model
- comparing the results of this work with other chemical mechanism (for instance *Pei*)
- using a black-box optimization tool, verifying if the results agree with the considerations done in this work
- better understanding the role of the oxidizing agents during different phases of injection

Bibliography

[1] http://creckmodeling.chem.polimi.it/.

[2] https://ecn.sandia.gov/diesel-spray-combustion/experimental-diagnostics/lift-off-length/.

[3] https://ecn.sandia.gov/diesel-spray-combustion/experimental-diagnostics/light-based-ignition-delay/.

[4] https://ecn.sandia.gov/diesel-spray-combustion/experimental-diagnostics/soot/.

[5] https://www.cancer.gov/about-cancer/causes-prevention/risk/substances/soot.

[6] https://www.dieselnet.com/standards/cycles/wltp.php.

[7] http://www.cmt.upv.es/ECN03.aspx.

[8] http://www.engines.polimi.it/.

[9] Peters N. Barths H., Hasse C. Computational fluid dynamics modelling of non-premixed combustion direct injection Diesel Engines.

[10] Pitsch H. Bisetti F., Blanquart G. Direct numerical simulation of soot formation in turbulent non-premixed flames. *Center ofr Turbulence Research Annual Research Briefs*, 2008.

[11] Haynes B.S. and Wagner H.G. Soot formation. *Progress in Energy and Combustion Science 7*, pages 229–273, 1981.

[12] Baumgarten C. *Mixture formation in internal combustion engines.* Springer, 2006.

[13] Fenimore C.P. Oxidation of soot by hydroxyl radicals. *Journal of Physical Chemistry*, 71.

[14] Bryce D. et al. Investigating the effect of oxygenated and aromatic compounds in fuel by comparing laser soot measurements in laminar diffusion flames with

diesel-engine emissions. *Journal of the Institute of Energy 72*, pages 150–156, 1999.

[15] Frassoldati A. et al. Reduced kinetic mechanisms of diesel fuel surrogate for engine CFD simulations. *Combustion and Flame*, 2015.

[16] Hiroyasu H. et al. Development and Use of a Spray Combustion Modeling to Predict Diesel Engine Efficiency and Pollutant Emissions. *Bulletin of the Jsme Japan Society of Mechanical Engineers*, 26:569–575, 1983.

[17] Kronenburg A. et al. Modeling soot formation in turbulent methane-air jet diffusion flames.

[18] Lehtiniemi H. et al. Efficient 3-D CFD combustion modeling with transient flamelets models. *Rapp. tecn. SAE technical paper.*, 2008.

[19] Wang H. et al. Development of an n-heptane-n-butanol-PAH mechanism and its application for combustion and soot prediction. *Combustion and flame*, 160:504–519, 2013.

[20] Wen Z. et al. Modeling soot formation in turbulent kerosene/air jet diffusion flames.

[21] Bruneaux G. Combustion structure of free and wall-impinging diesel jets by simultaneous laser-induced fluorescence of formaldehyde, poly-aromatic hydrocarbons, and hydroxides. *International Journal of Engine Research*, 9(3):249–265, 2008.

[22] Ferrari G. *Motori a Combustione Interna.* Il Capitello, Torino, IT, 1996.

[23] Ferrari G. *Internal Combustion Engines.* Esculapio, Bologna, IT, 2011.

[24] Stiesch G. *Modeling engine spray and combustion processes.* Springer, 2003.

[25] Taylor G. The instability of liquid surfaces when accelerated in a direction perpendicular to their planes. *Proceedings of the Royal Society of London A: Mathematical, Physical and Engineering Sciences.*

[26] Weiner A.M. Harris S.J. *Combustion Science and Technology.* 1983.

[27] Aradi A. Higgins B., Siebers D. Diesel-Spray Ignition and Premixed-Burn Behavior. *SAE Technical Paper 2000-01-0940*, 200.

[28] Hernandez Vera Ignazio. *Soot modeling in flames and Large-Eddy Simulations of thermo-acoustic instabilities.* PhD thesis, Universite de Toulouse; France, 2011.

[29] Kennedy I.M. Models of soot formation and oxidation. *Progress in Energy and Combustion Science*, 23:95–132, 1997.

[30] Lindstedt R.P. Leung K.M. and Jones W.P. A Simplified Reaction Mechanism for Soot Formation in Nonpremixed Flames. *Combustion and Flame*, 87:289–305, 1991.

[31] Gilyazefdinov L.P. Khim. *Tverd. Topl.*, 3:3–103, 1972.

[32] Ettorre D. Lucchini T., D'Errico G. Numerical investigation of the spray-mesh-turbulence interactions for high-pressure, evaporating sprays at engine conditions. *International Journal of Heat and Fluid Flow.*

[33] Jangi M. Bai X.-S. Lucchini T. D'Errico G., Contino F. Diesel combustion modeling with detailed chemistry and turbulence-chemistry interaction. *www.academia.edu.*

[34] Bolla M. Modeling soot formation in diesel engines using conditional moment closure., 2013.

[35] D'Elia M. Analisi e ottimizzaione di un approccio a flamelet instazionari per la previsione di fiamme turbolente non-premiscelate., 2015.

[36] Mastrapasqua M. Modellazione del processo di combustione in motori diesel mediante modelli di combustione basati su cinetica chimica tabulata., 2016.

[37] Frenklach Micheal. Reaction mechanism of soot formation in flames. *Physical Chemistry Chemical Physics*, 4:2028–2037, 2002.

[38] Young K.J. Moss J.B., Stewart C.D. Modeling soot formation and burnout in a high temperature laminar diffusion flame burning under oxygen-enriched conditions. *Combustion and Flame*, 101:491–500, 1995.

[39] Peters N. Laminar diffusion flamelet models in non-premixed turbulent combustion.

[40] Peters N.. *Turbulent combustion.* Cambridge.

[41] Peters N. Laminar flamelet concept in turbulent combustion. *Symposium (International) on Combustion*, 21:1231–1250, 1988.

[42] Strickland-Constable R.F. Nagle J. Proceedings of the Fifth Carbon Conference. In -, volume 1, pages 1–62, 1962.

[43] Sarofim A.F. Neoh K.G., Howard J.B. Particulate carbon formation during combustion. *Plenum*, 1981.

[44] Kirchen P. *Steady-State and Transient Diesel Soot Emissions: Developlment of a Mean Soot Model and Exhaust-Stream and In-Cylinder Measurements.* PhD thesis, ETH Zurich; Switzerland, 2008.

[45] Peters N. Pitsch H., Riesmeier E. Unsteadt flamelet modeling of soot formation in turbulent diffusion flames.

[46] Smyth K.C. Puri R., Santoro R.J. The oxidation of soot and carbon monoxide in hydrocarbon diffusion flames. *Combustion and Flames*, pages 125–144, 1997.

[47] Stagni A. Pelucchi M. Cuoci A.-Faravelli T. Ranzi E., Frassoldati A. Reduced kinetic schemes of complex reaction systems: fossil and biomass-derived transportation fuels. *Int. J. Chem. Kinet. 46*, pages 512–542, 2014.

[48] Reitz R.D. Modeling atomization processes in high-pressure vaporizing sprays. *Atomisation Spray Technology.*

[49] Carbonell Daniel Sanchez. *Numerical studies of diffusion flames. Special emphasis on flamelet concept and soot formation.* PhD thesis, Universitat Politecnica de Catalunya; Spain, 2008.

[50] Pope S.B. Computationally efficient implementation of combustion chemistry usinf in situ adaptive tabulation. *Combustion Theory Modelling.*

[51] Pratsinis S.E. Simultaneous Nucleation, Condensation and Coagulation in Aerosol Reactors. *Journal of Colloid and Interface Science*, 124:416–427, 1988.

[52] Dalen K. Pickett L.M. Skeen S.A., Manin J. Extinction-based Imaging of Soot Process over a Range of Diesel Operating Conditions. In *8th U.S. National Combustion Meeting Organized by the Western States Section of the Combustion Institute and hosted by the University of Utah*, 2013.

[53] Pfefferle L.D. Smoke M.D., McEnally C.S. Computational and experimental study of soot formation in a coflow, laminar diffusion flame. *Combustion and Flame*, 117:117–139, 1999.

[54] Frassoldati A. Faravelli T. Ranzi E. Stagni A., Cuoci A. Lumping and reduction of detailed kinetic schemes: an effective coupling. *Ind. Eng. Chem. Res.*, 2014.

[55] Poinsot T. *Theoretical and numerical combustion.* Edwards, 2012.

[56] Knorre V.G. Tesner P.A., Snegirova T.D. Kinetics of dispersed carbon formation. *Combustion and Flame*, 17:253–260, 1971.

[57] Glassman I. Vandsburger U., Kennedy I. *Combustion Science and Technology.*, volume 53. 1984.

[58] Malalasekera W. Versteeg H.K. *An introduction to computational fluid dynamics.* Pearson Education, 2007.

Appendix A

First appendix

A.1 Pressure

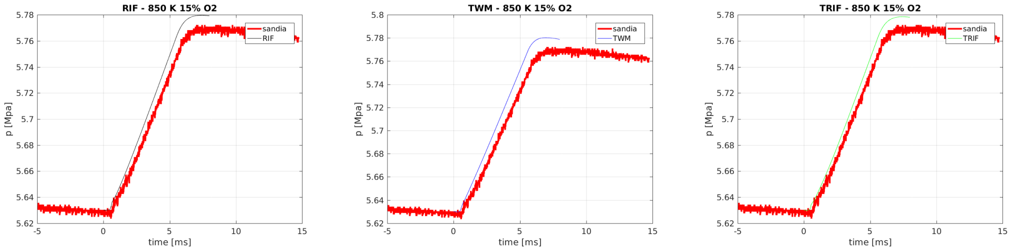

(a) RIF (b) TWM (c) TRIF

Figure A.1: Pressure at 850 K 15% O_2.

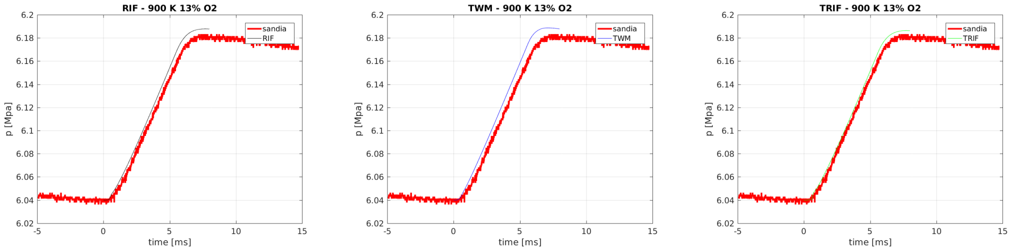

(a) RIF (b) TWM (c) TRIF

Figure A.2: Pressure at 900 K 13% O_2.

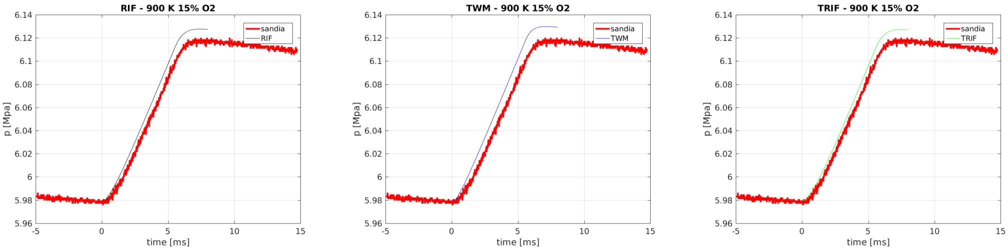

(a) RIF (b) TWM (c) TRIF

Figure A.3: Pressure at 900 K 15% O_2.

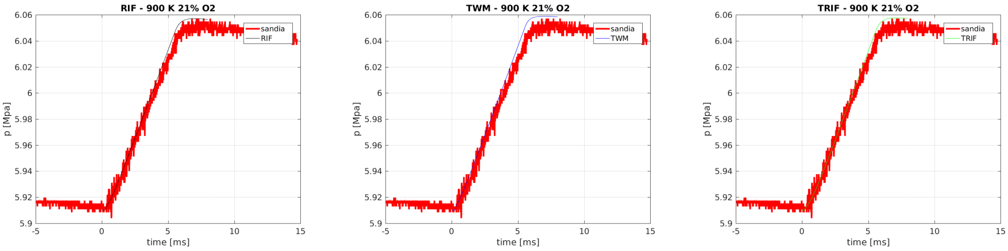

(a) RIF (b) TWM (c) TRIF

Figure A.4: Pressure at 900 K 21% O_2.

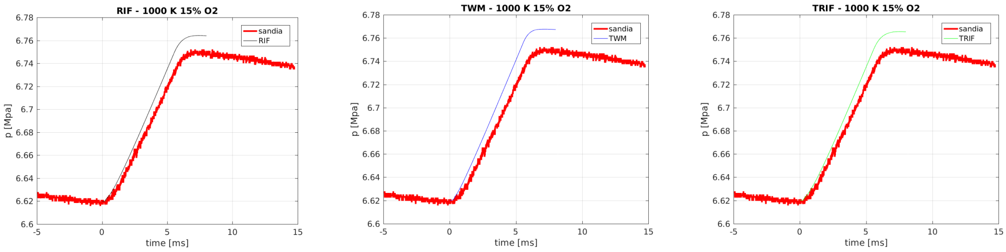

(a) RIF (b) TWM (c) TRIF

Figure A.5: Pressure at 1000 K 15% O_2.

A.2 Rate of heat release

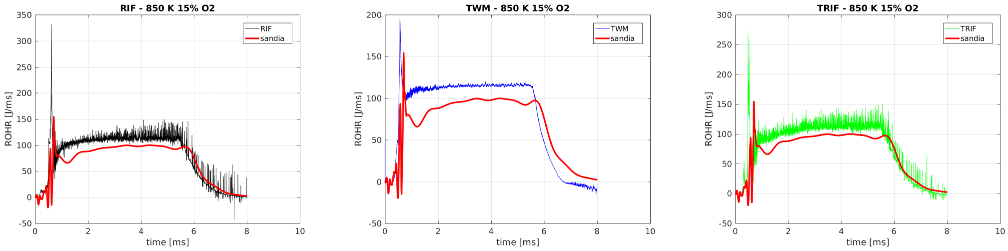

(a) RIF (b) TWM (c) TRIF

Figure A.6: Rate of heat release at 850 K 15% O_2.

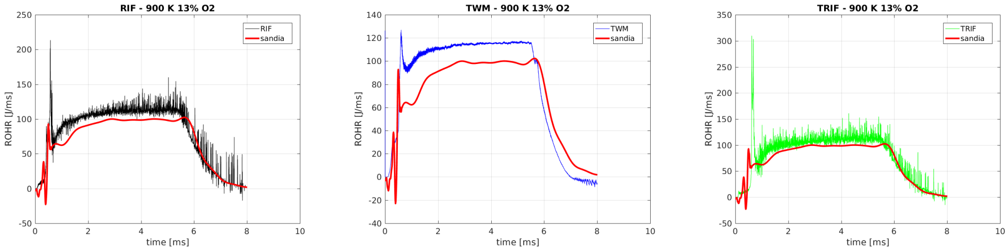

(a) RIF (b) TWM (c) TRIF

Figure A.7: Rate of heat release at 900 K 13% O_2.

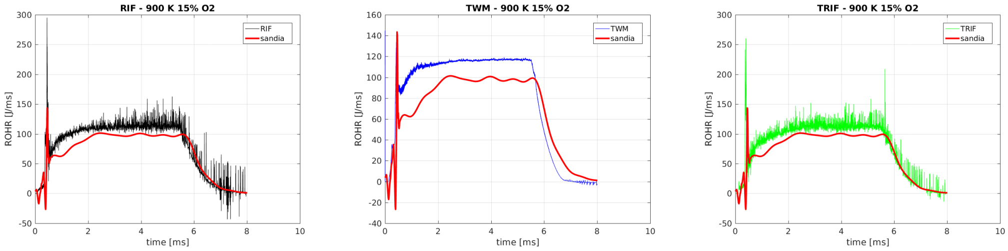

(a) RIF (b) TWM (c) TRIF

Figure A.8: Rate of heat release at 900 K 15% O_2.

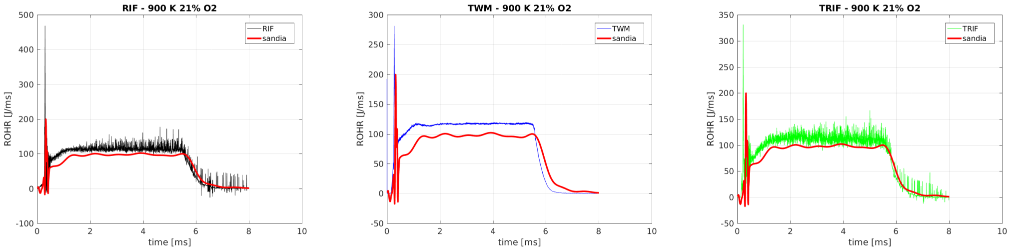

(a) RIF (b) TWM (c) TRIF

Figure A.9: Rate of heat release at 900 K 21% O_2.

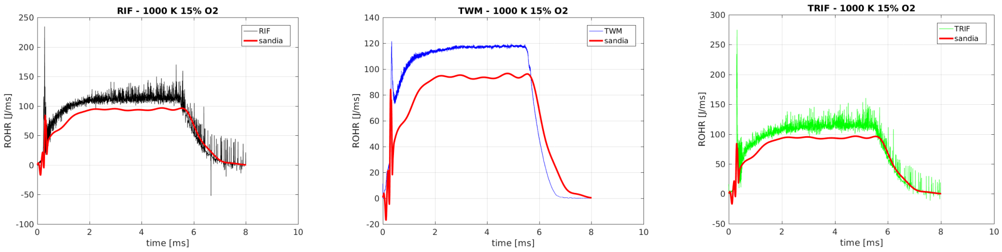

(a) RIF (b) TWM (c) TRIF

Figure A.10: Rate of heat release at 1000 K 15% O_2.

A.3 Temperature, acetylene, oxygen and hydroxyl spatial distributions

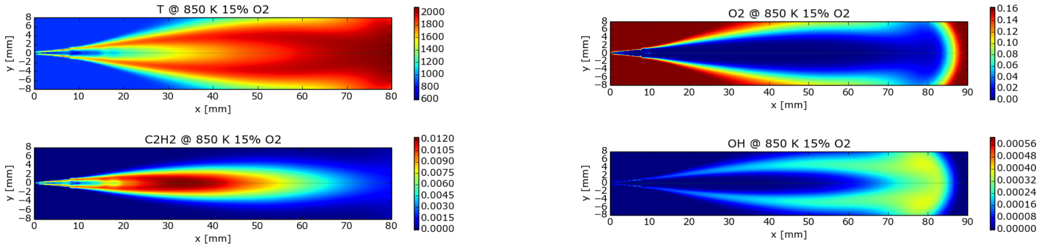

(a) RIF

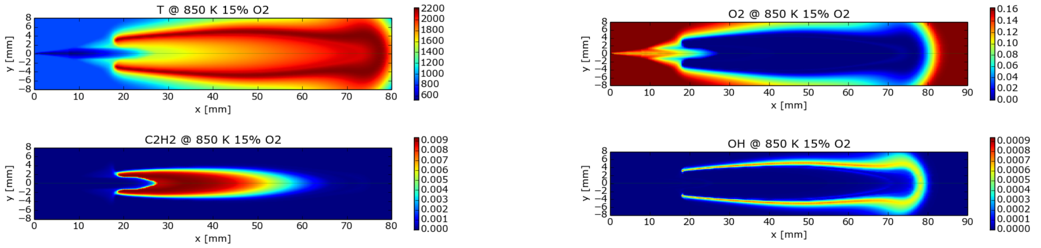

(b) TWM

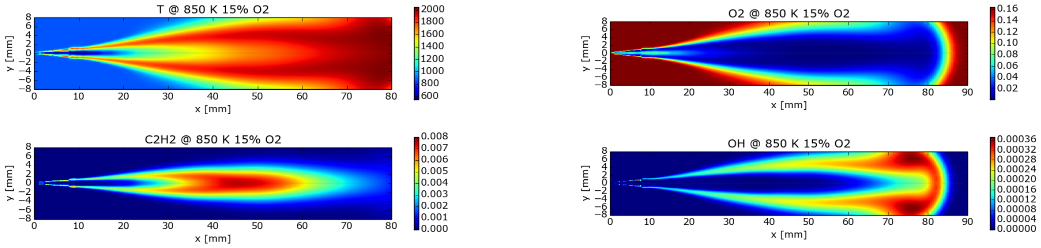

(c) TRIF

Figure A.11: T, C_2H_2, O_2 and OH spatial distributions at 850 K 15% O_2.

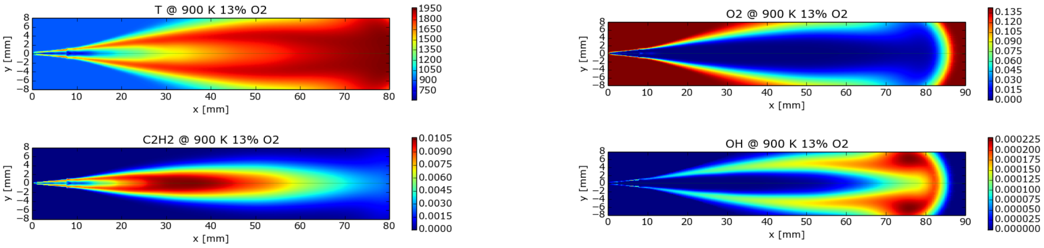

(a) RIF

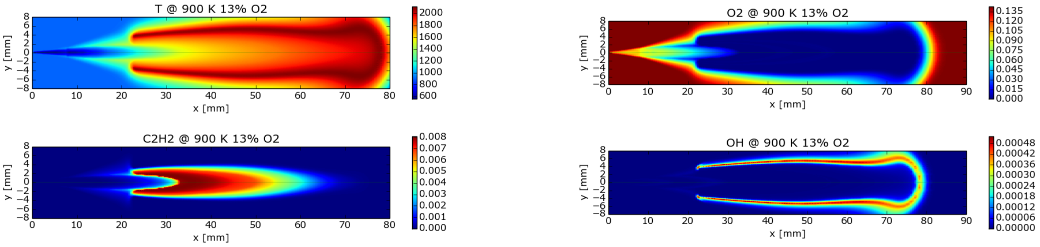

(b) TWM

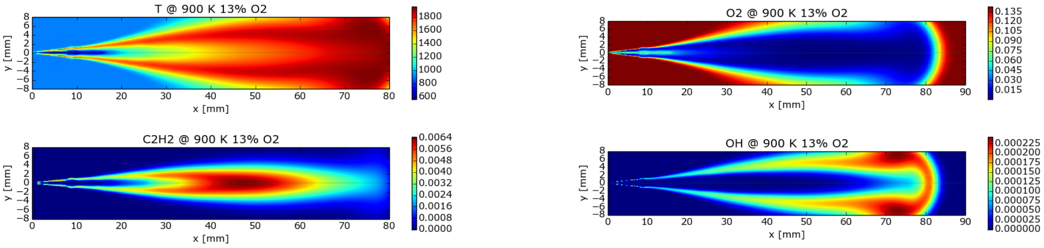

(c) TRIF

Figure A.12: T, C_2H_2, O_2 and OH spatial distributions at 900 K 13% O_2.

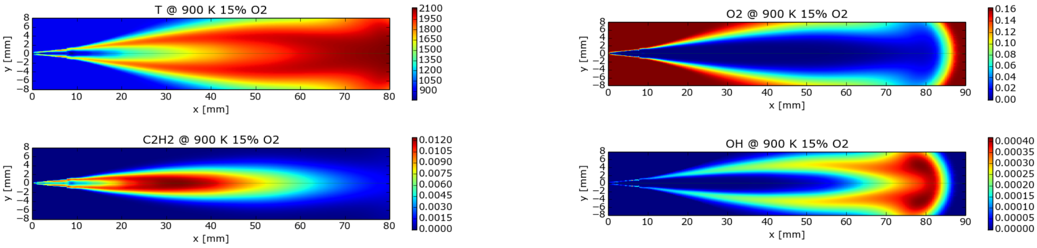

(a) RIF

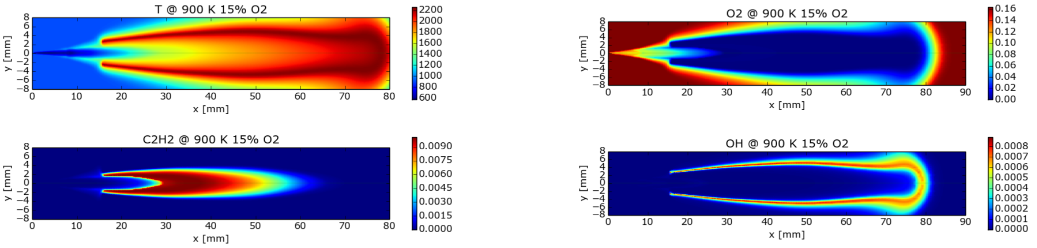

(b) TWM

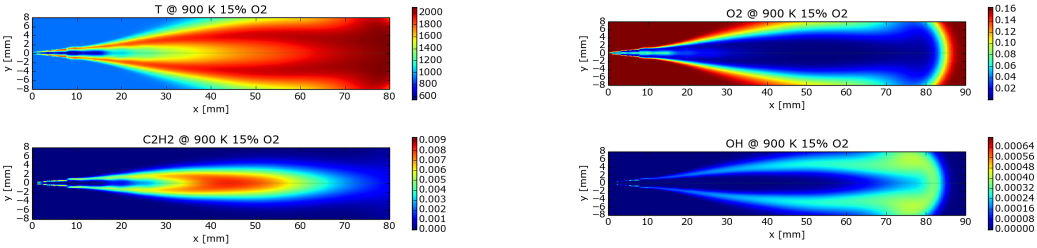

(c) TRIF

Figure A.13: T, C_2H_2, O_2 and OH spatial distributions at 900 K 15% O_2.

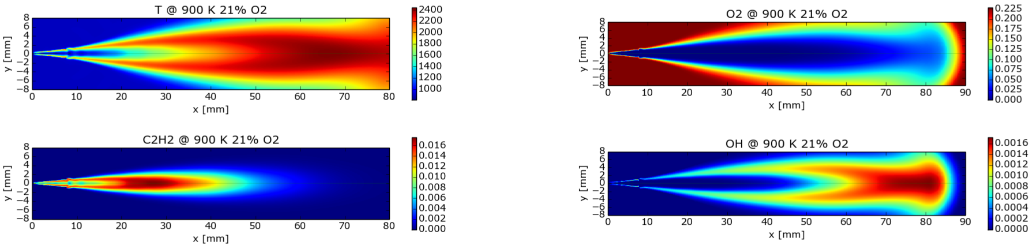

(a) RIF

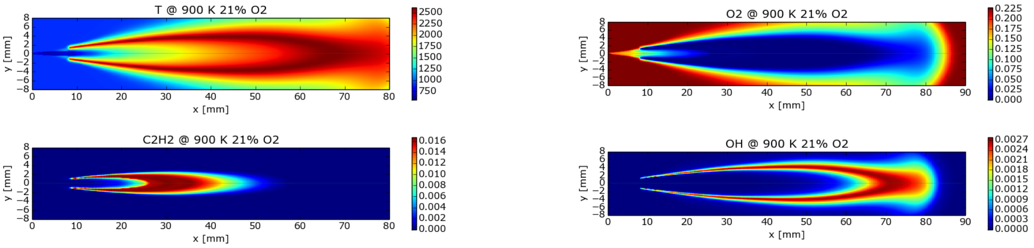

(b) TWM

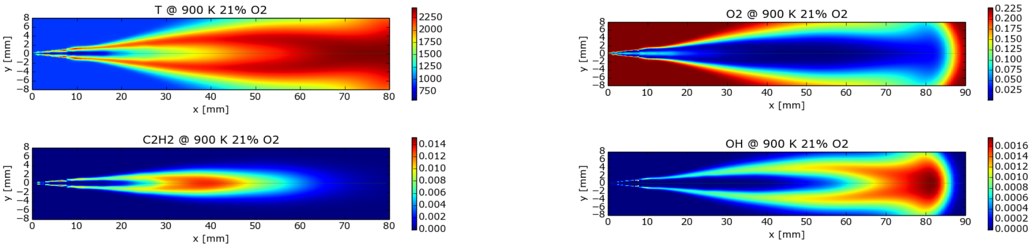

(c) TRIF

Figure A.14: T, C_2H_2, O_2 and OH spatial distributions at 900 K 21% O_2.

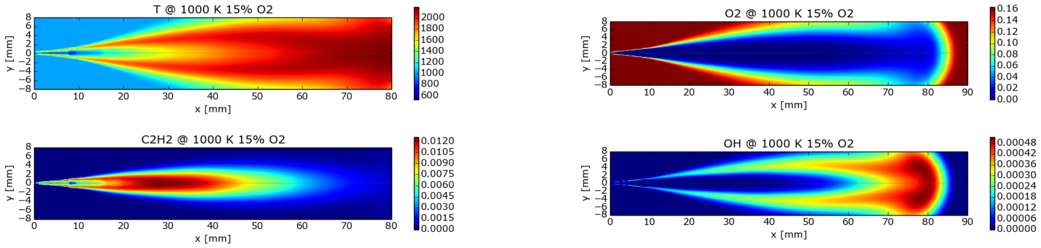

(a) RIF

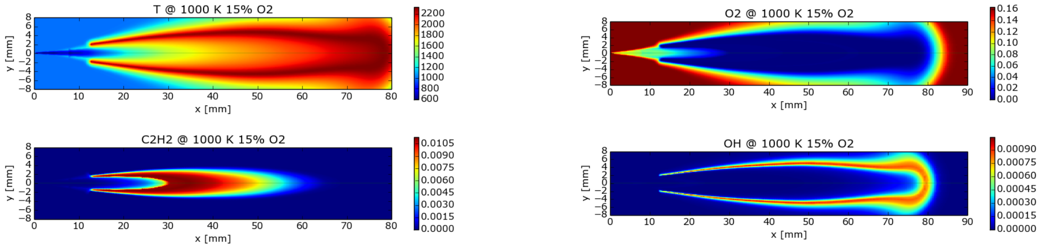

(b) TWM

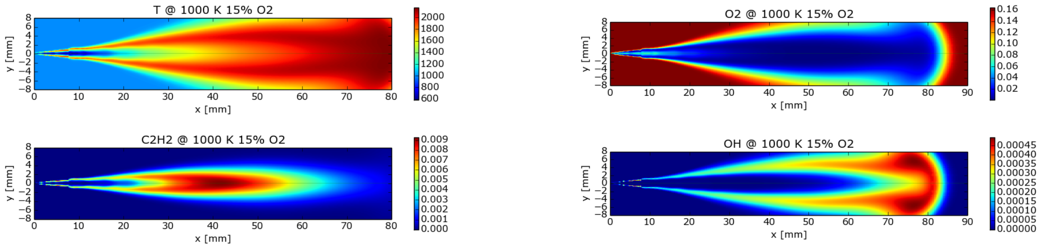

(c) TRIF

Figure A.15: T, C_2H_2, O_2 and OH spatial distributions at 1000 K 15% O_2.

Appendix B

Second appendix

B.1 Rates of creation and destruction for RIF combustion model

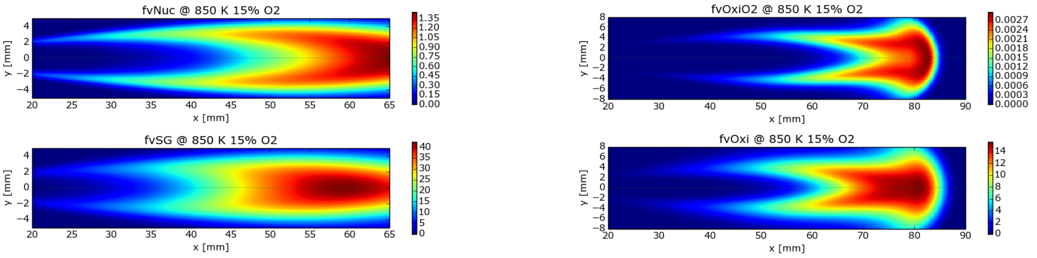

Figure B.1: RIF: rates of nucleation, surface growth and oxidation at 850 K and 15% O_2.

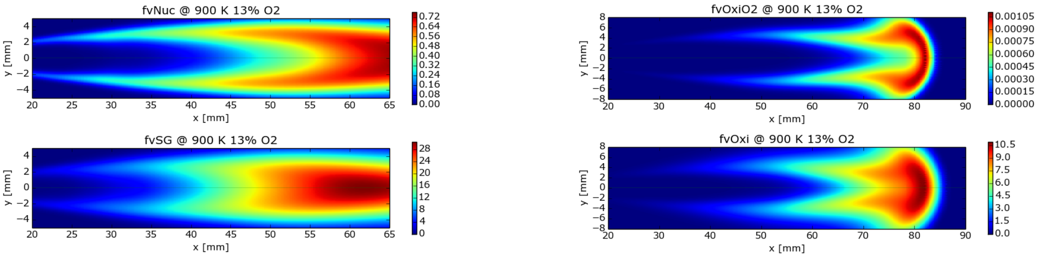

Figure B.2: RIF: rates of nucleation, surface growth and oxidation at 900 K and 13% O_2.

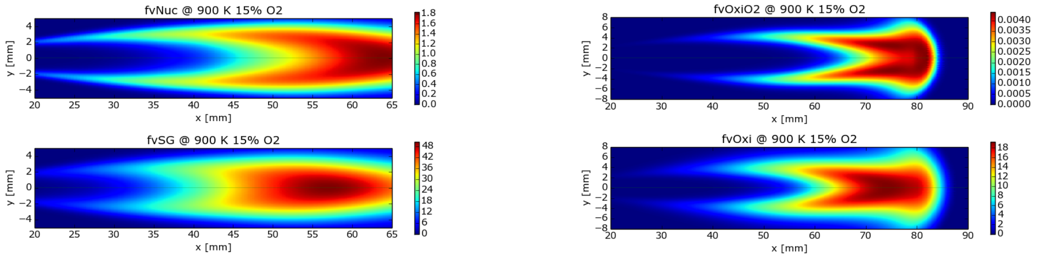

Figure B.3: RIF: rates of nucleation, surface growth and oxidation at 900 K and 15% O_2.

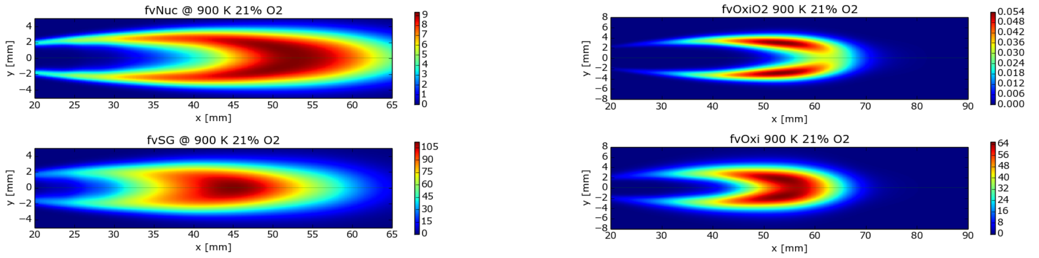

Figure B.4: RIF: rates of nucleation, surface growth and oxidation at 900 K and 21% O_2.

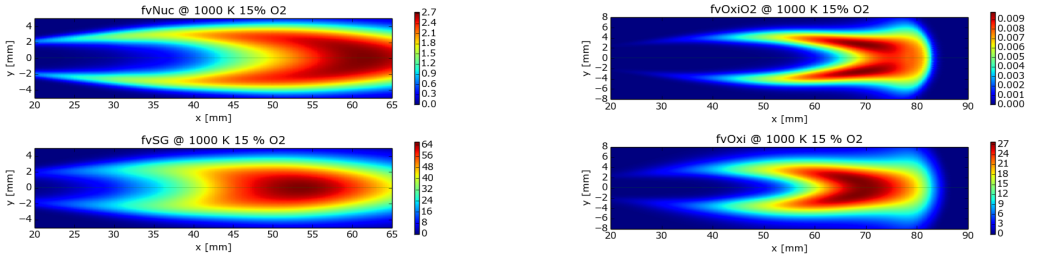

Figure B.5: RIF: rates of nucleation, surface growth and oxidation at 1000 K and 15% O_2.